Identification of Fold Hinge Migration in Natural Deformation: A New Technique Using Grain Shape Fabric Analysis

Kelly Kathleen Rose

Thesis submitted to the Faculty of the
Virginia Polytechnic Institute and State University
in partial fulfillment of the requirements for the degree of

Masters of Science
in
Geological Sciences

_____
Richard D. Law, Chair

_____
John A. Hole

_____
Jim A. Spotila

June, 10, 1999
Blacksburg, Virginia

Keywords: Hinge Plane Migration, Grain Shape Fabric Analysis,
Crystal Preferred Orientations, Rf/ϕ Analysis, Grandfather Mountain Window

Identification of Fold Hinge Migration in Natural Deformation: A New Technique Using Grain Shape Fabric Analysis

Kelly Kathleen Rose

(ABSTRACT)

Partitioning of finite strains in different domains within the limb and hinge regions of a fold can be used to understand the deformation processes operative during fold formation. Samples taken from the limb and hinge regions of a gently plunging, asymmetric, tight, mesoscale fold in the Erwin formation of the Blue Ridge in North Carolina were analyzed to determine the deformation mechanisms and strains associated with the folding event. Rf/ϕ grain shape fabric analysis was conducted for each sample and used to calculate the orientation and magnitude of the final grain shape fabric ellipsoids. Flexural folding and passive-shear folding models predict that the highest finite strains (ε_s-values) will be recorded in the hinge of a fold. The highest grain shape magnitudes recorded in the North Carolina fold, however, lie along the overturned fold limb.

The final geometry of many folds indicates that hinge plane migration processes are active during compressive deformation events. Numeric, conceptual, and analogue based studies have demonstrated the migration of fold hinges during deformation. However, documentation of these processes in field based studies is rare and limited to techniques that are frequently site specific. Methods proven successful in natural studies include the analysis of superposed folding; the migration of earlier hinge-related features such as fractures, cleavage planes, and boudinaged bedding planes; and the kinematic analysis of syntectonic pressure shadows. The magnitude and orientation of the grain shape ellipsoids calculated for the North Carolina fold indicate that rocks in the overturned limb were once located in the hinge of the fold. Subsequent noncoaxial deformation processes operative during folding resulted in the migration of the hinge to its present orientation and position. This relationship indicates that it is possible to use strain/shape fabric analysis as a test for hinge migration in folds, and that this technique may be more generally applicable in natural settings than previously proposed tests.

Please Note – An accurate and clear presentation of figures and tables is not possible when viewed on most computer monitors. However, when <u>printed</u> figures and tables should no longer exhibit any distortions.

Acknowledgements

Field and laboratory work was funded by grants to Kelly Rose, from the American Association of Petroleum Geologists (1997 Grant-in-Aid), the Byron Cooper Fellowship (1997 Department of Geological Sciences, Virginia Tech), Sigma Xi (1997 Grant-in-Aid of Research), and the Southeastern Section of the Geological Society of America (1997 Research Grant).

I owe extensive thanks to a variety of people for their help and support over the past few years. In particular, the support and encouragement of my mom, brother (Mike), JLJ Jr., Mocha, Chessie, Bear, and family at large, who have provided me with the strength and creativity to accomplish my goals and survive some interesting trials. The graduate students in our department; Jim, Jeane, Amy, Adam, Andy, B.J., Bill, Erin, Gwen, Jason (and PJK), Jay, Joel, John, Lee, Nancy, Rhonda, Rod, and, Shelley, who helped me maintain my sanity, sense of humor, and provided ample excuses to escape the first floor labyrinth where the majority of my time was spent. Also, thanks to the undergraudate majors who amazed me with their endless curiosity and inquisitive presence. To Sandra and Tom in Tyler, who will never know how positively and deeply their mentorship and friendship impacted my life this last year. And, to my friends outside of the Geology Department, and at other locations around the country for their emailed support and link to the world at large. Special thanks and consideration to the faculty, staff, engineers, and technicians of the department for all of their, help, support, and friendship. Finally, thanks to Rick for weathering the last three years and allowing me to experiment, investigate and make mistakes, while providing positive encouragement and support.

Table of Contents

	Page #
TITLE PAGE ……	i
ABSTRACT ..……	ii
ACKNOWLEDGMENTS ……..…	iii
TABLE OF CONTENTS ……..…	iv
LIST OF FIGURES ……..…….……	vi
LIST OF TABLES ……..…….....	vii
1. INTRODUCTION ……...……...……	1
2. HINGE MIGRATION DURING FOLDING ..……	1
2.1. *Hinge Migration in Natural Deformation* ……..	1
2.2. *Hinge Migration in Numerical, Analogue, and Conceptual Models* …….	4
2.3. *Definition and Types of Hinge Plane Migration* ……	5
2.3.1. Kinematic Framework and Reference Frame …….	5
2.3.2. Hinge Plane Migration Kinematic Processes …….	6
2.3.3. Material versus Nonmaterial Hinge Plane Migration	10
3. GEOLOGIC SETTING ..…….	11
3.1. *Blue Ridge Province, Northwest North Carolina*	11
3.2. *Characterization of the Clinchfield Railroad Fold*	13
4. METHODS AND RESULTS ……..…....	15
4.1. *Sample Acquisition and Preparation* …….	15
4.2. *Petrographic Analyses* ……..	15
4.2.1. Results and Data Presentation ……	15
4.3. *Crystal Preferred Orientation Analysis* …….	17
4.3.1. Results and Data Presentation ……	18
4.4 *Grain Shape Fabric Analysis* …….	18
4.4.1. Results and Data Presentation ……	25
5. DISCUSSION …….....	27
5.1. *Temperature and Depth of Deformation* ……	27
5.2. *Development of the Clinchfield Railroad Fold* ……..	28
5.2.1. Active Thrust Related Folding and the Clinchfield Railroad Fold …….	30
5.2.2. Magnitudes and Symmetry of Grain Shape Fabric Ellipsoids ……..	31
5.2.3. Obliquity of Fold Axes – Rotation of Folds During Progressive Deformation ……..	34
5.3. *Hinge Migration and the Clinchfield Railroad Fold* ……..	38
5.3.1. Strike-Rotation Hinge Plane Migration and the Obliquity of the Clinchfield Railroad Fold Axis …	38

Page #

5.3.2. Material Translation Hinge Plane Migration and the Clinchfield Railroad Fold …… 39

5.4. *Crystal Preferred Orientation Measurements, Record of Initial Layer-Parallel Shortening* …… 41

5.5. *Kinematic Model for the Development of the Clinchfield Railroad Fold* ……. 42

6. CONCLUSIONS …… 45

REFERENCES ……. 46

SOFTWARE ……. 50

APPENDIX I – Grain Shape Fabric Trends …… 51

APPENDIX II – 2D-3D Section Data ……..…. 52

APPENDIX III – Rf/ϕ Plots ……..….. 54

APPENDIX IV – Analytical Procedure ..……. 60

APPENDIX V – Natural Octahedral Unit Shear Equation …….…….. 61

APPENDIX VI – Validity of Lisle's Fabric Symmetry Variable (I) and Nadai, Lodes Number, and Lisle Calculations ….…… 62

VITA ……. 76

List of Figures

Please Note – An accurate and clear presentation of figures and tables is not possible when viewed on most computer monitors. However, when printed figures and tables should no longer exhibit any distortions.

		Page #
Figure 1.	Borradaile's (1979) model for folding of the Islay Anticline	2
Figure 2.	Down plunge projection cross section of the Clover Hollow Anticline-Syncline pair ……	3
Figure 3.	Progressive folding by hinge migration model developed by Beutner and Diegel (1985) …….	3
Figure 4.	Cross sectional view of the Jennings Creek fold, Central Virginia ……..	3
Figure 5.	Four end-member hinge plane migration kinematic processes	7
Figure 6.	Conceptual models of hinge plane migration kinematic processes ……	8 & 9
Figure 7.	Regional reference map and geologic map of the study area.	12
Figure 8.	Isograd map of the Grandfather Mountain Window region.	13
Figure 9.	Structural stereoplots and field photograph of Clinchfield Railroad Fold …….	14
Figure 10.	Sample bed and sample locations from the Clinchfield Railroad fold ……..	16
Figure 11.	Mineral composition point counts, each sample and representative photomicrograph …….	16
Figure 12.	Quartz c-axis fabric plots, sample 4 ……	19
Figure 13.	Quartz c-axis fabric plots, sample 1 ……	20
Figure 14.	Quartz c-axis fabric plots, sample 2 ……	21
Figure 15.	Quartz c-axis fabric plots, sample 3 ……	22
Figure 16.	Quartz c-axis fabric plots, sample 5 ……	23
Figure 17.	Nadai (natural) Strain plot and Flinn plot ……	26
Figure 18.	Photomicrographs of representative microstructures (a-f) .	29
Figure 19.	Schematic models of a Mode II fault-bend, fault-propagation and detachment folds ……..	32

Page #

Figure 20. Schematic models for folding involving flexural-slip and tangential longitudinal strain …….. 32

Figure 21. Wireframe representations of grain shape ellipsoids, calculated from 2-D sectional ……. 33

Figure 22. Fold models for generalized flexural folding and generalized passive shear folding …….. 35

Figure 23. Line drawing indicating the magnitude ($\bar{\varepsilon}_s$) & symmetry (k) of the grain shape fabric at each sample location …… 36

Figure 24. Coward and Potts (1983) model for arcuate thrusting and related fold development ……. 37

Figure 25. Relationship of the Clinchfield Railroad's fold axis and the X grain shape axis …….. 40

Figure 26. Model for the development of the CPO fabric at the study site …….. 43

Figure 27. Model illustrating the projected location of the Clinchfield Railroad fold within the Tablerock thrust sheet …….. 44

List of Tables

Table 1. Microstructures observed at each sample location …….. 17

Table 2. List of terms and variables ……. 24

Table 3. Calculated values of grain shape fabric axes, magnitudes and symmetries ……. 26

1. Introduction

The final geometry of folds found in compressional deformation belts indicates that hinge plane migration processes may be active during progressive folding. Both theoretical and analogue based studies have demonstrated that fold hinges may migrate during deformation, although documentation of these processes in field based studies is rare and limited to techniques that are frequently site specific. Partitioning of finite strains in different domains within the limb and hinge regions of a fold, however, can be used to understand and identify the deformation processes operative during fold formation, including those associated with hinge plane migration.

This study; i) provides a review of existing natural, numeric, conceptual, and analogue hinge plane migration studies, ii) develops a definition for hinge plane migration during folding, iii) provides a possible interpretation for obliquity of fold hinges and hinge planes to the regional trend in overthrusts terraines, and iv) proposes a new method for identifying hinge migration in natural folds using strain/grain shape factor and crystal preferred orientation (CPO) analyses. The use of grain shape fabric analysis as a tool for identifying hinge plane migration processes in buckled layers is demonstrated through the examination of a mesoscale fold in the Blue Ridge Province of western North Carolina.

2. Hinge Migration During Folding

Hinge migration is frequently used to explain the development and final geometry of folds. There are, however, few existing natural, numeric, conceptual, or analogue studies that provide methods for conclusively identifying folds whose hinges have migrated in natural settings. Theoretical and analogue studies typically involve, i) mathematical predictions or simulations, ii) analogue modeling of folding through the experimental deformation of various materials, or iii) schematic diagrams that illustrate situations when hinge migration may occur during folding. These published theoretical and analogue studies review the potential for hinge migration in the development of a large variety of folding styles; kink folds, chevron folds, box folds, domes, basins, etc. while previous natural studies have primarily succeeded in identifying hinge migration in asymmetric antiformal folds.

2.1. Hinge Migration in Natural Deformation

To date, there are five previously published studies that document evidence for hinge migration in naturally occurring folds. Each of these studies relies on a different set of mesoscale and/or microscale observations to identify the activity of hinge migration processes during folding, and suggest criteria for identifying hinge migration in natural deformation.

In 1979, Borradaile used strain histories and deformation mechanisms to identify hinge migration in the Islay Anticline of southwest Scotland. The final geometry of bedding and

cleavage in the Islay Anticline resembles those found in cleavage fans. In this study, however, Borradaile (1979) argued that axial planar cleavage formed early during fold formation (Fig. 1). In the upright limb of the Islay Anticline the axial planar bedding-cleavage relationship was maintained. During progressive deformation in and around the hinge of the fold, however, the cleavage planes dip less steeply than the late forming, XY finite strain ellipse and are not axial planar in nature. Based on this relationship, Borradaile suggested that hinge migration processes were activated after development of the axial planar cleavage and resulted in rotation of the cleavage planes in and around the hinge into their present day orientations (Fig. 1).

Gray (1981) and Simon and Gray (1982) extended the use of bedding-cleavage relationships in the identification of hinge migration through the examination of mesostructures and strain in the Clover Hollow Anticline of Giles County, Virginia. Pressure-solution, "modification models" for bedding-cleavage relationships originally developed by Groshong (1975), were used by Simon and Gray (1982) to argue for the development of axial-planar cleavage early during folding of the Clover Hollow Anticline. They maintained that the observed oblique fanning of cleavage across the anticline and location of the bedding perpendicular cleavage in the southeastern limb of the anticline is due to hinge migration during deformation either by rotational or translational processes (Fig. 2).

Beutner and Diegel (1985) used the kinematics of quartz pressure shadows on pyrite grains in folds of the Martinsburg Slate, New Jersey, to argue for hinge migration during folding. They observed that quartz pressure shadows from the long limbs of these folds were composed of straight fibers, however, pressure fibers from the hinge and short limbs of these folds displayed more complex straight-curved fiber patterns (Fig. 3). Based on variations in fiber geometries around the folds, Beutner and Diegel (1985) proposed a model for fold formation beginning with fold nucleation and active limb rotation, followed by hinge migration via rotation and translation of bedding and possibly the hinge planes, and ending with flattening (Fig. 3).

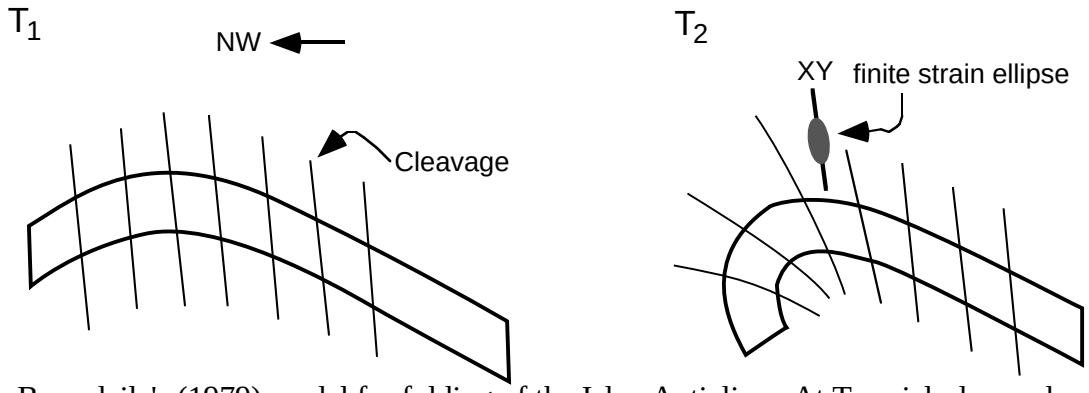

Fig. 1. Borradaile's (1979) model for folding of the Islay Anticline. At T_1 axial planar cleavage is formed, as deformation proceeds (T_2) the axial planar cleavage is rotated by hinge migration processes into an orientation that differs from the late forming XY finite strain ellipse.

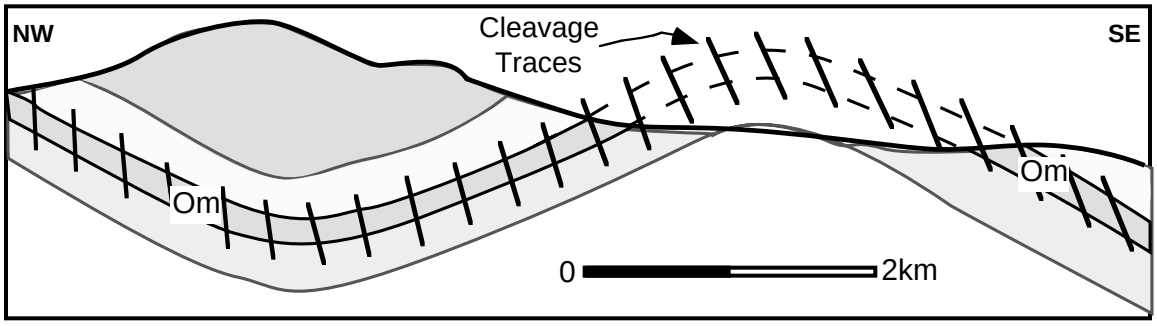

Fig. 2. Down plunge projection cross section through the Clover Hollow Anticline-Syncline pair. Cleavage-bedding relationships are illustrated in the Moccasin (O_m) Formation. Obliquity of cleavage-bedding at the crest of the Clover Hollow Anticline is attributed to activity of hinge migration processes during deformation (adapted from, Simon and Gray, 1982).

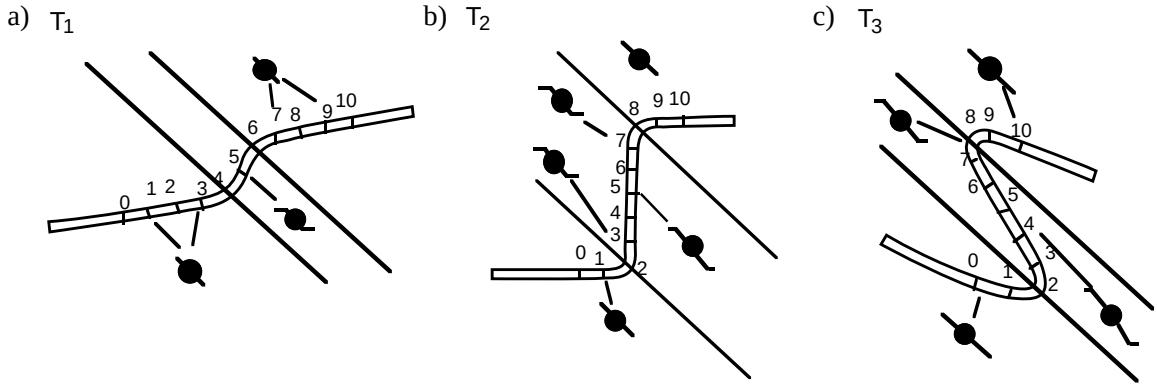

Fig. 3. Progressive folding by hinge migration model developed by Beutner and Diegel (1985). At T_1 folding is initiated, T_2 hinge migration processes are active during deformation, T_3 continued rotation and flattening of the fold.

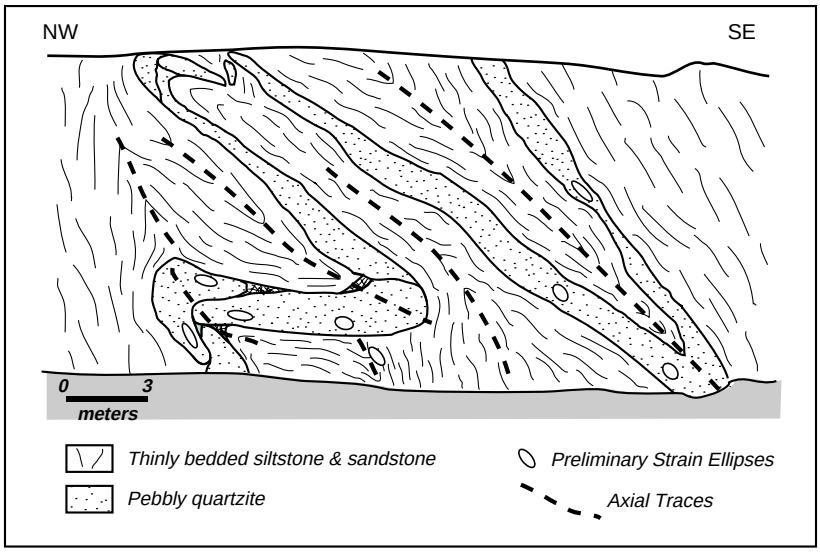

Fig. 4. Cross sectional view of the Jennings Creek fold, Blue Ridge Province, Central Virginia. Boudinaged segments of the pebbly quartzite bed are imbricated over one another in the hinges of the fold (Bailey and Brooks, 1996).

Finally, in a preliminary study of a mesoscale fold along Jenning's Creek in Central Virginia, Bailey and Brooks (1996) made their case for hinge migration during folding. The Jenning's Creek fold is composed of thinly interbedded siltstones and sandstones that surround a more competent, thickly bedded sandstone-conglomerate layer. Bailey and Brooks (1996) argued that asymmetric folding was initiated because of fault propagation in the less competent units. Strain and microstructural data indicate that the overturned fold limbs underwent boudinage early during the folding event (Fig. 4). With continued deformation the boudinaged limbs migrated into the hinges of the folds where they were imbricated into their present day positions and inhibited further translation of material into and through the hinges of the fold.

2.2. Hinge Migration in Numerical, Analogue, and Conceptual Models

Geologists have proposed a wide variety of theoretical and analogue models that predict or rely upon hinge migration during folding. As early as 1962, Flinn suspected that the orientations of "fold axes" (fold hinges) and "axial planes" (hinge planes) did not remain constant throughout folding events. Treagus and Treagus (1981) expanded upon
Flinn's ideas and produced a comprehensive theoretical model illustrating the complex relationships between the fold form, orientation of the fold hinge, axial planar cleavage, and the finite strain ellipsoids within folded material. In the mid 1980's and early 1990's models illustrating the mechanics of fault-bend folding (Suppe, 1983), and fault-propagation folding (Suppe and Medwedeff, 1984; Jamison, 1987; Suppe and Medwedeff, 1990), were developed that predict hinge migration processes are a geometrical necessity during fault-related folding.

More recently there have been a series of studies that focus directly on modeling hinge migration during folding. Analogue, numerical, and conceptual studies illustrating the development of kink and chevron folds involving hinge migration processes, have been conducted by Stewart and Alvarez (1991), Fowler and Winsor (1996), and Bezar et al. (1998). The study by Bezar et al. (1998) also produced theoretical models that predict the activation of hinge migration processes during the development of drag folds and fault-propagation folds. Homza and Wallace (1995) produced theoretical models that involved hinge migration to explain the development of detachment folds, while Odonne and Vialon (1987) used analogue models to document the possibility of hinge migration during superimposed folding. Finally, Ghosh et al. (1996) used numerical and analogue models to explore the potential contribution of hinge migration processes in the development of structural domes and basins.

Although there is a growing wealth of natural and theoretical studies that test the probability and viability of hinge plane migration occurring during folding, very few published studies offer criteria for identifying folds whose hinges have migrated in natural settings. The five natural studies reviewed above used i) cleavage-bedding relationships, ii) the kinematic analysis of

pressure shadows, and iii) the analysis of boudinaged bedding to suggest that hinge plane migration occurred during deformation. Of these natural studies only Beutner and Diegel's (1985) pressure shadows technique definitively illustrated that hinge plane migration occurred during deformation. This technique and others, however, are site specific and difficulty to apply at other locations. With the exception of quantitative studies, such as those conducted by Treagus and Treagus (1981) and Ghosh et al. (1996), most theoretical studies do not provide criteria for identifying folds formed by natural deformation that have experienced hinge plane migration. The study described in this thesis uses the distribution of finite grain shape fabric/strain patterns throughout folded layers as a means for identifying the whether hinge plane migration was active during folding.

2.3. Definition and Types of Hinge Plane Migration

Hinge plane migration during folding is widely used to explain the development and final geometry of folds in natural and experimental settings. However, there is no formal definition for hinge migration during folding. Most studies use the term hinge migration during folding to indicate that there has been a change in the location or orientation of fold hinges during either initial or subsequent folding events. To understand the processes that contribute to hinge migration during folding, and further constrain the definition provided above, the kinematics of hinge migration and the reference frame from which most folds are viewed in both natural and experimental settings must be examined.

2.3.1. Kinematic Framework and Reference Frame of Hinge Plane Migration

In order to identify and classify the different kinematic processes active during fold hinge plane migration a reference frame and kinematic framework for deformation must be defined. Within most fold and thrust belts mesoscale folds are viewed in relation to the thrust sheet in which they formed. Within such a reference frame the direction of transport is generally considered to be towards the foreland of the thrust system (excepting any backthrusts etc.). Once a reference frame for deformation is defined, kinematic analysis of the mesoscale fold can provide valuable information about the type of deformation that produced the fold, including distinguishing between the kinematic processes associated with hinge plane migration. Without definition of a regional reference frame, such as the thrust sheet example described above, kinematic analysis of the types of hinge plane migration that were dominant during deformation is not possible.

2.3.2. Kinematics of Hinge Plane Migration Processes

Once a frame of reference for deformation has been defined, it is possible to identify four end-member kinematic processes associated with hinge plane migration during deformation. Three of

these kinematic processes are not formally described or defined by previous studies. These are dip-rotation, material translation, and lateral translation of the hinge plane (Fig. 5 a,b,c). Hinge migration by dip-rotation produces a change in the dip angle of the hinge plane during folding. This dip-rotation process is similar to a rug overlying a trap door in the floor, as the door is opened from underneath, the rug is folded and the door acts as the hinge plane in that fold (Fig. 6a). As the door is either raised or lowered, the angle of dip increases or decreases rotating the orientation of the trap door (hinge plane) and the overlying rug (rocks). Material translation hinge migration is the physical movement of material through the hinge regions of the fold during deformation with respect to a fixed external reference frame. The position of the hinge plane with respect to external coordinates remains constant, but the material or rock that occupies and defines the hinge of the fold moves through the point of maximum curvature and is replaced by material once found in the limb of the fold. This translation of material is similar to the movement of a conveyor belt at a store, the conveyor (material) moves while the rollers (hinge) it wraps around remain fixed in space (Fig. 6b). Finally, during lateral translation hinge migration the folded material and the dip angle of the hinge plane remain fixed with respect to a fixed reference frame, however, the position of the hinge plane along the fold changes with time, similar to the movement of a wave through water. The crest and trough deform the water molecules that they pass through, but do not transport the material through space (Fig. 6c).

Theoretical and experimental studies by Flinn (1962 p. 424), Treagus and Treagus (1981), and Ghosh et al. (1996) identify a fourth kinematic process of hinge plane migration, referred to in this study as strike-rotation hinge plane migration (Fig. 5d). During deformation the strike of the hinge plane changes orientation with respect to a fixed external reference frame, resulting in strike-rotation migration (Fig. 6d). Flinn (1962 p. 424) stated that during non-coaxial deformation, as soon as folding was initiated the hinge plane should rotate towards the direction of regional elongation (**X**). In an idealized fold and thrust system the **XZ** plane of regional deformation is a vertical plane oriented parallel to the direction of transport where **Z** is oriented in the direction of maximum regional shortening, and **Y** parallels the direction of strike along the thrust system. Treagus and Treagus (1981) produced an extensive study in which buckling was initiated as a result of stresses oriented oblique to the strike and dip of layering. Variations in the orientation of the resulting fold axes (or hinge planes) were related to the primary regional deformation axes (**X**, **Y**, and **Z**) rather than variation in competency contrasts. They found that the degree of strike-rotation hinge migration depends on the state of strain, initial layer attitude, and degree of initial

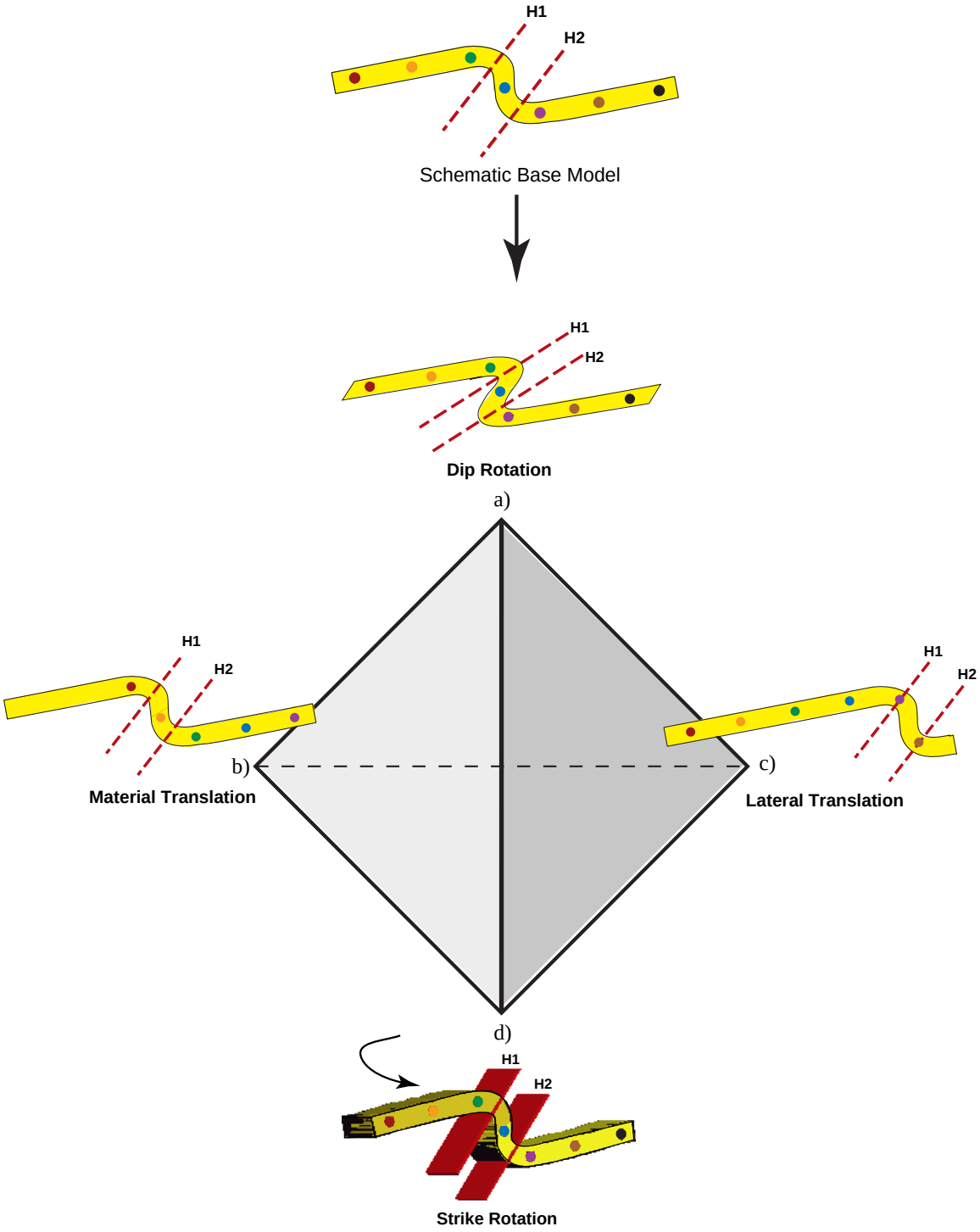

Fig. 5. Schematic representation of the end-member hinge migration kinematic processes, a) dip-rotation, b) material translation, c) lateral translation, and d) strike-rotation.

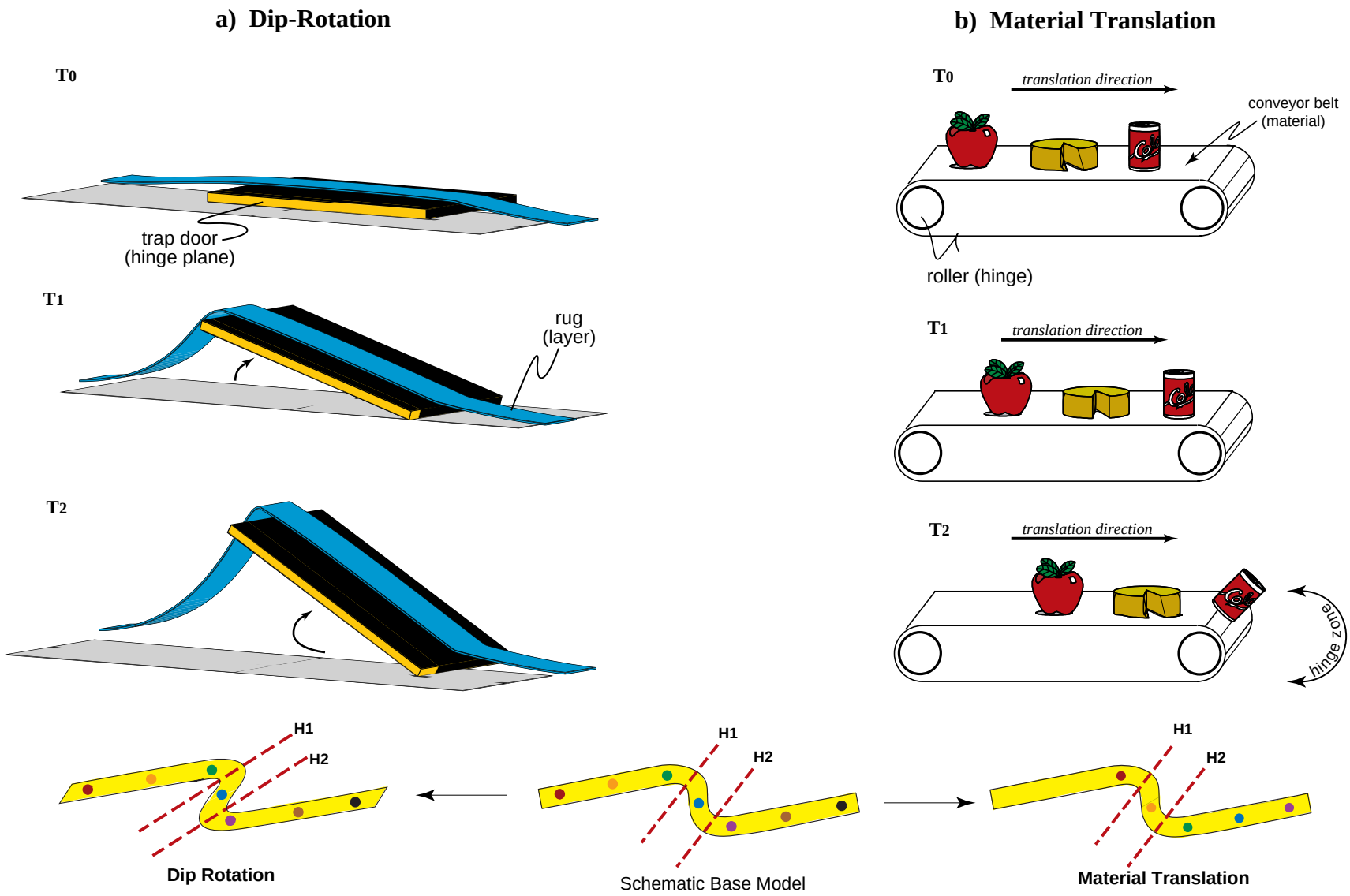

Fig. 6. a) Example of dip-rotation hinge migration in which a horizontal planar surface, such as a trap door, changes its angle of dip with respect to horizontal. An overlying layer, such as a rug, is deformed as a result of the dip-rotation. b) Example of material-translation. The conveyor belt (material) is passively translated around the rollers (hinge) of the system.

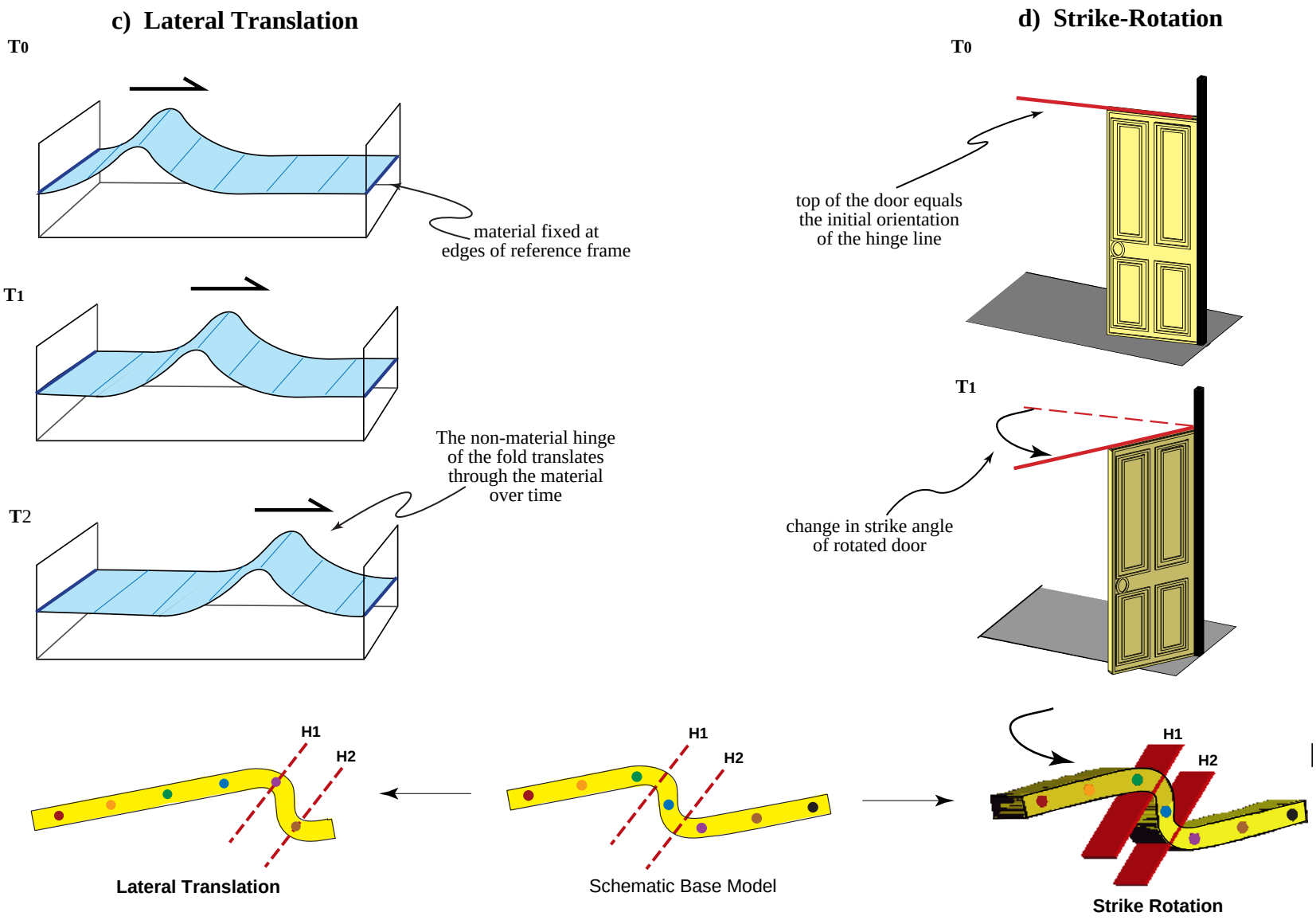

Fig. 6 c) Lateral translation HPM - the crest and hinge of the wave move through space, but the material it is deforming is not translated with it. d) Strike-rotation HPM - the hinge plane is visualized as a door in a door frame, when the door is swung open or closed the strike of the door (hinge plane) changes.

irregularities in the layering. Their models also predicted that folds experiencing constrictional strains during deformation contained fold axes that were strongly oblique to the **XY** regional deformation plane, while folds that experienced flattening strains during deformation contained fold axes parallel to the **XY** regional deformation plane. Treagus and Treagus (1981) also observed that oblique layers experiencing constrictional deformation produced non-cylindrical folds, with curving hinge planes as a result of strike-rotation hinge-plane migration (HPM). Ghosh et al. (1996) extended the studies of strike-rotation HPM to include the effects of competency contrasts between units. They argued that HPM is only active as long as tightening during folding continues, and reported that competency contrasts between layers greatly affects hinge migration during deformation. Much of their study agrees with the results of the Treagus and Treagus' (1981) work. Ghosh et al. found that large degrees of strike-rotation HPM are possible during constrictional deformation, and that it was harder to activate strike-rotation HPM during flattening or plane strain deformation. This is consistent with Treagus and Treagus' (1981) finding that the value of *k'* , or the measure of ellipsoid shape, increased from general flattening strains to plane strains and into constrictional strains as the degree of strike-rotation HPM increased. k' used in their study was defined by Flinn (1962) as:

$$k' = \ln\left(X/Y\right) / \ln\left(Y/Z\right) \qquad (1)$$

where *X*, *Y*, and *Z* are the maximum, intermediate and minimum principal strain axes respectively.

2.3.3. Material Versus Non-Material Hinge Plane Migration

As was illustrated above, there are four end-member kinematic processes that can contribute to hinge migration during deformation: i) HPM dip-rotation, ii) HPM strike-rotation, iii) HPM material translation, and iv) HPM lateral translation. Each of these processes may act individually or together in various combinations to produce hinge plane migration during deformation. Treagus and Treagus (1981) modeled HPM strike-rotation as the migration of a non-material or material plane during deformation. During non-material deformation the position of the hinge plane changes through time but the position of the material (rock layers) remains fixed with respect to an external reference frame. Migration of a material plane during deformation involves the change in location of material (rock layers) through time with respect to an external reference frame. HPM material translation is only produced by the migration of a material plane while HPM lateral translation only occurs through the migration of a non-material plane. HPM by strike-rotation and dip-rotation can result from migration of a material and/or a non-material plane during deformation. In natural deformation, a combination of two or more of these kinematic processes discussed above probably contributes to the migration of hinge planes during deformation. When

viewed from a fixed external reference frame, such as geographic coordinates, the kinematic analysis of a fold that has experienced hinge plane migration during deformation, can help determine which kinematic process(es) of hinge migration were active during deformation.

3. Geologic Setting

3.1. Blue Ridge Province, Northwest North Carolina

The mesoscale fold investigated in this study (the Clinchfield Railroad fold) crops out in the southern Blue Ridge province of northwestern North Carolina (Fig. 7). The southern portion of the Blue Ridge province is composed primarily of Grenvillian basement massifs emplaced during Paleozoic contractional deformation events that resulted in northwestward directed thrusting and folding. Recent seismic profiles and geologic mapping indicate that the Blue Ridge Province is completely allochthonous (Cook, 1979; Rankin, et al., 1991).

Rocks exposed within the Clinchfield Railroad fold are meta-quartzites of the Erwin Formation, the uppermost member of the early Cambrian Chilhowee Group (Simpson and Eriksson, 1989). The Clinchfield Railroad fold crops out in the Tablerock thrust sheet which is exposed in the southwestern corner of the Grandfather Mountain Window (Fig. 7) (Bryant and Reed, 1970). The Grandfather Mountain Window, first recognized by Jonas (1932) formed as a result of erosion through the Linville Falls fault and is only partially exposed within the Grandfather Mountain Window (Bryant and Reed, 1970; Boyer and Mitra, 1988). Within the window the Tablerock thrust places Early Cambrian rocks of the Chilhowee Group over late Precambrian sedimentary and volcanic rocks of the Grandfather Mountain Formation (Bryant and Reed, 1970; Rankin et al., 1970; Hatcher and Butler, 1986). Field relationships and a Rb-Sr whole rock isochron age of 302 Ma from mylonites along the Linville Falls fault indicate that movement along both the Linville Falls and Tablerock faults occurred during the Alleghanian Orogeny (Bryant and Reed, 1970; Van Camp and Fullagar, 1982; Boyer and Mitra, 1988; Hatcher et al., 1989; Hatcher and Goldberg, 1991). During deformation, rocks within the Tablerock thrust sheet experienced biotite grade, greenschist facies metamorphism (Fig. 8) (Hatcher and Goldberg, 1991). Field relations and greenschist facies assemblages from mylonites along the Linville Falls and Tablerock faults suggest that greenschist facies metamorphism of the Grandfather Mountain Formation and the Chilhowee Group in the Grandfather Mountain Window accompanied Alleghanian thrusting and folding (Bryant and Reed, 1970; Van Camp and Fullagar, 1982; Dallmeyer et al., 1986; Hatcher and Goldberg, 1991; Trupe, 1999). Therefore, folding of the Erwin Formation at the study site, and throughout the Tablerock thrust sheet, accompanied movement along the Tablerock thrust fault during the Alleghanian Orogeny (Bryant and Reed, 1970; Hatcher et al., 1989). Within the Grandfather Mountain Window the Chilhowee and Shady formations are cut by unmetamorphosed and undeformed early Mesozoic dikes (Bryant and Reed,

1970). This relationship indicates that following movement along the Tablerock thrust during the Alleghanian Orogeny no major penetrative deformation affected the rocks of the Tablerock thrust sheet.

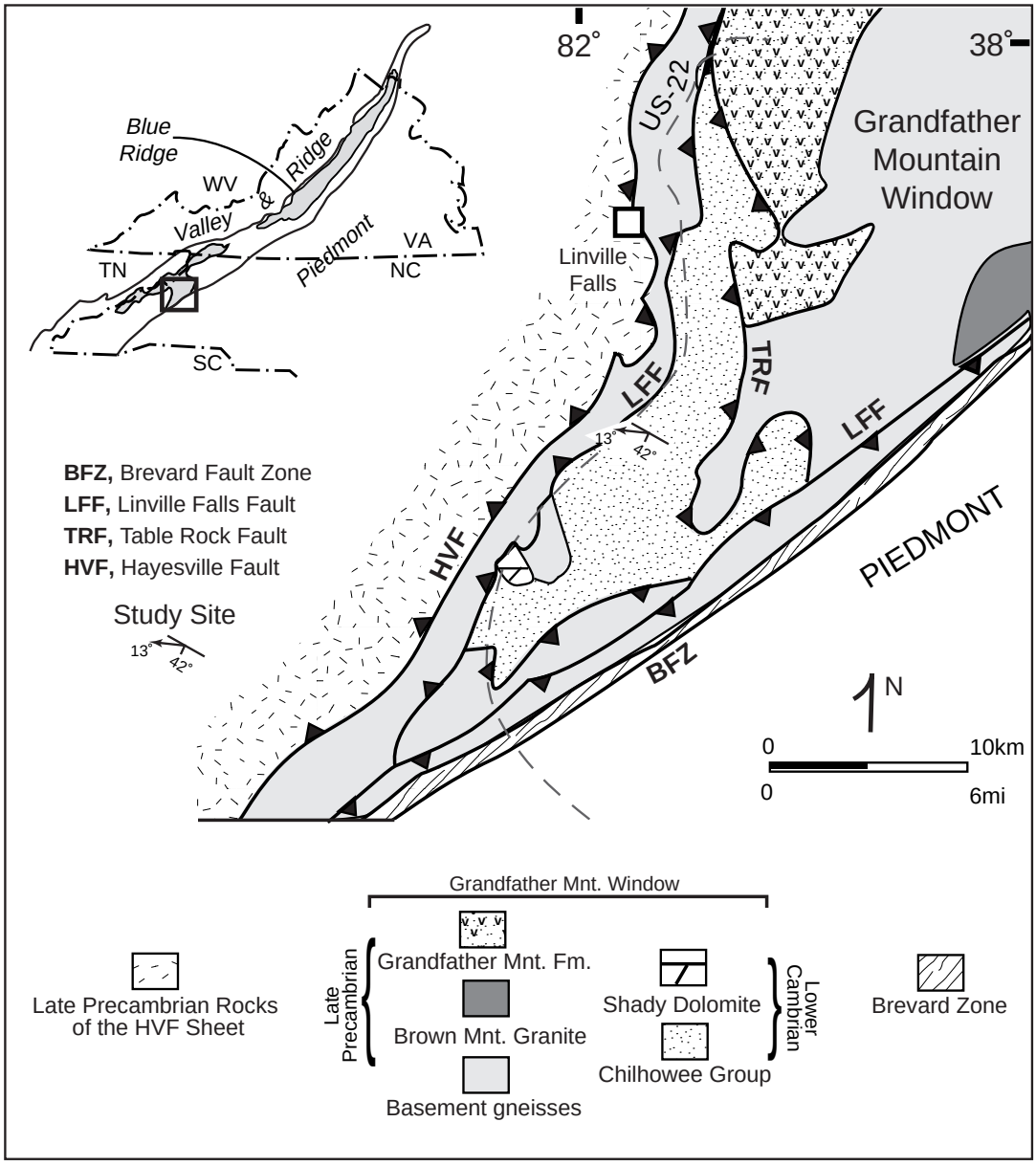

Fig. 7. Regional reference map and geologic map of the study area (after Hatcher and Butler, 1986). The Grandfather Mountain Window is bounded by the Linville Falls fault (LFF). The study fold crops out in the underlying Tablerock thrust sheet (stippled pattern). The location of the fold is indicated by the orientation symbol. The hinge plane and fold axis are indicated.

3.2. Characterization of Clinchfield Railroad Fold

The Clinchfield Railroad fold is a mesoscale (amplitude of ~3.5 meters and half-wavelength of ~4.5 meters), asymmetric, antiformal fold located at 35˚, 54', 22" North latitude and 81˚, 56', 50" West longitude. The fold is near-cylindrical, verging north with a 48˚ interlimb angle. The fold (hinge) axis trends 297˚, plunging at 13˚ and the axial plane (hinge plane) strikes 312˚, dipping at 42˚ to the southwest, and shallowing downwards towards the inner layers of the fold (Fig. 9a & c). Contacts with more pelitic units, along strike from the study site, parallel the foliation observed within the fold. This field relationship suggests that the foliation planes that define the layering in the Clinchfield Railroad fold and original sedimentary bedding are coincident. Cleavage and macroscopic lineation are absent at the study site. Two sets of planar joints (oriented at 015˚, 80˚W and 060˚, 75˚SE) cross cut the Clinchfield Railroad fold (Fig. 9b). Based on field relationships, Bryant and Reed (1970) concluded that these and other joint sets formed after folding of the Tablerock thrust sheet, and are not related to the deformation that produced the Clinchfield Railroad fold.

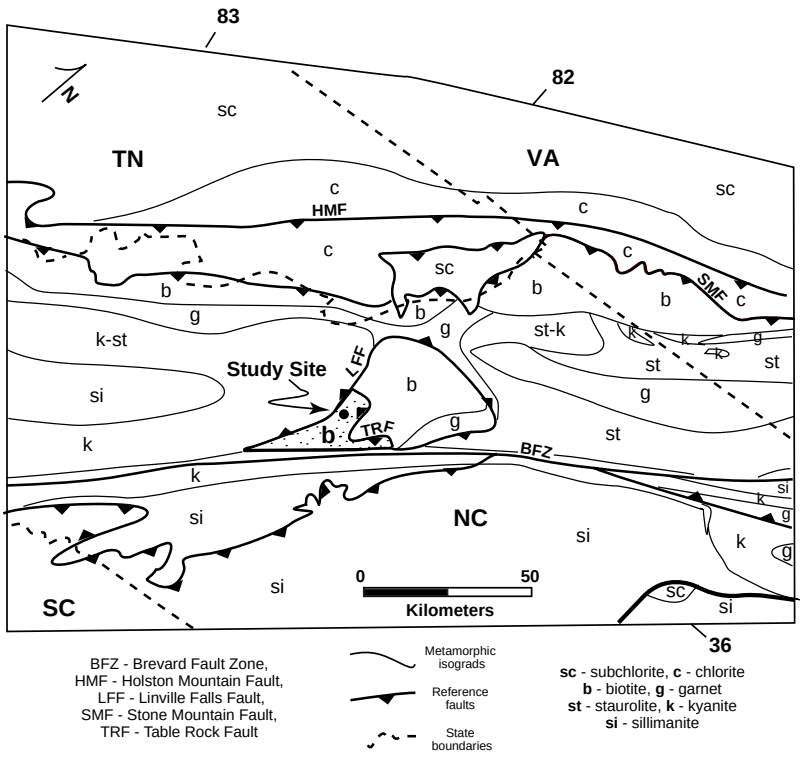

Fig. 8. Metamorphic isograd map of the Grandfather Mountain Window region, southern Appalachians (after Hatcher and Goldberg, 1991). Rocks at the study location crop out in the Tablerock thrust sheet, indicated by the stippled pattern, and experienced biotite grade, greenschist facies metamorphism during the Alleghanian Orogeny.

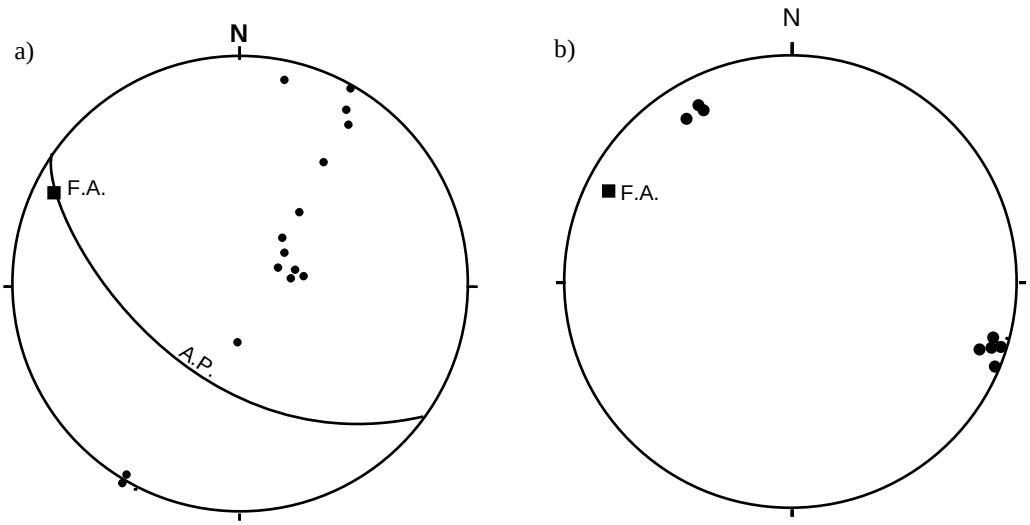

Axial Plane, 312˚, 42˚ SW
■ Fold Axis, 13˚, 297˚
• Poles to bedding n=13
Joints ● n=8

c)

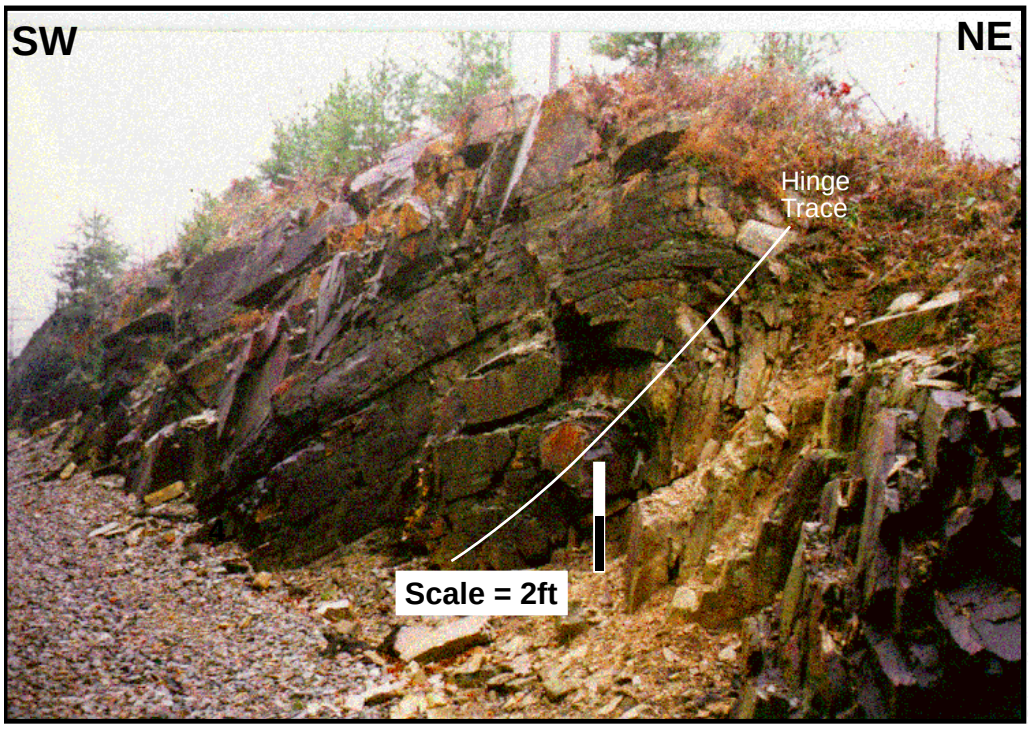

Fig. 9. a) Orientations of poles to bedding, axial plane (A.P.), and fold axis (F.A.) projected on an equal area stereoplot for the Clinchfield Railroad fold; b) Poles to joints projected on an equal area stereoplot for the Clinchfield Railroad fold; c) Clinchfield Railroad fold viewed approximately along strike of the axial plane.

4. Methods and Results

Using a representative suite of samples across the profile of the Clinchfield Railroad fold a detailed analysis of the grain scale deformation associated with folding was acquired from petrographic based techniques. Thin section based analyses were carried out to obtain information about: i) composition, ii) operative deformation mechanisms, iii) crystal preferred orientation fabric, and iv) average three-dimensional grain shape fabric at each sample location.

4.1. Sample Acquisition and Preparation

Five oriented samples of Erwin quartzite were taken from the same bedding plane within the Clinchfield Railroad fold (Fig. 10). Samples were obtained from both of the limbs and from the hinge zone: i) lower upright limb (sample number **4**), ii) upper upright limb (**1**), iii) hinge zone (**2**), iv) upper overturned limb (**3**), and v) lower overturned limb (**5**). Three, mutually perpendicular thin sections were cut from each sample and were oriented with respect to the strike and dip of foliation at each location (Appendix VIa). The "a" thin section planes were cut perpendicular to the strike of foliation for each sample; "b" thin sections plane were cut parallel to strike but at 90˚ to foliation for each sample; the "c" thin section planes lie within the foliation plane at each sample location (Fig. 10).

4.2. Petrographic Analyses

Each suite of thin sections was examined under plain and cross polarized light on a standard petrographic microscope in order to identify the microstructures, the general orientation of the grain shape fabric (Appendix I), and the average size of grains present in each sample suite. The average mineral composition of each sample was obtained from microscopic point counts conducted on the "a" thin section plane of each sample. 200 data points were identified and counted from each sample.

4.2.1. Petrographic Analyses - Results and Data Presentation

The only rock type found within the Clinchfield Railroad fold is the Erwin quartzite. Petrographic point count analyses of the "a" thin section plane from each sample reveal that there is less than 2% matrix material in any of the five samples (Fig. 11). This matrix material is dominantly composed of sericite, fine grained quartz, chlorite, and feldspar grains. The quartz grains (>98%) are almost completely recrystallized. The long axes of these recrystallized grains range from 0.05mm to 0.5mm in length. Feldspar grains, when present, are more equant in shape than the quartz grains. Their grain boundaries are not, however, euhedral and grains are either fractured or have alteration rims of white mica and fine grained quartz. Internally, most feldspar grains exhibit perthitic twins.

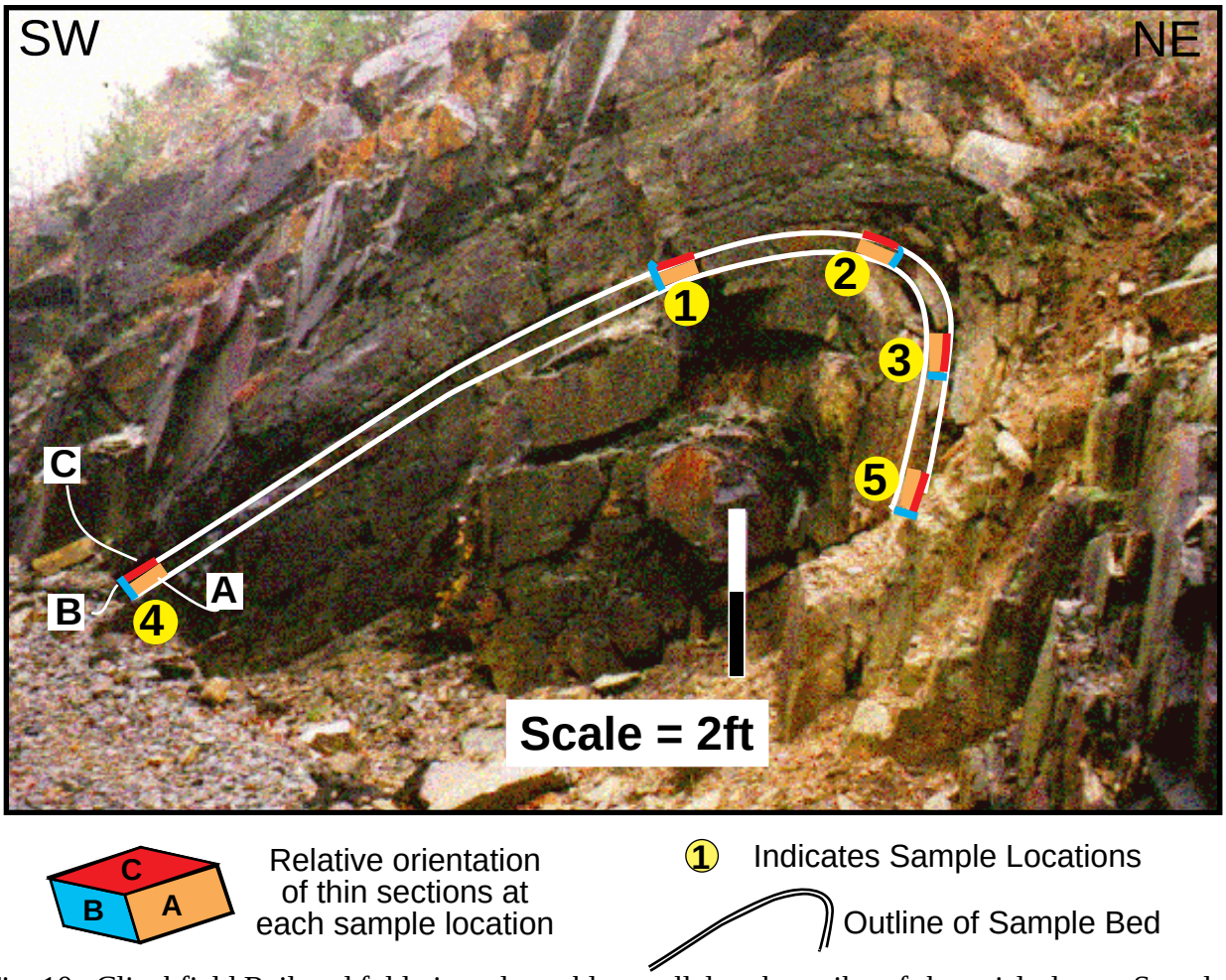

Fig. 10. Clinchfield Railroad fold viewed roughly parallel to the strike of the axial plane. Sample bed and sample locations are indicated on the photograph. Relative orientation of thin section planes at each sample location are indicated as "a" (orange), "b" (blue), and "c" (red).

Sample Number	809-1a	809-2a	809-3a	809-4a	809-5a
Recrystallized Quartz	98%	98 %	98%	98%	99%
Micas, Opq. & FG Qtz	2%	2 %	2%	2 %	1%
Number of points	200	200	200	200	200

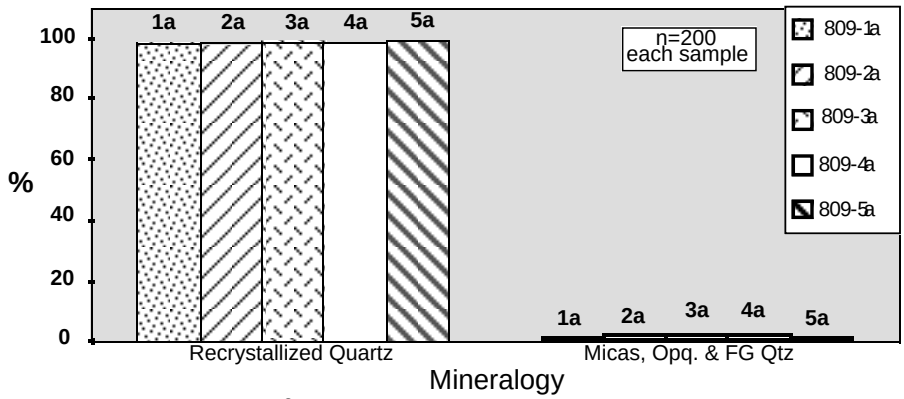

Fig. 11. The Erwin Formation of the Chilhowee Group is a clean quartz arenite or quartzite. A histogram illustrates the mineral composition point count results from each sample.

The shape of the quartz grains varies between section planes but is uniform within each plane. In all of the section planes quartz grains display undulose extinction, evidence of internal deformation. Two of the section planes in each sample display preferred orientation of elongate quartz grains, the third section plane usually contains more equant, blocky quartz grains. The size of quartz grains in each section plane is uniform, with the exception of infrequent finer grained recrystallized quartz bands that cross cut a few of the samples oblique to the primary fabric in that thin section. In all thin sections, quartz grains display undulose and uniform extinction patterns in approximately equal abundance to one another. The boundaries of quartz grains are irregular and sutured, or equant along one or more boundaries (Fig. 18a) (Table 1).

Throughout each sample suite, remnant or "ghost" grains are present. The ghost grains appear in two different forms. The first type is a group of recrystallized quartz grains that, in certain orientations on the microscope stage, rotate into or out of extinction together. In all other orientations, these grains have different interference patterns. The second type of ghost grains are made up of a large (up to ten times the size of the recrystallized quartz grains), dominantly unrecrystallized central quartz grain that is bounded by a mantle of subgrains or extensive areas of undulose extinction. Relative to the first type of ghost grains, the second type of ghost grains are less common.

Table 1. Presence (X) or absence (-) of primary microstructures in each sample suite. Samples listed in order of their location around the fold profile (see Fig. 10).

Sample #	Undulose Grain Boundaries	Subgrains	Undulose Extinction	Fine Grained Quartz Bands	Fractures & Veins	"Ghost" Grains	Pressure Solution Seams	Inclusion Trails
4	X	X	X	-	X	X	-	–
1	X	X	X	X	X	X	-	-
2	X	X	X	-	X	X	X	-
3	X	X	X	X	-	X	X	X
5	X	X	X	X	X	X	-	-

Other less common microstuctures include i) randomly oriented, fine grained, quartz bands, veins or fractures, ii) poorly developed pressure solution seams, and iii) fluid inclusion trails. The presence or absence of each of the microstrictures described above for each thin section suite, are listed in Table 1.

4.3. Crystal Preferred Orientation Analysis

Crystal preferred orientation (CPO) analyses were conducted on quartz grains from the "c" thin section plane of each sample, which lies within the foliation plane at each sample location. These analyses involved measuring the c-axis orientation of 450-500 quartz grains from each

sample. Single grain measurements were collected from each sample using standard universal stage techniques (Turner and Weiss, 1963). Each data plot is displayed on an equal area, lower hemisphere spherical projection plot.

4.3.1. Crystal Preferred Orientation - Results and Data Presentation

Neither macroscopic cleavage nor lineation are visible at the study site; therefore, an alternative reference frame was used to produce pole figure crystal preferred orientation (CPO) stereoplots. Two sets of CPO stereoplots are presented for each sample. In the first set of stereoplots (Figs. 12a-16a) foliation, is plotted as the primitive circle. The orientations of *X*, *Y*, and *Z*, the calculated principal axes of the average grain shape ellipsoid, and the fold axis are indicated on each plot . The second set of CPO plots (Figs. 12-16b) were obtained by rotating the data into a reference frame defined by the average grain shape axes. Rotations were carried out using the program FABRIC 1.2. developed by Starkey (1989). These data plots use the traditional *XYZ* reference system where *X* and *Z* lie along the primitive and *Y* plots at the center of the stereoplot.

4.4. Grain Shape Fabric Analysis

For each sample the average triaxial grain shape fabric ellipsoid was calculated by combining average grain shape ellipses from the three mutually perpendicular thin section planes at each sample location (Appendix II). The two-dimensional grain shape fabric for each thin section was determined by measuring the ratio of the long to short axes (R_f) and orientation (ϕ) of individual grain long axes. R_f/ϕ analysis separates the effects of original ellipticity (R_i) from the strains associated with tectonic deformation (R_s) (Ramsay, 1967). This method, first described by Ramsay in 1967, has since been modified by Dunnet (1969), Lisle (1985), De Paor (1988) and others. Since 1967, Rf/ϕ analysis has become the most commonly used method of strain/grain shape fabric analysis and its reliability has withstood comparison against other commonly used methods of strain analysis and theoretical tests (Lisle, 1985). The use of strain analysis techniques for calculating average grain shape fabric ellipsoids within recrystallized aggregates was previously demonstrated in experimentally deformed quartzites by Miller and Christie (1981) and in natural samples by Platt and Behrmann (1986) and Tagami and Takeshita (1998).

Basic assumptions made by this method of strain/grain shape analysis include: i) the original strain markers possessed an initial circular or elliptical shape with an aspect ratio (R_i) and variable orientation (θ), ii) the markers subsequently deformed with their matrix, iii) strain was homogeneous on the scale of the specimen, and iv) the pattern of the strain markers on the Rf/ϕ plot is a function of the strain/grain shape ellipse and the initial eccentricity (θ) of the markers. Rf/ϕ calculations in this study were completed using the method modified by De Paor (1988). De

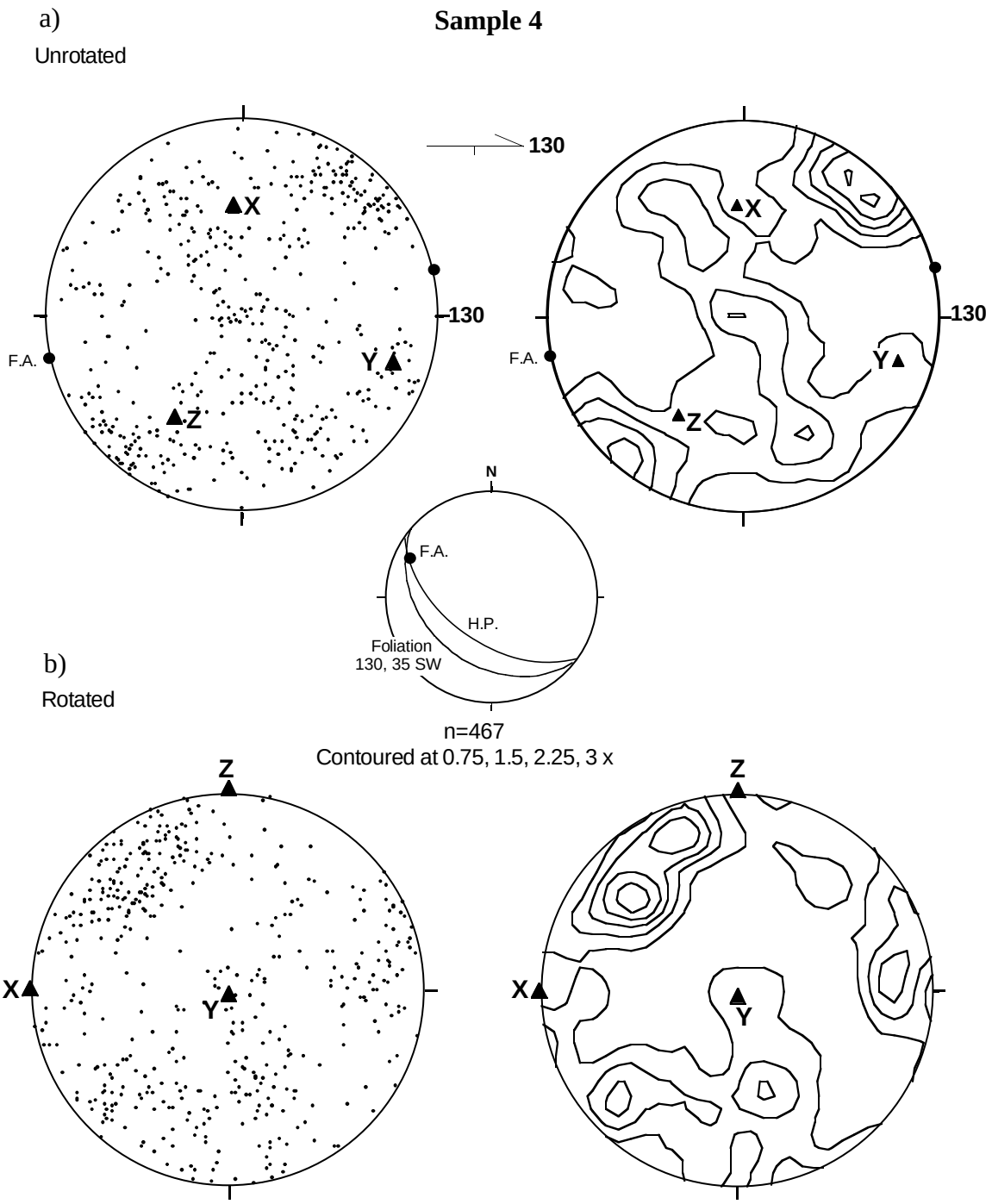

Fig. 12. Quartz c-axis fabric diagram for sample **4** (thin section 809-4c); equal area, lower hemisphere projection, a) CPO plot within the foliation plane, b) CPO plot semi-traditional projection. Note in a) the orientation of the fabric diagram with respect to the fold axis projection.

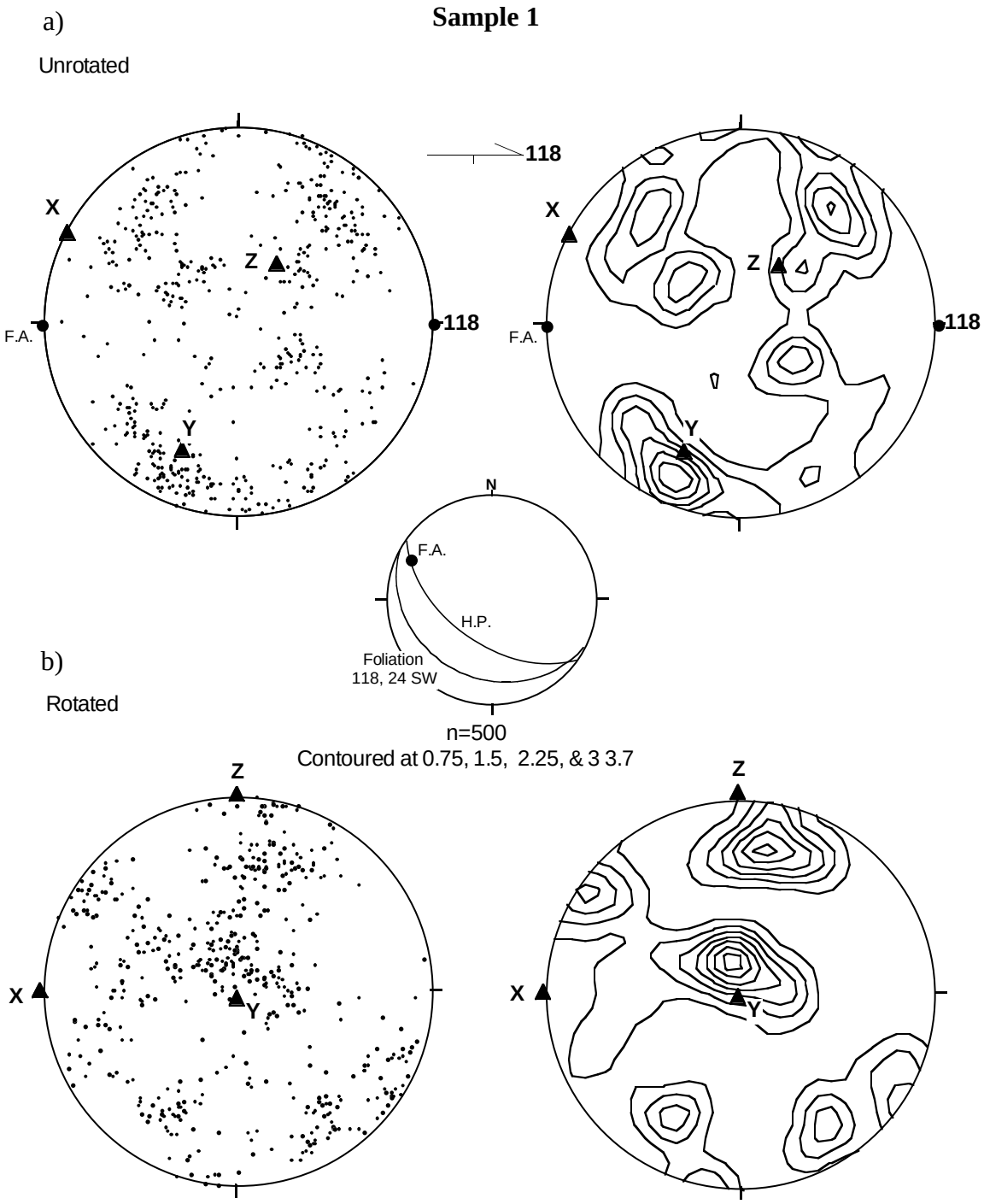

Fig. 13. Quartz c-axis fabric diagram for sample **1** (thin section 809-1c); equal area, lower hemisphere projection, a) CPO plot within the foliation plane, b) CPO plot semi-traditional projection. Note in a) the orientation of the fabric diagram with respect to the fold axis projection.

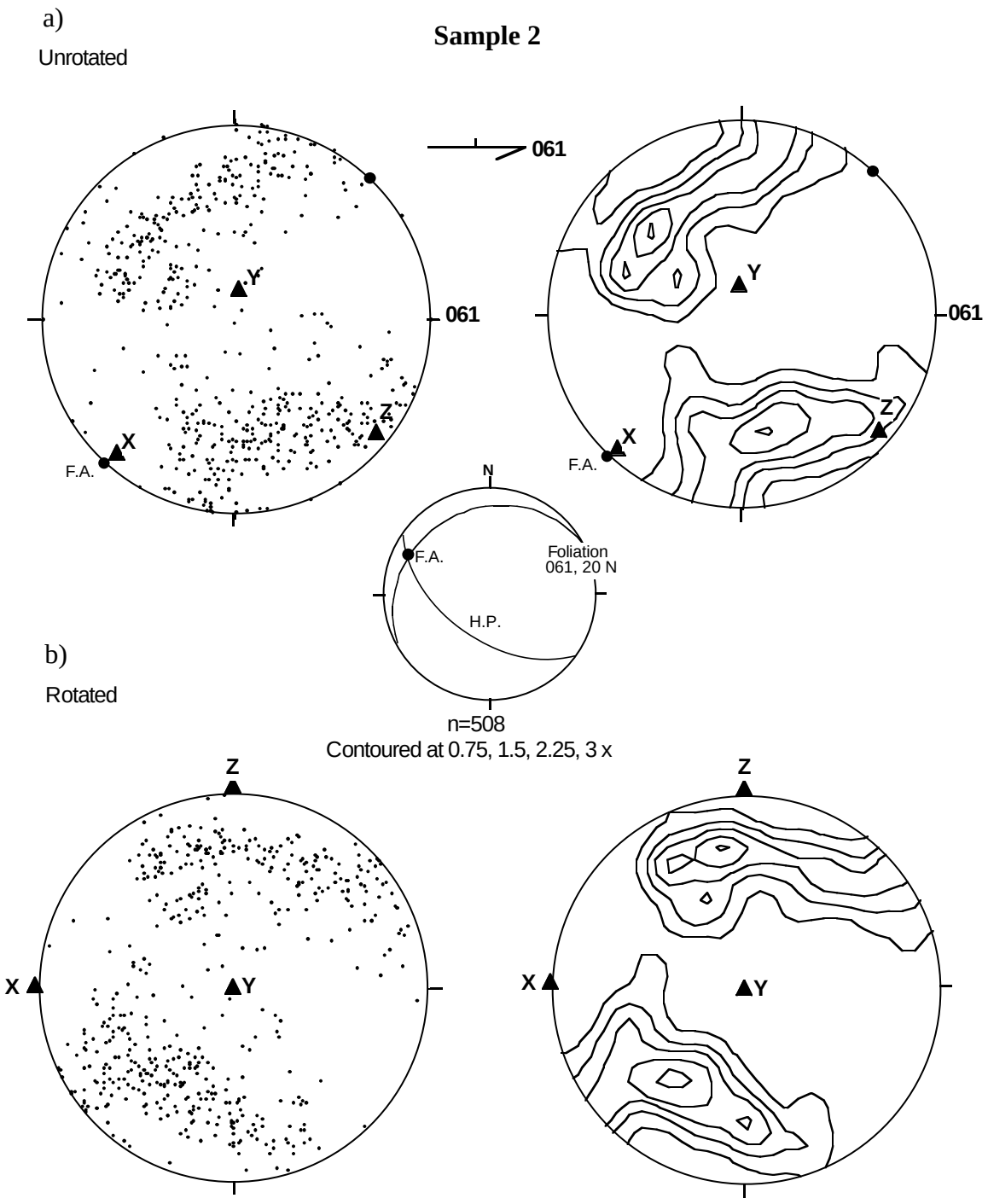

Fig. 14. Quartz c-axis fabric diagram for sample **2** (thin section 809-2c); equal area, lower hemisphere projection, a) CPO plot within the foliation plane, b) CPO plot semi-traditional projection. Note in a) the orientation of the fabric diagram with respect to the fold axis projection.

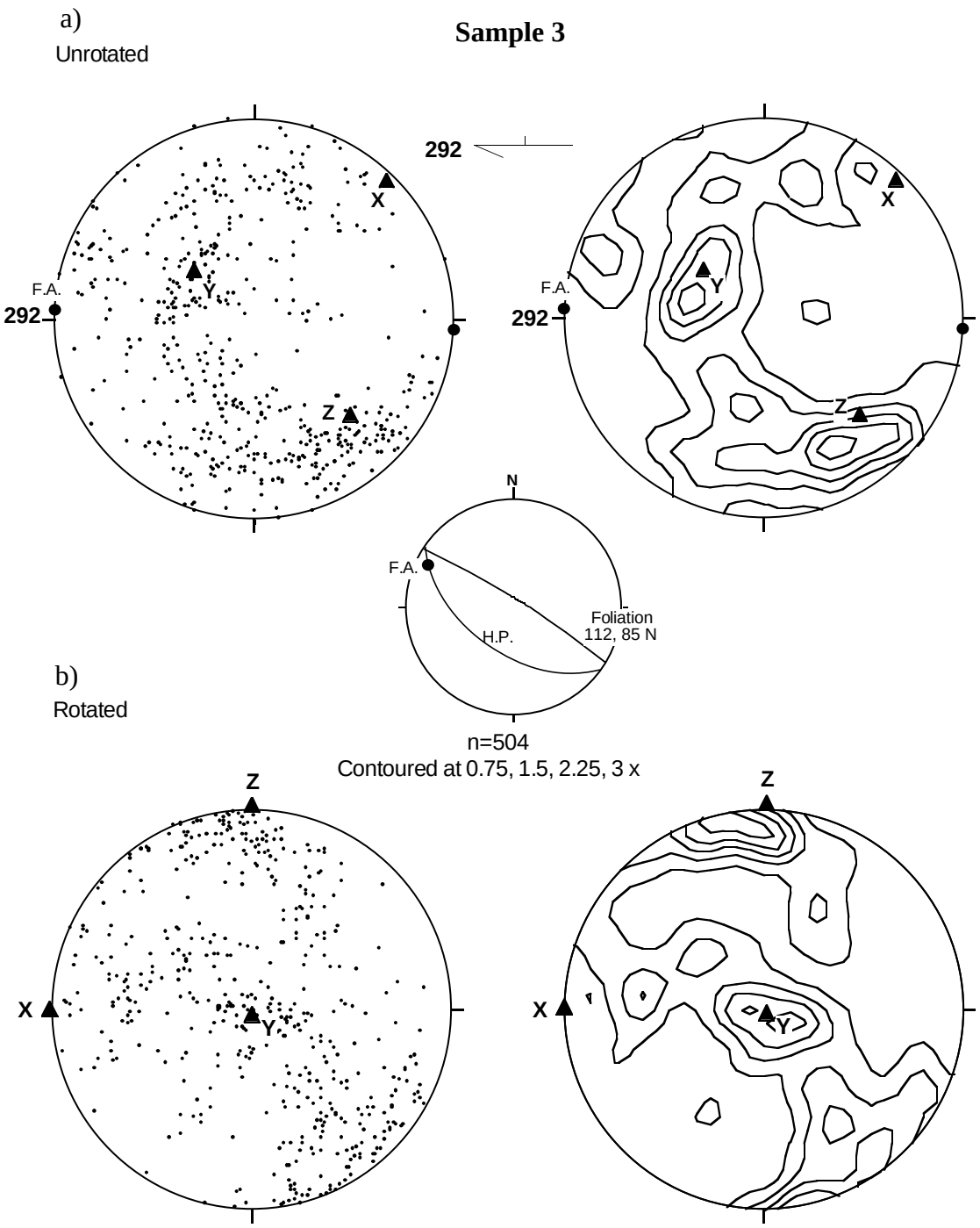

Fig. 15. Quartz c-axis fabric diagram for sample **3** (thin section 809-3c); equal area, lower hemisphere projection, a) CPO plot within the foliation plane, b) CPO plot semi-traditional projection. Note in a) the orientation of the fabric diagram with respect to the fold axis projection.

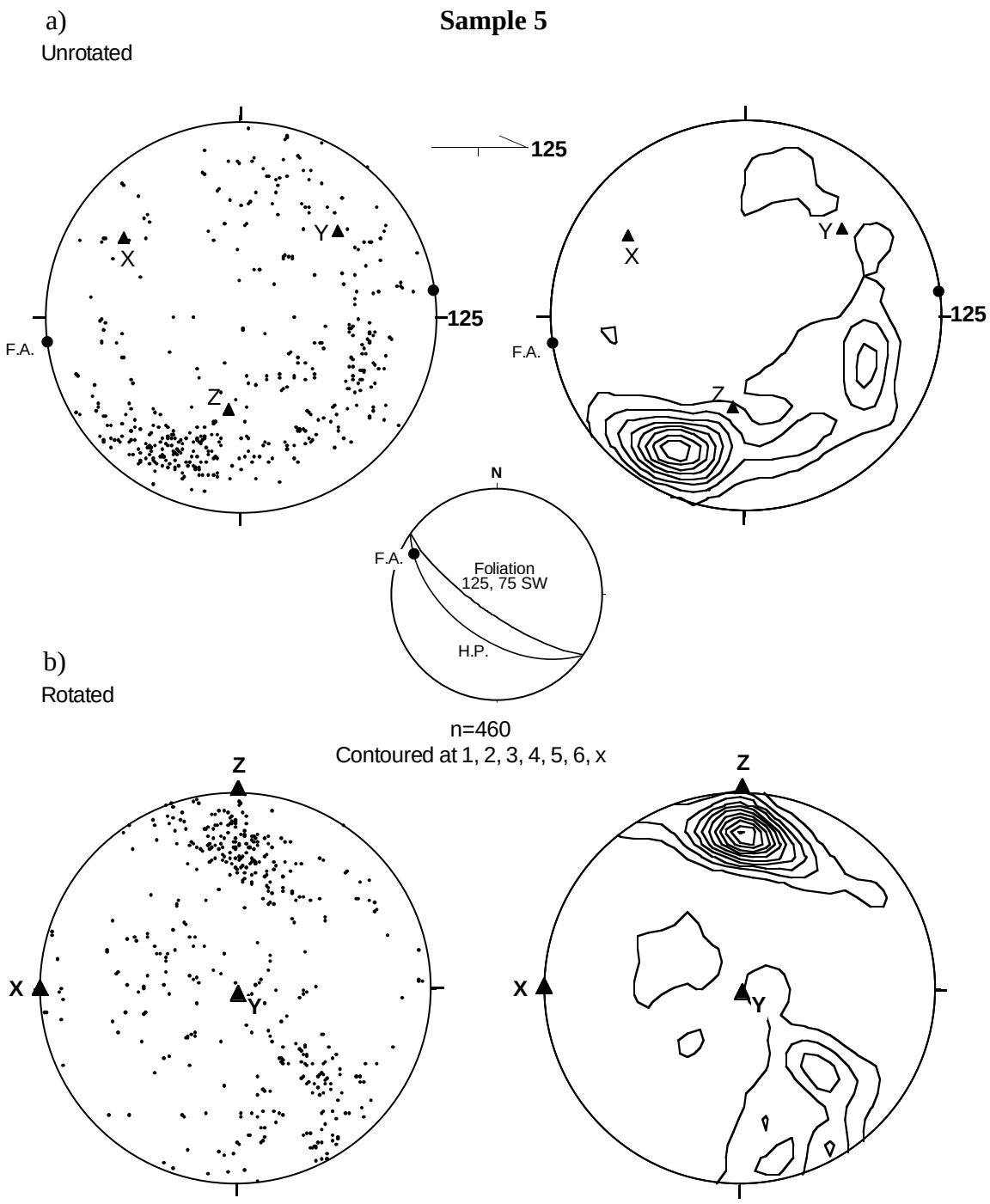

Fig. 16. Quartz c-axis fabric diagram for sample **5** (thin section 809-5c); equal area, lower hemisphere projection, a) CPO plot within the foliation plane, b) CPO plot semi-traditional projection. Note in a) the orientation of the fabric diagram with respect to the fold axis projection.

Paor's method of Rf/ϕ analysis using a hyperbolic stereonet (Appendix III), meets the criteria and assumptions of earlier Rf/ϕ methods but is more readily graphed and solved (see De Paor, 1988 for further details).

Calculations of R_s, the axial ratio of the imposed grain shape ellipse, and ϕ, orientation of the deformed grain shape ellipse, for each thin section, (Appendix IIb) were conducted using the computer program Rf/fry 2.0.6 (De Paor and Simpson, 1987) which is based on De Paor's 1988 Rf/ϕ method of grain shape fabric analysis**.** Calculated values for R_s and ϕ were compared to the optical estimations of R_s and ϕ for each thin section. Incompatibilities between the shape fabric ellipses calculated for the three sections for each sample were resolved using the program 2D-3D Compatibility 2.0 (Appendix IIc). This program prepares two dimensional section data for use in determining the triaxial grain shape fabric ellipsoid by resolving minor incompatibilities in the magnitude and orientation between the three average sectional ellipses for each sample (De Paor, 1994). De Paor, 1990, discusses the theoretical foundation for this correction in detail.

Table 2. List of variables and terms

Terms:	
X	Axis of maximum regional elongation
Y	Intermediate axis of regional deformation
Z	Axis of minimum regional shortening
R_I	Initial aspect ratio of grain shape ellipse
R_f	Final aspect ratio of grain shape ellipse
R_s	Aspect ratio imposed on grain shape ellipse
θ	Initial orientation of grain shape ellipse's long axis
ϕ	Imposed orientation of grain shape ellipse's long axis
X	Maximum principal grain shape ellipsoid axis, orientation and magnitude
Y	Intermediate principal grain shape ellipsoid axis, orientation and magnitude
Z	Minimum principal grain shape ellipsoid axis, orientation and magnitude
k	Measure of the grain shape fabric symmetry, Flinn's strain symmetry parameter
ε_s	Natural Octahedral Unit Shear, Nadai, 1963
ν	Lode's Parameter, Lode, 1926
I	Fabric Intensity, Lisle, 1985
1	Sample 809-1
2	Sample 809-2
3	Sample 809-3
4	Sample 809-4
5	Sample 809-5
γ_1	Main layer parallel shear, Coward and Potts, 1983 (Fig. 24b)
γ_2	Differential shear, Coward and Potts, 1983 (Fig. 24b)

Two dimensional section data were used to calculate the average triaxial grain shape fabric ellipsoids (Appendix IId) at each sample location using 2D->3D Strain (Kanagawa, 1992). This

program calculates the average magnitude and orientation of strain/grain shape ellipsoid axes (X, Y, and Z) from any three orthogonal or non-orthogonal section planes where the axial ratios (R_s) and long-axis orientations (ϕ) of the average grain shape fabric in each section are known (Kanagawa, 1992). 2D->3D Strain calculates the average grain shape fabric ellipsoid using Wheeler's (1986) tensor algebraic method and Milton's (1980) normalized final average ellipsoid method. A more detailed "cookbook" review of the procedure used to calculate the average, triaxial, grain shape fabrics determined in this study are included in Appendix IV.

4.4.1. Grain Shape Fabric Analysis - Results and Data Presentation

Because the Erwin quartzite at the study location experienced almost complete recrystallization during deformation the "strains" calculated in this study do not reflect the finite strains imposed on the quartzites in each sample (Platt and Behrmann, 1986; Tagami and Takeshita, 1996). The orientations and magnitudes of the principal triaxial, grain shape axes calculated for each sample location are used for relative comparison purposes only in this study.

The principal grain shape data, listed in Table 3, are analyzed graphically in Figure 17. Both Flinn and Nadai plots are used to compare and contrast the three dimensional states of the average grain shape fabric ellipsoids. Flinn plots are based on the ratios of the principal axes of the grain shape ellipsoids (Flinn, 1962). Nadai plots compare the natural octahedral unit shear ($\bar{\varepsilon}_s$) and the Lode's parameter (ν), where:

$$\bar{\varepsilon}_s = \left(\frac{\sqrt{3}}{2}\right)\left[\frac{2}{3}\left[\left(\ln\left(\frac{X}{Y}\right)\right)^2 + \left(\ln\left(\frac{Y}{Z}\right)\right)^2 + \left(\ln\left(\frac{Z}{X}\right)\right)^2\right]^{\frac{1}{2}}\right], \qquad (2)$$

Nadai (1963) and,

$$\upsilon = \frac{\ln\left(\frac{Y}{Z}\right) - \ln\left(\frac{X}{Y}\right)}{\ln\left(\frac{X}{Z}\right)}, \qquad (3)$$

(Ross, 1973). Nadai's (1963) natural octahedral unit shear (grain shape magnitude) is proportional to the eccentricity of the grain shape ellipsoid and provides a measure of strain magnitude. Lode's parameter, originally derived by Lode (1926) and modified by Ross (1973), describes the shape or symmetry of the grain shape ellipsoid. On Flinn Plots the symmetry of the grain shape fabric ellipsoid is defined by k. Throughout the literature there is much confusion regarding the form of Nadai's (1963) natural octahedral unit shear equation ($\bar{\varepsilon}_s$). A complete re-derivation of $\bar{\varepsilon}_s$ is included in Appendix V.

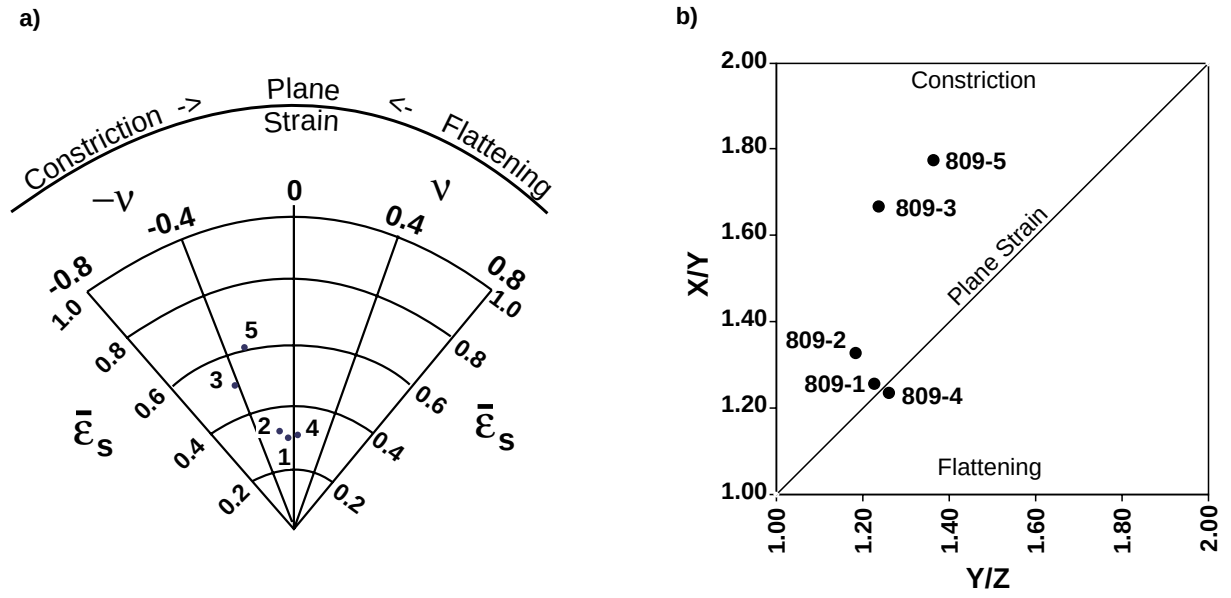

Fig. 17. a) Nadai (natural) Strain Plot and b) Flinn Plot. Each plot independently confirms the strain conditions recorded within each sample of the Clinchfield Railroad fold. The upright limb of the fold (sample 4) plots close to the plane strain line of deformation. The strain conditions of samples progressively taken along the upright limb, through the hinge and into the overturned limb of the fold plot along a semi-circular path up and into the constrictional field of deformation.

Table 3. Calculated values of grain shape fabric axes, magnitudes and symmetries.
Samples listed in order of their location around the fold profile (see Fig. 10).

	Principal Grain Shape Axes (Magnitude, Plunge & Trend)			$k = \frac{X/Y-1}{Y/Z-1}$	Strain Magnitude	Lode's Number	Fabric Intensity (Lisle, 1985)	
Sample #	X	Y	Z	$\boldsymbol{k}$	$\bar{\varepsilon}_S$	ν	$\boldsymbol{I_{gsf}}$	$\boldsymbol{I_{cpo}}$
4	1.245 10˚, 038˚	1.004 24˚, 132˚	0.800 64˚, 287˚	0.94	0.313	0.027	0.080	0.086
1	1.261 09˚, 143˚	1.002 51˚, 244˚	0.821 38˚, 026˚	1.17	0.304	-0.072	0.077	0.110
2	1.285 23˚, 287˚	0.964 58˚, 155˚	0.807 21˚, 026˚	1.71	0.332	-0.236	0.095	0.382
3	1.507 46˚, 301˚	0.906 15˚, 047˚	0.732 41˚, 150˚	2.79	0.525	-0.409	0.251	0.260
5	1.642 24˚, 159˚	0.917 23˚, 259˚	0.672 56˚, 028˚	2.11	0.633	-0.295	0.355	0.527

Fabric intensity, *I*, (Lisle, 1985) was calculated for both the grain shape fabric and crystal preferred orientation fabrics. Orientation tensors for the grain shape fabric are X, Y, and Z. Orientation tensors for the crystal preferred orientation fabric were determined using the Bingham statistical method incorporated in Stereoplot 3.04 (Mancktelow, 1997). The fabric intensity, *I*, parameter is a term used to describe the intensity or strength of fabrics and is an adaptation of the

previously used S_1/S_3 test, where S_1 equals the maximum eigenvalue and S_3 is the minimum (Woodcock, 1977; Woodcock and Naylor, 1983). Lisle (1985) defines *I* as:

$$I = \frac{15}{2}\sum_{i=1}^{3}\left(S_i - \frac{1}{3}\right)^2 \qquad (4)$$

where S_i are the normalized eigenvalues of the orientation tensor. Lisle argues that *I* is a less biased means of determining certain shape fabrics than S_1/S_3 because the latter results in different, frequently asymmetric distributions for girdle-type fabrics than for unimodal clusters. The validity of using *I* as a measure of fabric symmetry is discussed in Appendix VI.

5. Discussion

5.1. Temperature and Depth of Deformation

Biotite grade, greenschist facies metamorphism was associated with thrusting along the Tablerock fault (Bryant and Reed, 1970; Van Camp and Fullagar, 1982; Hatcher and Goldberg, 1991). Microstructures (Table 1) in the overlying thrust sheet are consistent with those produced in experimental studies where deformation occurred at temperatures between 350˚ and 450˚ C (Tullis and Yund, 1985). The deformation associated with folding of the Erwin formation, resulted in almost complete dynamic recrystallization of the quartzites at the study site (Fig. 18a). The ghost grains described previously, may be the remnants of primary sedimentary grains or an earlier recrystallized fabric, but because of the extent of recrystallization during the folding event it is not possible to determine the nature of the grain scale fabric prior to this recrystallization event.

Based on the results of previously published experimental studies, grain scale deformation during folding at the study site is inferred to have primarily been associated with climb-accommodated dislocation creep (Yund and Tullis, 1991). This resulted in subgrain rotation recrystallization, but as rotation of subgrain walls increased grain boundary migration recrystallization took over (Tullis and Yund, 1985; Lloyd and Freeman, 1994). This is evidenced by the dominance of grain boundary migration structures such as sutured grain boundaries (Fig. 18b), and the less frequent presence of subgrains (Fig. 18c & d) throughout all the samples. During recovery the sutured and undulose quartz grain boundaries underwent grain boundary area reduction, reducing the internal free energy of the quartz grain, which produced the more stable, euhedral grain boundaries (Fig. 18f) exhibited by many of the quartz grains (Bons and Urai, 1992).

Although, feldspar grains exhibit perthitic twins (Fig. 18e), alteration rims of white mica and fine grained quartz, or are moderately fractured, none of the feldspar grains displayed any

evidence of subgrain rotation or grain boundary migration. Metamorphic reactions common during low grade metamorphism include the alteration reaction,

$$\text{Potassium Feldspar} + H_20 = \text{Muscovite (white mica)} + \text{Quartz} \quad (5)$$

when water is readily available. If the activity of water is low, potassium feldspar survives in a metastable state (Hibbard, 1995). These relationships may explain why potassium feldspar grains present within the sample suite exhibit little to no alteration. The internal twinning, low temperature alteration to white mica and quartz, and minor fracturing observed in the sample suite, are consistent with experimental deformation studies of feldspars at low to medium grade conditions (300˚-500˚C).

Microstructures exhibited by quartz grains in the sample suite include undulose extinction, subgrains, and sutured grain boundaries. Quartz grains deformed under low to medium grade conditions (~400˚C) frequently exhibit undulose extinction (Passchier and Trouw, 1996). Experimental evidence indicates that with increasing temperature (from 400˚C+), recrystallization mechanisms change from predominantly subgrain rotation to subgrain rotation plus grain boundary migration processes (Hirth and Tullis, 1992). The microstructures exhibited by both quartz and feldspar grains from each sample suite are consistent with microstructures reported in experimental studies deformed at temperatures around 400˚C, and are in agreement with previous studies that document biotite grade, greenschist facies metamorphism during deformation of the Tablerock Thrust sheet (Hatcher and Goldberg, 1991). Biotite grade, greenschist facies metamorphism ranges between 400˚-500˚C, at depths between 15 to 22 kilometers assuming a geothermal gradient between 25˚-30˚C per kilometer depth (Turner, 1968; Hibbard 1995).

5.2. Development of the Clinchfield Railroad Fold

Based on interpretations by Bryant and Reed (1970), folds within the Tablerock thrust sheet, including the Clinchfield Railroad fold, developed in response to motion along the underlying Tablerock thrust during Alleghanian deformation. In general, folding results from either active or passive deformation. Active folding occurs when a mechanical instability within a stratified sequence of rocks leads to buckling in response to stresses acting on the system (Biot, 1961; Ramberg, 1961) and occurs in layers of uniform rheology (Merle, 1998). Passive folding occurs when layers slip, shear or flow across one another in response to deformation. The layers take no active part in the deformation (Ramsay, 1967, p. 430). Passive folding produces similar folds in which dip isogons are parallel throughout the fold and the hinge zone is thickened with respect to the limbs (Ramsay, 1967 p. 367). The geometry of the Clinchfield Railroad fold is not consistent with that produced by passive folding mechanisms, but is consistent with Class 1B

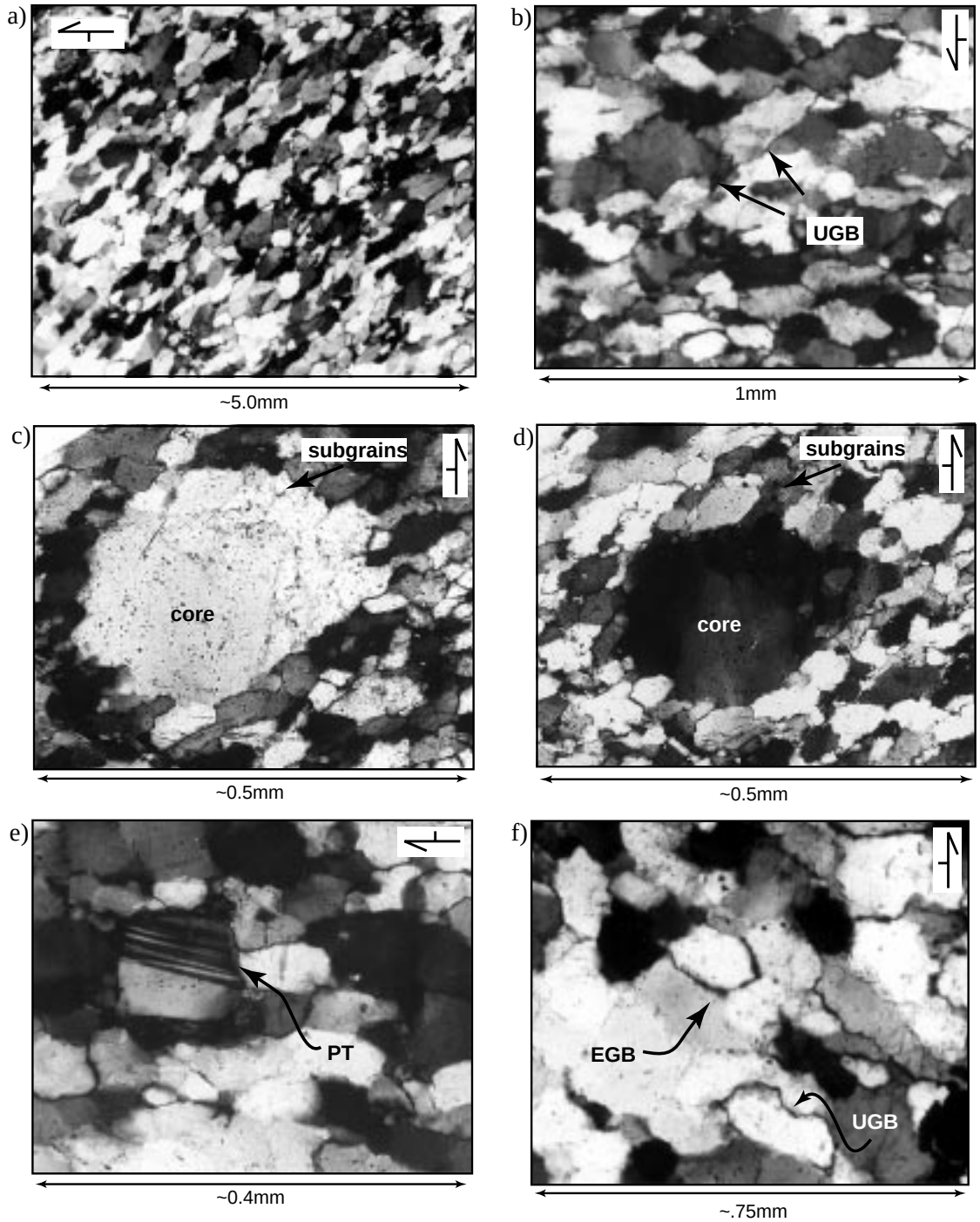

Fig. 18. Representative photomicrographs taken under cross polarized light. Field of view is indicated for each figure, orientation markers are referenced with respect to the thin section of origin. a) Example of the recrystallized texture and grain shape fabric exhibited in each sample, b) Undulose or sutured grain boundaries (UGB) evident throughout all the samples c) & d) Photomicrographs of the same field of view at different angles of extinction. Notice the core or ghost grain which is larger than the surrounding recrystallized quartz grains, and the subgrains along the upper boarder, e) Feldspar grain with perthitic twinning, f) Linear grain boundaries (LGB) evident along some quartz grains.

parallel folds that form from active folding (Ramsay, 1967 p. 367). Class 1B parallel folds form in competent units, maintaining constant orthogonal thickness throughout individual layers, and have dip isogons that are perpendicular to layering.

Simple models for active folding during deformation predict that the fold axis will form parallel to the **XY** plane of regional deformation. Therefore, in thrust systems the fold hinge plane should strike parallel that of the orogen, and perpendicular to the regional transport direction. The trend of the Clinchfield Railroad fold axis, however, is almost parallel to the regional **XZ** plane of deformation. This relationship indicates that processes in addition to those associated with active folding were also operative during deformation of the Tablerock thrust sheet. The kinematics of active folding and the orientation of the Clinchfield Railroad fold axis are discussed below.

5.2.1. Active Thrust Related Folding and the Clinchfield Railroad Fold

Given the final geometry of the Clinchfield Railroad fold and its association with the Tablerock fault, folding at the study site was produced by one of the following:, i) Mode II fault-bend folding, ii) fault-propagation folding, or iii) detachment folding (Fig. 19). Fault-bend folds are similar to passive folds. Layers deform in response to changes in the orientation of the ramps and flats of the underlying fault (see review by Merle, 1998). Fault-propagation folds and detachment folds are both associated with the termination of an underlying thrust fault along either a ramp or a flat. Where the displacement along a fault reaches zero, internal deformation to the foreland of the fault tip line is expressed in the form of horizontal shortening that results in folding when mechanical contrasts exist, such as between layers possessing different rheological properties (Merle, 1998).

Geometrically, Mode II fault-bend folds can resemble fault-propagation folds or detachment folds. Generally, the upright limb-upper flat in Mode II fault-bend folds maintains a gentle to shallow dip (Jamison, 1987). The angle of dip along the upright limb of the Clinchfield Railroad fold is ~30˚ and is steeper than those usually modeled for Mode II fault-bend folds. The geometry of the Clinchfield Railroad fold is more consistent with those produced during fault-propagation folding or detachment folding. Characteristics shared by these modes of deformation include a steeply dipping to overturned fore limb and an interlimb angle that is close to tight.

Faults that produce fault-bend folds and fault-propagation folds are primarily documented in association with brittle deformation events. The formation of detachment folds, however, is documented in association with both brittle and ductile faulting. There is no outcrop expression of faulting at the study site. Mylonites identified elsewhere in the thrust sheet adjacent to the Tablerock fault (Trupe, 1999), and the deformation temperature of ~400˚ C (biotite grade greenschist facies metamorphism), indicate that deformation within the thrust sheet was primarily

accommodated by crystal plastic processes during thrusting. These observations suggest that detachment folding was responsible for the development of the Clinchfield Railroad fold.

During active folding, Class 1B parallel folds usually form as a result of flexural slip and/or tangential longitudinal strain (Ramsay, 1967 p. 392). During buckling in flexural slip folding, individual rock layers are flexed and the outermost layers slip over the inner layers, moving towards the fold hinges (Fig. 20a). Evidence for flexural slip during folding includes the presence of slickenfibers along bedding planes and layers of equal thickness through the limb and hinge zones of the fold, indicating inter-bed slip accommodated deformation. Tangential longitudinal strain, which involves deformation within rock layers, commonly occurs in areas where there is little to no preexisting planar anisotropy, or in competent rock units such as quartzites (Ramsay, 1967 p. 397). During deformation the principal axes of strain are oriented tangential and perpendicular to the layers in the fold (Fig. 20b) (Ramsay, 1967). Layers located towards the outer arc of the fold experience layer-parallel extensional deformation, with the maximum extensional stresses developing in the hinge of the fold. Layers towards the inner arc of the fold experience compressional deformation, the maximum compressional stresses developing in the hinge of the fold. A neutral surface of no infinitesimal deformation separates these two zones (Fig. 20b). Depending on the scale of the fold all three deformation regimes, i) compressional, ii) neutral, and iii) extensional may not be recorded in one fold (Treagus and Treagus, 1981)

The grain shape fabric recorded throughout the Clinchfield Railroad fold is consistent with internal deformation developed by tangential longitudinal strain. The sample bed is located towards the inner arc of the antiform. The magnitudes and orientations of the principal grain shape ellipsoid axes in samples **1**, **2**, **3**, and **5** are given in Figure 21. The grain shape ellipsoid shapes all plot within the constrictional strain field on both Flinn and Nadai plots (Fig. 17). These samples are distributed across the inner limbs and hinge zone of the fold. Sample **4**, which lies farthest away from the hinge along the upright limb, plots along the line of plane strain on both Flinn and Nadai plots. This general trend is consistent with models of deformation by tangential longitudinal strain produced by Ramsay (1967 p. 398) (Fig. 20b). Along one foliation plane, poorly developed slickenfibers, were observed trending roughly perpendicular to strike within the fold. The thickness of individual layers throughout the fold remain constant, traced from limb to limb. This indicates that flexural slip deformation may have also been active during buckling. The internal accommodation of deformation by both layer parallel slip and tangential longitudinal strain is common during folding (Ramsay, 1967).

5.2.2. Magnitudes and Symmetry of Grain Shape Fabric Ellipsoids

The magnitude and symmetry of strain or grain shape fabric ellipsoids in folds forming from pure buckling or bending processes is generally symmetrically distributed about the hinge-

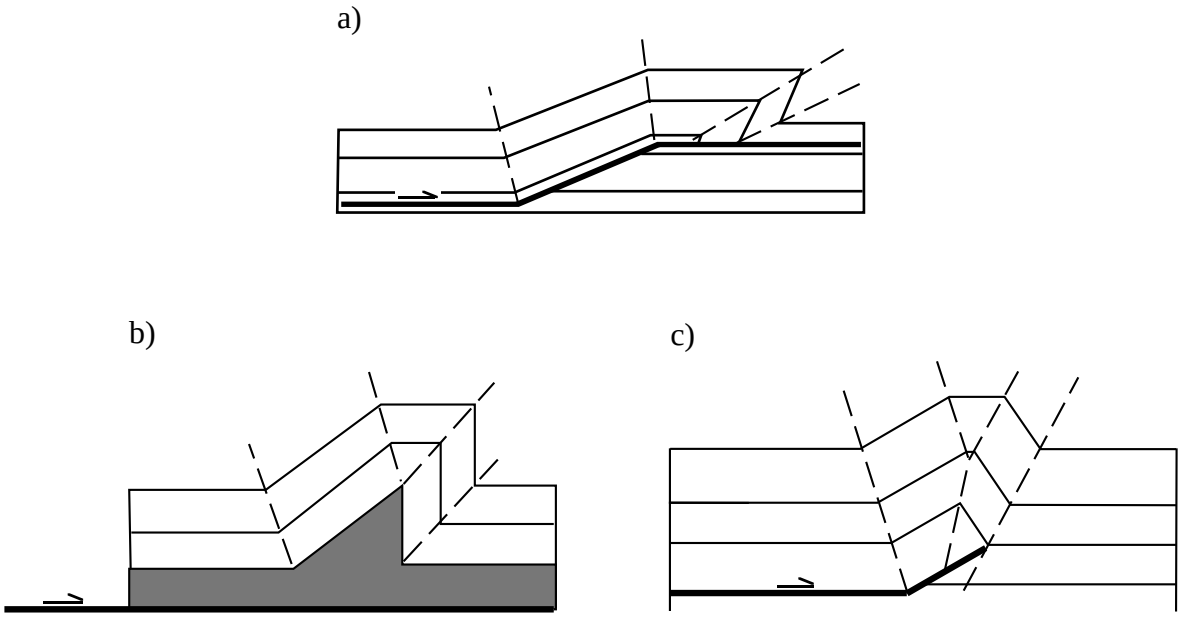

Fig. 19. a) Schematic model of a mode II fault-bend fold (after Jamison, 1987), b) schematic fault-propagation fold model (after Suppe and Medwedeff, 1990), c) schematic detachment fold model (after Jamison, 1987).

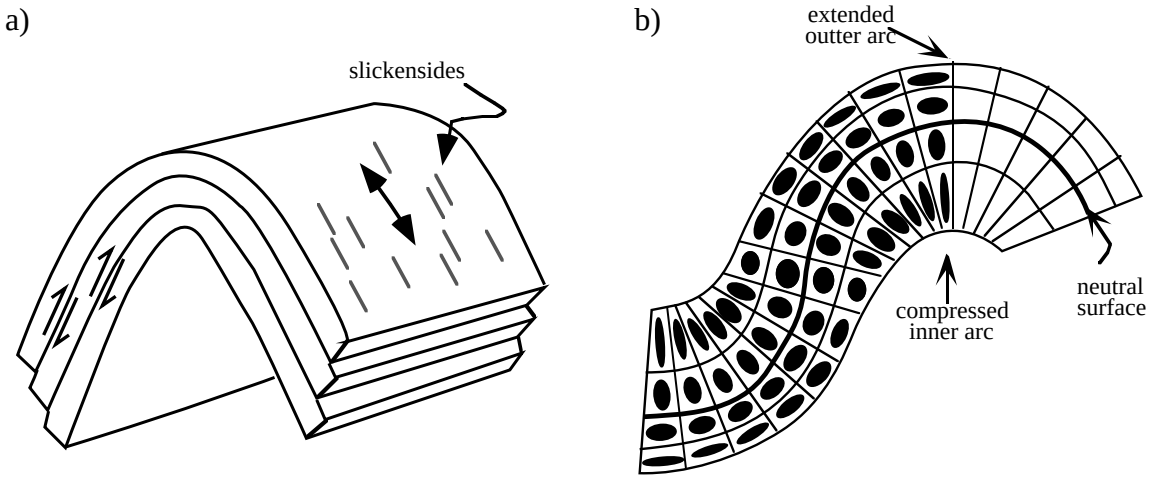

Fig. 20. a) Folding by flexural-slip (after Ramsay, 1967) and, b) folding involving tangential longitudinal strain. Outlines of 2-D strain ellipses modeled for each position throughout the fold (after Ramsay, 1967).

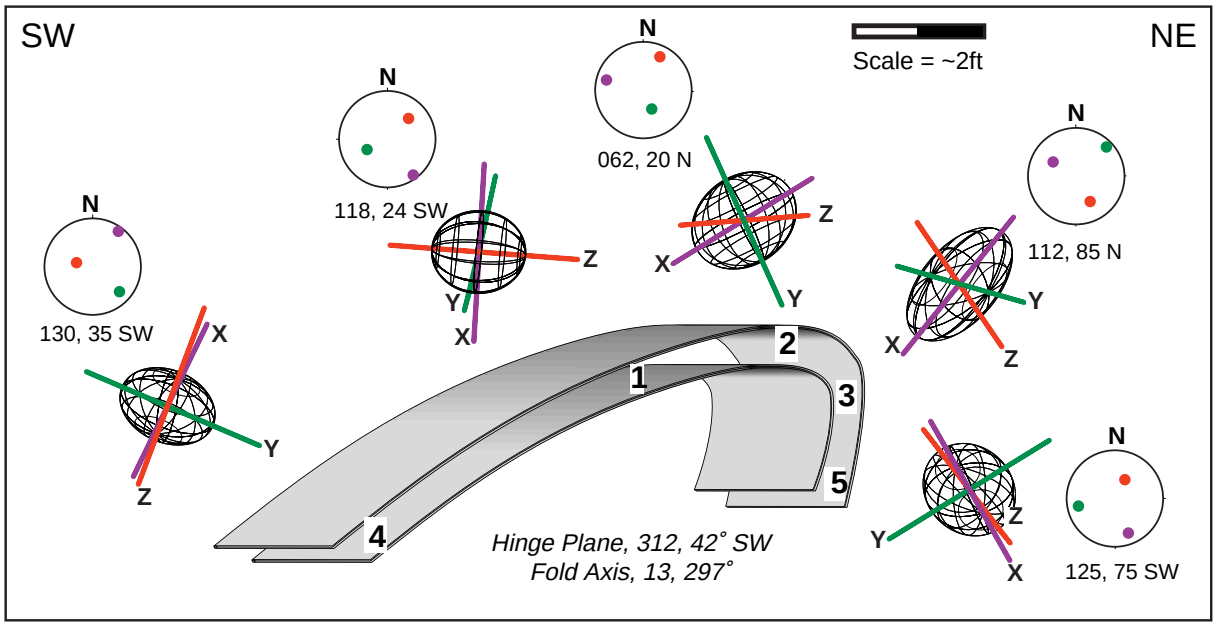

4	1	2	3	5
X = 1.245 at 10˚, 038˚	X = 1.261 at 09˚, 143˚	X = 1.285 at 23˚, 287˚	X = 1.507 at 46˚, 301˚	X = 1.642 at 24˚, 159˚
Y = 1.004 at 24˚, 132˚	Y = 1.002 at 51˚, 244˚	Y = 0.964 at 58˚, 155˚	Y = 0.906 at 15˚, 047˚	Y = 0.917 at 23˚, 259˚
Z = 0.800 at 64˚, 287˚	Z = 0.821 at 38˚, 047˚	Z = 0.800 at 21˚, 026˚	Z = 0.732 at 41˚, 150˚	Z = 0.672 at 56˚, 028˚

Fig. 21. Wireframe representations of grain shape ellipsoids, calculated from 2-D sectional ellipse data using Rϕ/f analysis and Macstrain 2.4, for each sample along the Clinchfield Railroad fold. Equal area stereoplots illustrate the plunge and trend of the primary ellipsoid axes. The magnitude, plunge and trend of each axis is listed in the table below. Strike and dip of bedding/foliation at each sample location is noted below each stereoplot.

plane of the fold (Fig. 22) (Ramsay, 1967; Twiss and Moores, 1992). During deformation produced solely by bending or buckling processes, the orientation, magnitude and symmetry of grain shape ellipsoids on one limb should be equal to those found at the same position on the opposite limb. The hinge plane in the Clinchfield Railroad fold is located between samples **2** and **3** in the sample bed (Fig. 23). If folding resulted purely from bending or buckling processes, the orientations, magnitudes and symmetry of the calculated grain shape fabric ellipsoids across the fold should be symmetrically distributed.

Along the upright limb, approaching the hinge of the fold, are samples **4**, **1**, and **2** respectively. The Flinn and Nadai plots illustrate that both the magnitude and symmetry of the grain shape fabric ellipsoids on the upright limb progressively increase and change from plane strain deformation (sample **4**) to increasing constrictional deformation (samples **1** and **2** respectively). The magnitude of constrictional strain recorded by the grain shape fabric ellipsoids continues to increase through the fold hinge and sample **3**. The maximum strain magnitude ($\bar{\varepsilon}_s$)

value calculated for the grain shape fabric ellipsoids is at sample **5**, on the overturned limb of the fold (Fig. 23). The highest strain symmetry value (v and k) was calculated for sample **3**, in the overturned limb just past the fold hinge (Fig. 23).

In pure buckling models where internal deformation is partially or entirely accommodated by tangential longitudinal strain along the inner layers of the fold, the highest strain magnitude is recorded in the hinge of the fold. The asymmetrical distribution of the grain shape ellipsoid magnitudes in the Clinchfield Railroad fold indicates that processes other than pure bending and/or buckling were operative during deformation. Passive shear folding models predict the lowest strains will occur in the hinge of the fold. These models also predict thickening in the hinge zone of the fold and thinning along the limbs. The Clinchfield Railroad fold displays neither of these characteristics. There is no change in thickness along layers in the fold, and the minimum "strains" calculated along the sample bed occur farthest away from the hinge of the fold in the upright limb.

The simplified models reviewed above do not explain the obliquity of the Clinchfield Railroad fold axis to the regional **XY** plane of deformation or the asymmetric distribution of grain shape magnitudes across the fold profile. This indicates that processes in addition to layer parallel flexural-flow and tangential longitudinal strain associated with the formation of folds in the Tablerock thrust sheet were active during deformation.

5.2.3. Obliquity of Fold Axes - Rotation of Folds During Progressive Deformation

Throughout the Tablerock thrust sheet there are mesoscale folds with axes that are oriented oblique to the regional **XY** plane of regional deformation and the trend of megascopic folds in the southern Appalachians (Bryant and Reed, 1970). Bryant and Reed (1969) suggested a conceptual model to explain these occurrences in which the obliquity of fold axes to the regional transport direction formed from the modification of earlier open folds with axes parallel to the **Y** regional axis. During continued deformation these folds were: i) progressively tightened, ii) flattened, and iii) passively rotated away from the **Y**-axis of regional deformation towards the **X**-axis of regional deformation. More recent conceptual, numeric and natural studies have provided further explanations for folds with axial orientations oblique to the regional trend (see review by Merle, 1998).

Many thrust belts display an arcuate shape in plan view, where the maximum displacement along the fault is found at the center of the thrust and diminishes towards either lateral boundary. Based on analysis of this commonly displayed thrust geometry, Elliot (1976) suggested the bow and arrow rule for thrusting. On a map the position of these overthrusts is arcuate and the lateral boundaries of the fault are oriented sub-parallel to the primary transport direction of the thrust. The bow and arrow theory assumes that maximum displacement occurs at the center of the fault and within the lateral borders of the thrust sheet transcurrent shear occurs (Fig. 24a). Coward and

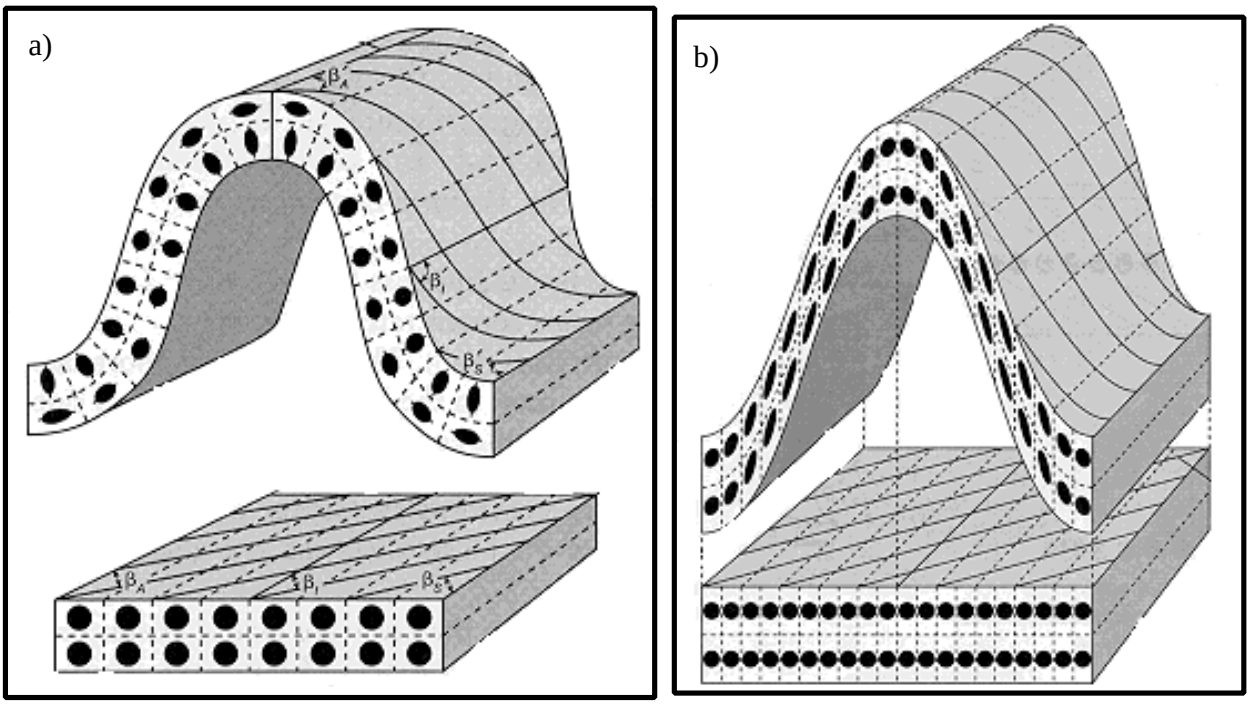

Fig. 22. Two examples of fold models, a) generalized flexural folding and b) generalized passive shear folding, with associated 2-D strain ellipses (Twiss and Moores, 1992 p. 317-318). Note the mirror symmetry of strain ellipses across the fold hinge plane. Flexural folding model displays internal characteristics of tangential longitudinal strain signatures where the maximum extensional and compressional strains are found within the hinge zone of the fold. Passive shear folding predicts extensional strains in the limbs of the fold and thickening in the hinge zone of the fold.

Potts (1983) developed Elliot's bow and arrow model further, based on theoretical and natural observations. They compared the tip line of the fault, oriented perpendicular to the transport direction, to edge dislocations and the lateral portions of the fault to screw dislocations. Within the frontal portions of faults they suggested that deformation is primarily associated with compressive strains and layer-parallel shortening. The development of layer parallel shortening may cause rocks to fold, frequently producing asymmetric folds (Coward and Potts, 1983). Along the lateral boundaries of the fault, shear strains would develop normal to the main thrust plane but parallel to the overall transport direction (Fig. 24a, b). Folds would also develop in the lateral regions of the thrust, initiating with their axes perpendicular to the regional transport direction. As the ratio of layer parallel shear (γ_1 – shear strain in the direction of regional transport) to differential shear (γ_2 – wrench-shear strain along the lateral regions of the thrust system) decreases within the lateral portions of these arcuate thrust sheets, fold hinges are rotated and verge away from the direction of layer parallel shear (Coward and Potts, 1983) (Fig. 24a, b & c). Although the fold axes are reoriented towards the direction of transport, the hinge plane does not fold or deform but maintains a constant geometry throughout rotation (Coward and Potts, 1983; Merle, 1998). The folds are

reoriented by means of strike-rotation hinge plane migration as predicted by Treagus and Treagus (1981), Coward and Potts (1983), and Ghosh et al.s' (1996) studies. Although the Treagus and Treagus (1981) and Ghosh et al. (1996) models addresses the problem of strike-rotation hinge migration during deformation, their results predicting obliquely oriented fold axes in folds experiencing constrictional deformation are consistent with the results of Coward and Potts (1983) study and Elliot's (1976) bow and arrow model.

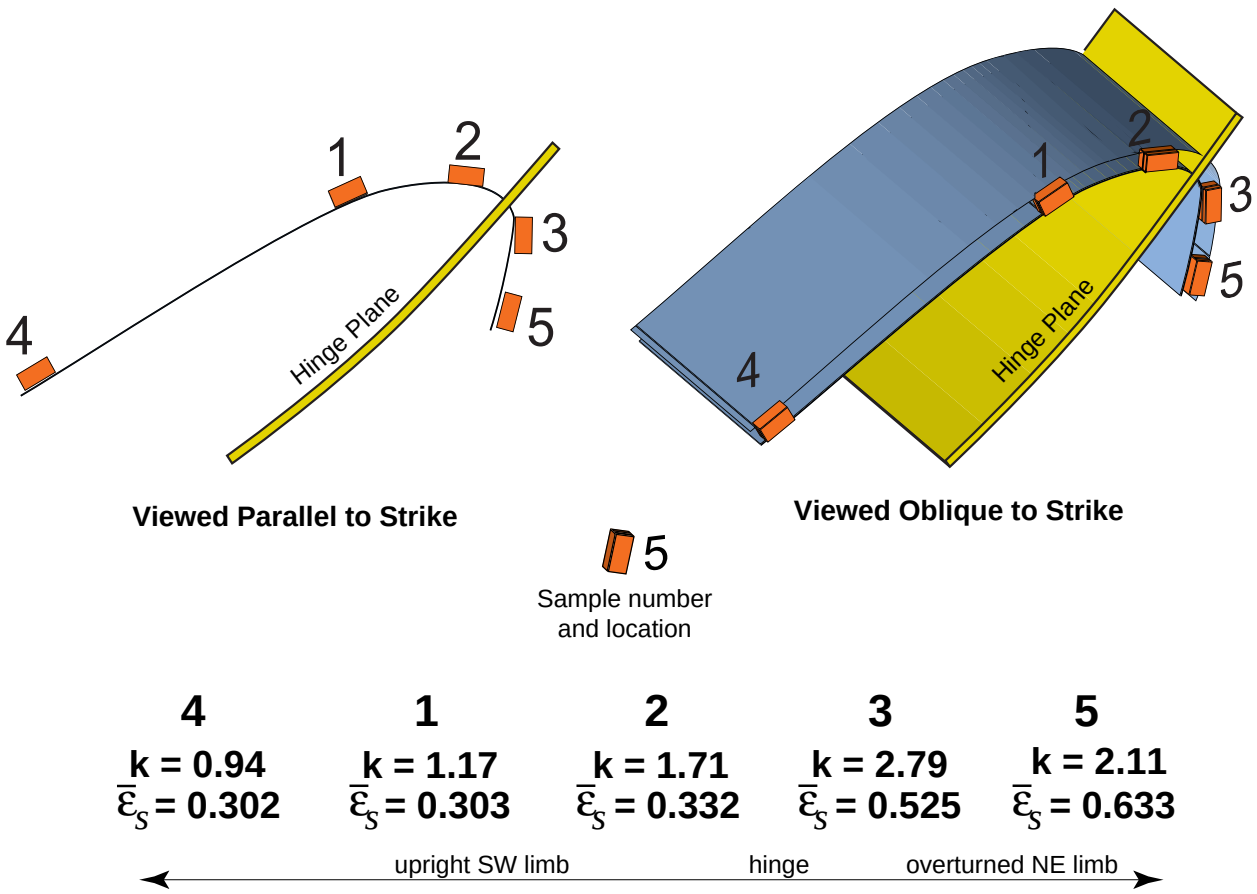

Fig. 23. To scale line drawing of sample bed, sample locations, and orientations of hinge and hinge plane in the Clinchfield Railroad fold. k-values and $\bar{\varepsilon}_s$ values calculated for each sample location are also given. Note that the magnitude of strain ($\bar{\varepsilon}_s$) and strain symmetry (k) are greatest in the overturned limb of the fold.

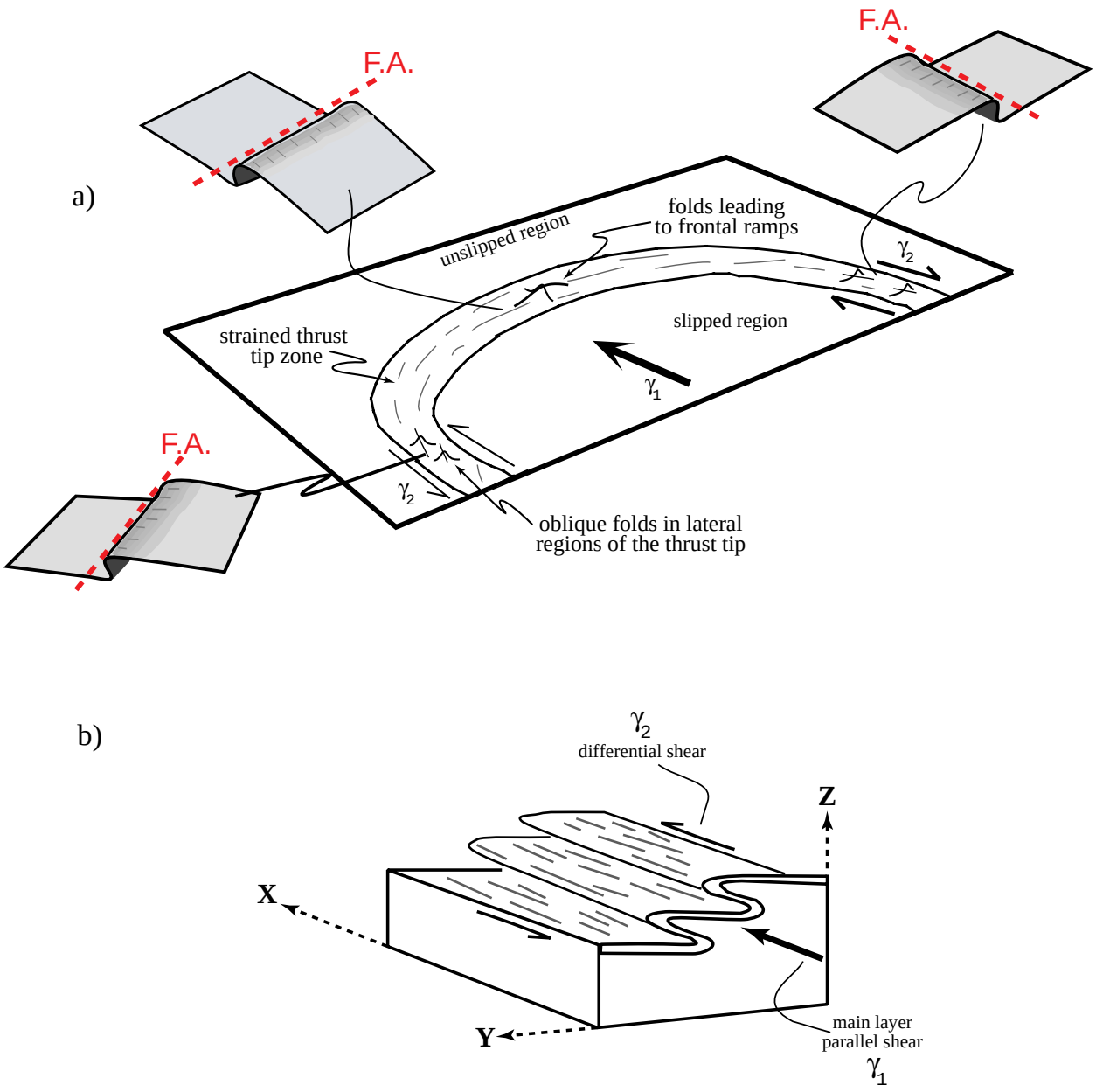

Fig. 24. Thrust plane with strained tip between the slipped and unslipped regions (adapted from Coward and Potts, 1983). a) Schematic drawing of the strained tip region in a thrust plane bounding the slipped (hangingwall) and unslipped (footwall) regions of the system. Notice the orientation of folds in the frontal ramp region compared to the orientation of folds in the lateral regions of the thrust tip. Folds in the lateral regions are oriented oblique to the regional strike of the thrust system as a result of differential shears (γ_2) associated with the lateral regions of the thrust system. b) Block diagram showing fold hinges rotated parallel to the direction of main layer shear (γ_1), which are predicted to form in the lateral tip region of thrust systems as a result of competing differential (γ_2) and layer parallel (γ_1) shears.

5.3. Hinge Migration and the Clinchfield Railroad Fold

In the southern Appalachians, most major fold hinge planes and faults strike northeast-southwest (approximately parallel to the strike of the **XY** plane of regional deformation), as a result of thrusting towards the northwest during the Paleozoic. The hinge plane of the Clinchfield Railroad fold is oriented at 312˚, 42˚ SW and the fold axis plunges at 13˚ to 297˚. The orientation of the fold axis and fold hinge plane in the Clinchfield Railroad fold are highly oblique to the regional **XY** plane of deformation. The fold is asymmetric, verging to the northeast (Fig. 9). Detailed mapping and structural analysis demonstrates that many of the mesoscale folds are oriented obliquely to the regional **XY** plane of deformation within the Tablerock thrust sheet (Bryant and Reed, 1970, plate IV). In contrast, a detailed lineation map of the Grandfather Mountain Window region indicates that mineral stretching lineations from more pelitic units, trend northwest to southeast and are gently plunging throughout the Tablerock thrust sheet (Bryant and Reed, 1970, Fig. 33). These lineations are consistent with northwest directed thrusting and the **XZ** regional plane of deformation.

5.3.1. Strike-Rotation Hinge Migration and the Obliquity of the Clinchfield Railroad Fold Axis

The conclusions of the Treagus and Treagus (1981), Coward and Potts (1983), and Ghosh et al.s' (1996) studies, regarding the oblique orientation of folds in thrust belts, are consistent with the results of this study when the Tablerock thrust sheet is used as the reference frame for examining the Clinchfield Railroad fold. Treagus and Treagus (1981) and Ghosh et al.'s (1996) studies predict higher activity of strike-rotation hinge migration during folding associated with constrictional deformation. Treagus and Treagus (1981) also reported that folding aided by strike-rotation hinge migration processes during constrictional deformation may produced non-cylindrical folds with curving (decreasing dip) axial planes, which is consistent with the geometries of the hinge plane and profile of the Clinchfield Railroad fold (Fig. 9).

Elliot (1976) and Coward and Potts (1983) studies illustrating the deformation associated with arcuate thrusting are also consistent with the results of this study and those presented by Treagus and Treagus (1981) and Ghosh et al. (1996). Coward and Potts (1983) model for oblique fold development in the lateral portions of arcuate thrust sheets is consistent with the structures observed by Bryant and Reed (1969, 1970) and Treagus and Treagus (1981). With increasing magnitudes of main layer parallel shear (γ_1) and differential shear (γ_2) folds in the lateral portions of thrust sheets undergo reorientation by means of strike-rotation hinge plane migration. According to the Coward and Potts (1983) model, the hinge planes of these reoriented folds do not deform internally during rotation, maintaining an internally consistent strike at all structural levels throughout reorientation. The subsequent obliquely oriented folds, such as the Clinchfield Railroad fold, may therefore, have experienced hinge plane migration by strike-rotation as

described by the models of Treagus and Treagus (1981), Coward and Potts (1983) and Ghosh et al. (1996).

Building on the conclusions of the strike-rotation models described above, it is interesting to note that the *X*-axis of the grain shape ellipsoids for each sample, except Sample **4**, trends roughly parallel to the orientation of the Clinchfield Railroad's fold axis (Fig. 25). Generally, however, the regional deformation axis that trends approximately parallel to the orientation of the fold axes in a fold and thrust belt, is the **Y**-axis of deformation. In a simple fold and thrust system the axes of regional deformation (**X**, **Y**, and **Z**) would be expected to align with the axes of the grain shape fabric ellipsoids (*X*, *Y*, and *Z*). However, the strike-slip or wrench component of deformation associated with the bow and arrow model for thrusting, results in the activation of additional stress regimes besides those associated with pure contractional deformation. The axis of maximum elongation (*X* and **X**) in a strike slip system would roughly parallel the orientation of the differential shear stress (γ_2) acting upon the system. The strike-rotation of mesoscale folds in the lateral portions of the thrust tip in arcuate thrust sheets, is activated by an increase in the differential shear stresses (γ_2) acting upon those regions (Coward and Potts, 1983). If the differential shear stresses (γ_2) in the lateral regions of a thrust system are strong enough to induce strike-rotation hinge plane migration of mesoscale folds in these regions, it may be inferred that the local orientation of maximum elongation (*X*) within these zones would also be affected. Given this relationship, the direction of maximum escape or elongation (*X*) in these lateral portions of the thrust tip region would progressively become oriented sub-parallel to the trend of the rotated fold axis. As the angle of strike-rotation HPM increases, the more closely aligned the fold axis and the *X*-axis of the grain shape fabric would become.

5.3.2. Material Migration Hinge Migration and the Clinchfield Railroad Fold

The distribution of strain magnitudes ($\bar{\varepsilon}_S$) across the Clinchfield Railroad fold is asymmetric, suggesting that processes in addition to buckling were active during folding. The location of the high magnitude grain shape fabric ellipsoids along the overturned limb, and the northwesterly vergence of the fold indicate that material translation migration was also active and dominant during deformation (Fig. 23). Based on Ramsay's (1967) model of internal deformation by tangential longitudinal strain, the highest magnitude compressional stresses will form in the hinge of a fold's inner layers. If hinge migration processes are active during deformation, the material affected by these high magnitude strains can be translated into the limb of the fold. As a result of material translation, positions **3** and **5** once defined the hinge of the Clinchfield Railroad fold, and high magnitude grain shape fabrics were recorded at these positions reflecting those conditions produced when the material was located in the hinge zone of the fold. Dip-rotation and lateral translation migration processes may have contributed to folding during deformation, but the

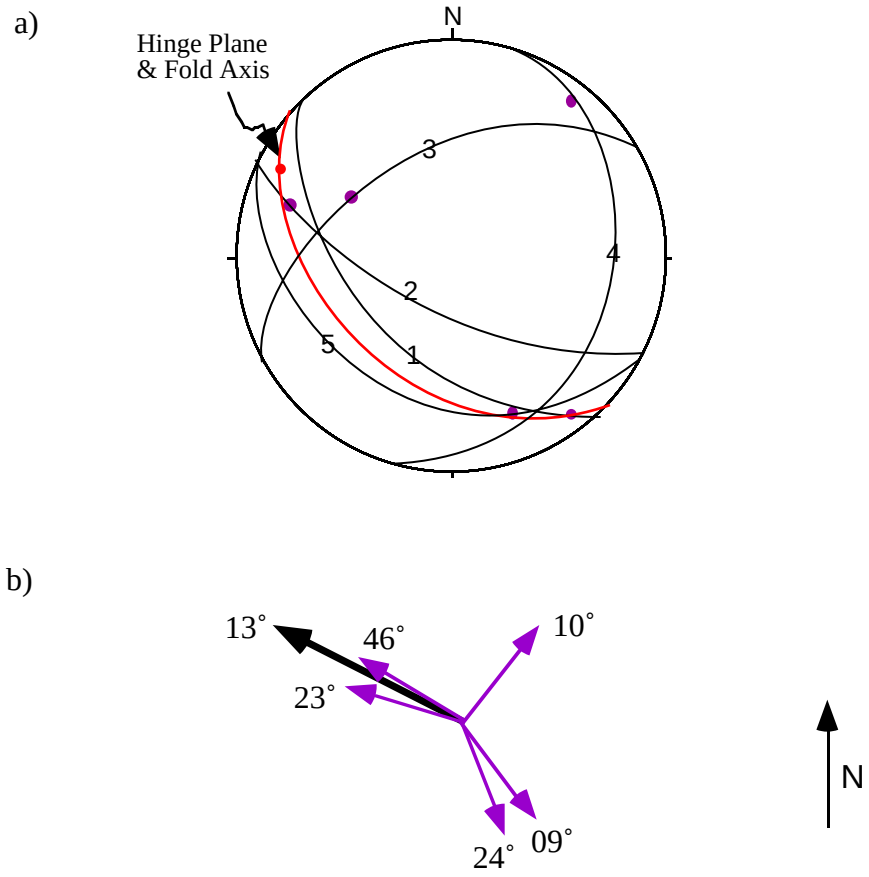

Fig. 25. a) Equal area stereoplot of the Clinchfield Railroad fold's hinge plane, fold axis, and the plunge and trend of the*X*-axis of the grain shape fabric from each sample. b) Arrows, depicting the trend of the fold axis and *X*-axes of the grain shape fabric ellipsoids, illustrating that the general trend of the fold axis is approximately parallel to the trend of the *X*-axis of the grain shape fabric in the Clinchfield Railroad fold (major exception is sample **4**). Black great circles equal the *XY* grain shape fabric plane.

kinematics of these deformation processes with respect to the defined reference frame, does not explain the location of the high magnitude grain shape fabric ellipsoids in the overturned limb.

In the case of the Clinchfield Railroad fold, recrystallization processes must have been operating at a slower rate than the grain shape fabric and hinge migration processes in order to preserve the anomalously high strains at positions **3** and **5** (Fig. 21). However, the slight decrease in strain symmetry (*k*) at position **5** (Fig. 17b) does suggest that the internal deformation processes in the limb, (associated with smaller constrictional strains and symmetries normally associated with the limb regions of the fold) had begun to modify the high constrictional strain hinge zone signature that was imposed on the rock when position 5 was in the hinge.

5.4. Crystal Preferred Orientation Measurements, Record of Initial Layer-Parallel Shortening?

Most samples within the Clinchfield Railroad fold record a prolate grain shape fabric (*X*, *Y*, and *Z*) signature (Fig. 17). Neither set of crystal preferred orientation plots (CPO) (Figs. 10a&b - 14a&b) produced for each sample, exhibit patterns consistent with experimentally produced CPO patterns formed during constrictional deformation (Lister and Hobbs, 1980). The first series of CPO plots (Figs. 10a-14a) are viewed with respect to the plane of foliation for each sample, where foliation plots along the primitive circle of each plot. The location of the grain shape fabric axes are shown on each plot, as is the projection of the fold axis onto the primitive of each plot. The second set of CPO plots (Figs. 10b-14b) are viewed with respect to the grain shape fabric axes (*X*, *Y*, and *Z*), a variation of the traditional frame of reference for interpreting CPO plots. The distribution of the grain shape fabric symmetries (*k*) across the fold, and the orientation of the *X* -axis with respect to the regional axes of deformation, indicate that development of the grain shape fabric was a continuous process throughout deformation. Also, because a mesoscopic lineation is not present, and foliation does not correspond to the *XZ* grain shape fabric plane, the semi-traditional frame of reference used for the second series of CPO plots is not appropriate for interpreting the samples from the Clinchfield Railroad fold. The first series of CPO plots were used for interpretation purposes.

The CPO patterns, especially those exhibited in samples **4**, **2**, and **3**, are consistent with Type I cross girdle patterns produced during low temperature, non-coaxial, plane strain deformation (Law, 1990). If the rate of CPO fabric development was slower than the rate of grain shape fabric development then the two fabrics would record different parts of the deformation history for the Clinchfield Railroad fold. The development of CPO fabric patterns is influenced by the realignment of the c-axis of the quartz crystal during deformation in response to changes in temperature, strain rate, and recrystallization processes (Lister et al., 1978; Lister and Hobbs, 1980; Law, 1990 and references therein).

At the onset of contractional deformation associated with displacement along the Tablerock thrust sheet, the effects of layer parallel shortening would have been recorded by the rocks of the Clinchfield Railroad fold. Initial coaxial shortening, prior to noncoaxial deformation associated with the development of the thrust system, would result in the development of a symmetric, Type I cross girdle fabric (Fig. 26b), the remnants of which are seen in samples from the study site (Fig. 12a-16a).

Given the Coward and Potts (1983) model for arcuate thrusting, the Clinchfield Railroad fold hinge would form parallel to the strike of the fold and thrust belt, roughly parallel to the inferred regional **Y**-axis. The CPO patterns (especially for samples **2**, **3**, and **4**) indicate that the hinge is oriented parallel to the maximum extension direction (Figs. 10a – 14a and 26). With continued folding and thrusting the effects of the noncoaxial, differential stresses (γ_2), in the lateral

regions of the thrust system, would increase eventually activating strike-rotation HPM of the Clinchfield Railroad fold. This strike-rotation HPM would result in modification of the coaxial, symmetrical, Type I cross girdle patterns formed during initial layer parallel shortening, to produce the asymmetric, noncoaxial, Type I cross girdle patterns exhibited by the samples from the Clinchfield Railroad fold (Fig. 26c). A faster rate of recrystallization of the grain shape fabric, relative to the rate of development of the CPO fabric, may explain why the two fabric patterns are different. Each records the deformation history at different stages in development of the Clinchfield Railroad fold.

5.5. Kinematic Model for the Development of the Clinchfield Railroad Fold

Given the relationships discussed above, the following model for the development of the Clinchfield Railroad fold and the Tablerock thrust sheet is proposed. Rocks within the Tablerock thrust sheet experience layer parallel shortening associated with thrusting along the underlying fault during biotite grade greenschist facies metamorphism(Fig. 26a & b). As transport along the Tablerock thrust sheet continued, lateral propagation of the tip line produced an increasingly arcuate thrust geometry, similar to the model proposed by Elliot (1976) and Coward and Potts (1983). Initially, the Clinchfield Railroad fold probably formed in an orientation consistent with the regional trend, with a fold axis that trends roughly northeast-southwest parallel to the strike of the frontal thrust tip (Fig. 26c). As transport along the fault continued, differential shear stresses in the lateral regions of the thrust tip increased, ultimately resulting in the passive dextral strike-rotation of the Clinchfield Railroad fold and other mesoscale folds within the Tablerock thrust (Figs. 26 & 27). Evidence for strike-rotation hinge plane migration includes: i) the oblique orientation of the Clinchfield Railroad's fold axis with respect to the regional strike of the fold-thrust belt (Fig. 26a), ii) the asymmetric, Type I cross girdle CPO patterns, iii) the orientation of the *X*-axis of the grain shape ellipsoid fabric with respect to the regional trend, and iv) the northeast vergence of the Clinchfield Railroad fold and the Coward and Potts (1983) model for arcuate thrusting, that suggest the Clinchfield Railroad fold crops out in the dextral-lateral region of the Table Rock thrust system (Fig. 27).

The development of the fold, throughout deformation was accommodated by flexural folding, material translation HPM, and strike-rotation HPM processes, as evidenced by the orientation, magnitude, symmetry and position of the grain shape fabric ellipsoids throughout the Clinchfield Railroad fold. The asymmetric CPO patterns from the study site provide evidence for noncoaxial deformation during thrusting, however, the multiple mechanisms of deformation associated with the development of the fold, make determining the sense of shear difficult. When the asymmetry of the CPO patterns are interpreted with respect to the fold axis (Figs. 10a – 14a & 26), the shear sense may be interpreted as being consistent with modified dextrally deformed

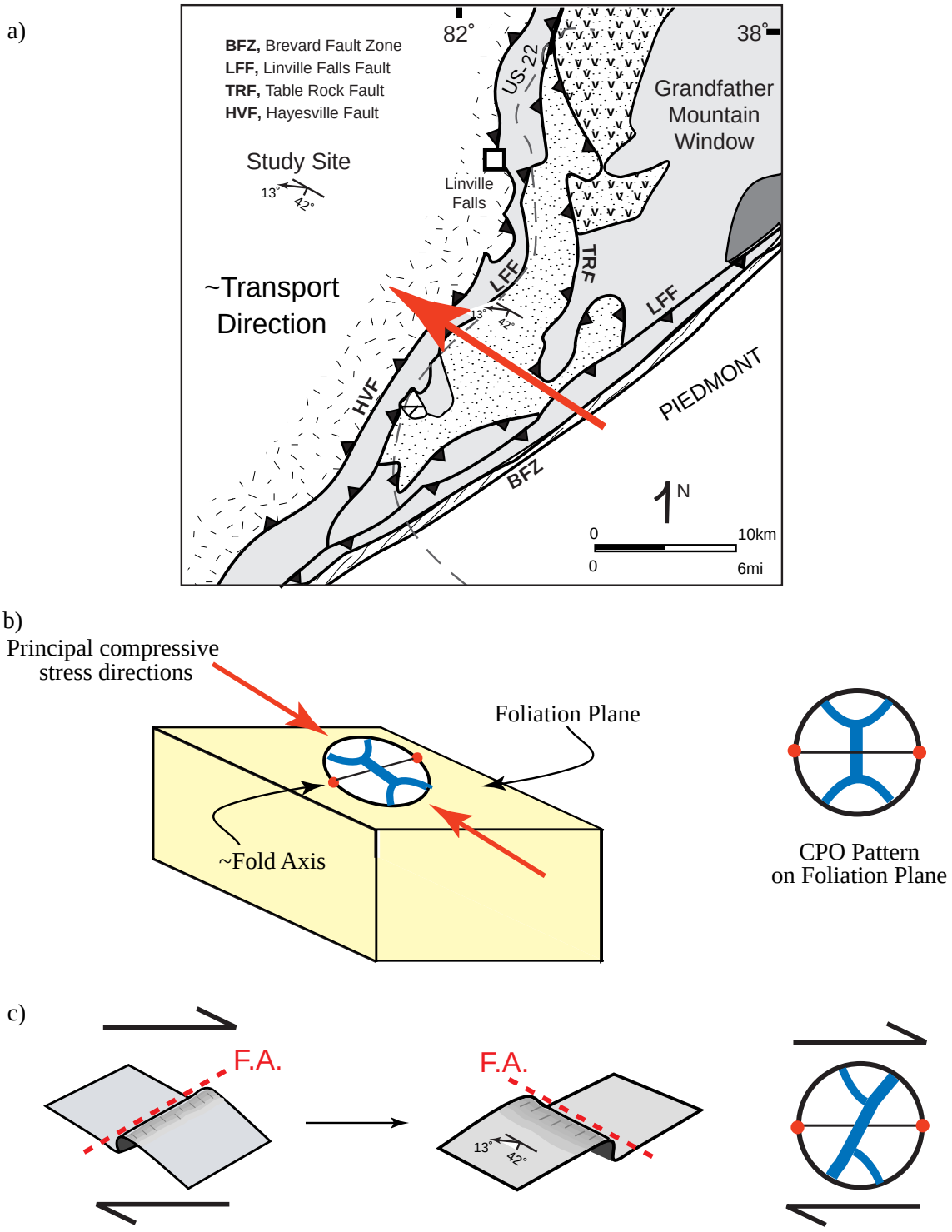

Fig. 26 a) Geologic map of Grandfather Mountain Window region. Red arrow designates the approximate direction of main layer shear (γ_1) along the Tablerock thrust fault during deformation. b) Model for development of an early CPO fabric during initial layer parallel shortening. Notice the approximated orientation of the fold axis (red dots) along the primitive of the stereoplot, and the symmetric Type I cross girdle CPO pattern. c) Schematic representation of dextral strike-rotation HPM of the Clinchfield Railroad fold, from its initial orientation to present day orientation.

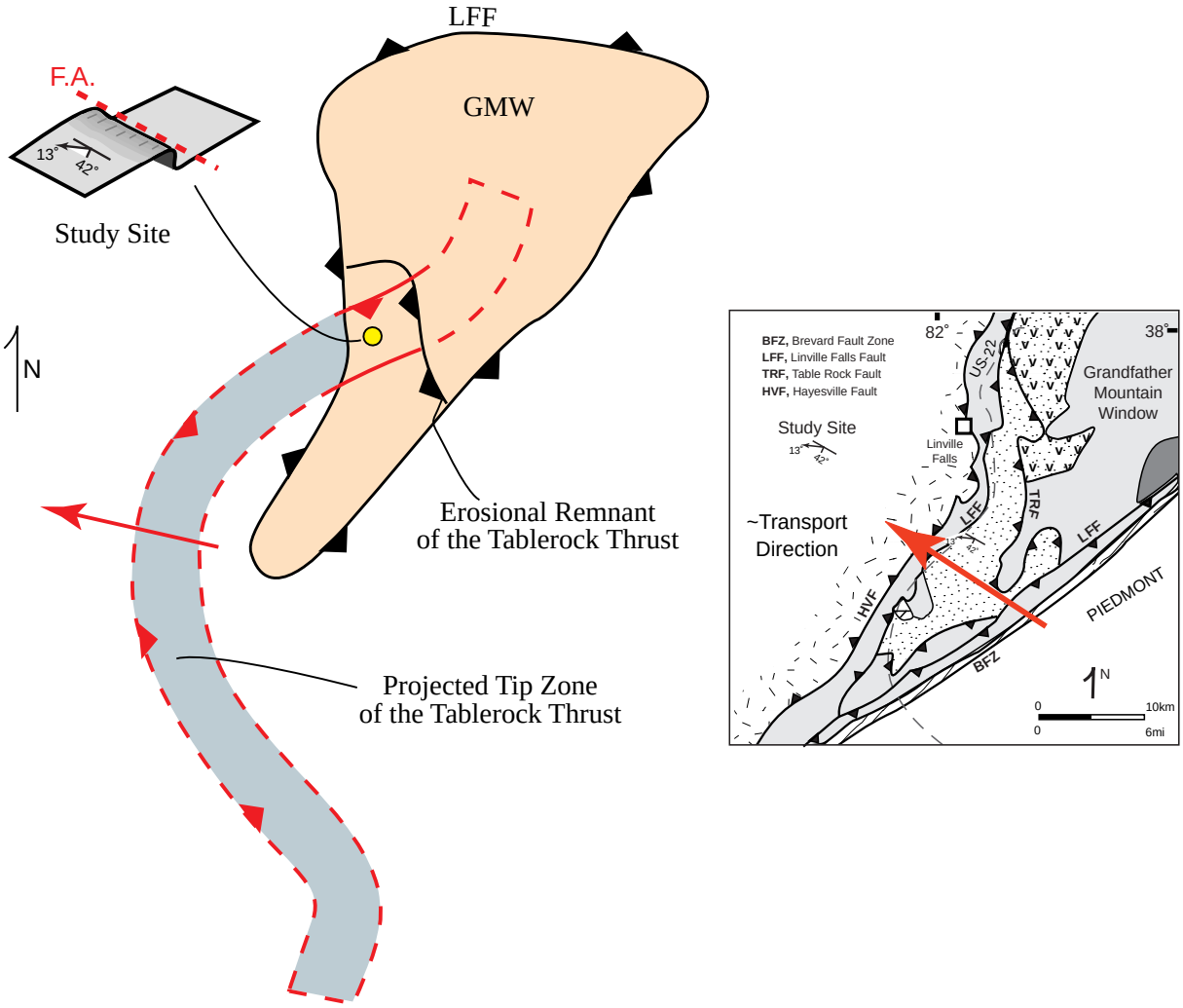

Fig. 27. Schematic outline of the tip region of the Tablerock thrust sheet within the Grandfather Mountain Window (outlined in red, shaded in orange) and projected orientation beneath the Linville Falls thrust sheet (outlined in red, shaded in gray). The study fold, highlighted in yellow, is located in the northern lateral region of the thrust tip. This lateral ramp would have experienced dextral differential shears, consistent with the orientation of the Clinchfield Railroad's fold axis and possibly the asymmetry displayed in CPO fabrics from the study site.

patterns (see Passchier and Trouw, Fig. 4.45b, 1996). This supports the inferred position of the Clinchfield Railroad fold within the Tablerock thrust sheet along the northern dextral-lateral region of the thrust (Fig. 27). This interpretation of the shear sense is not conclusive, given the modified nature of the CPO data (Figs. 12a-16a), but does provide evidence of multiple stages of CPO development and associated deformation.

6. Conclusions

Hinge plane migration is a change in the location or orientation of fold hinge(s) during either initial or subsequent folding events as a result of: i) dip-rotation, ii) strike-rotation, iii) material translation, and/or iv) lateral translation processes. Techniques for identifying folds that experienced hinge migration during deformation in natural studies have been limited to site specific and sometimes inconclusive methods. There exists a wide variety of natural strain markers in rocks and analytical techniques that can be used to conduct strain/grain shape analysis in folded layers. The use of grain shape fabric/strain analysis for identifying folds that experience hinge migration during deformation provides a more generally applicable method than those used in other natural studies.

Grain shape fabric analysis of the Clinchfield Railroad fold, in conjunction with previous theoretical studies regarding hinge migration during folding by Treagus and Treagus (1981), Coward and Potts (1983), and Ghosh et al. (1996), provide evidence that hinge migration processes were active during folding. Kinematic analysis of the fold provides further constraints on the specific hinge migration kinematic processes that were dominant during deformation, these processes include syn-folding material translation and post-folding strike-rotation. Application of the triaxial grain shape fabric/strain analysis, and other previously established methods allows for better identification of folds that have experienced hinge migration during deformation. Grain shape fabric/strain analysis as a tool for identifying folds whose hinges have migrated during deformation is useful because of the large variety of strain markers and rock types that can be used to conduct such analyses. Partitioning of finite strains into the limb and hinge regions of a fold can lead to important variations in rock properties, such as porosity and permeability, and the driving forces for metamorphic reactions. Understanding the kinematics and processes that were active throughout deformation, buckling, bending, and hinge migration, allows for better modeling, understanding, and prediction of changes in rock properties.

References

Bailey, C.M., and Brooks, J.S., 1996. Folds in Unicoi formation quartzite, Virginia: A case for hinge migration? Geological Society of America, Abstracts with Programs 28, 240.

Beutner, E.C., and Diegel, F.A., 1985. Determination of fold kinematics from syntectonic fibers in pressure shadows, Martinsburg Slate, New Jersey. American Journal of Science 285, 16-50.

Bezar, B.S., de Lamotte, D.F., Morel, J.L., and Mercier, E., 1998. Kinematics of large scale tip line folds from the High Atlas thrust belt, Morocco. Journal of Structural Geology 20, 999-1010.

Biot, M.A., 1961. Theory of folding of stratified viscoelastic media and its implications in tectonics and orogenesis. Geological Society of America Bulletin 72, 1595-1620.

Bons, P.D., and Urai, J.L. 1992. Syndeformational grain growth: microstructures and kinetics. Journal of Structural Geology 14, 1101-1109.

Borradaile, G.J., 1979. Strain study of the Caledonides in the Islay region, SW Scotland: Implications for strain histories and deformation mechanisms in greenschists. Journal of the Geological Society of London 136, 77-88.

Boyer, S.E. and Mitra, G., 1988. Relations between deformation of crystalline basement and sedimentary cover at the basement/cover transition zone of the Appalachian Blue Ridge Province. Geological Society of America Special Paper 222, 119-136.

Bryant, B., and Reed Jr., J.C., 1969. Significance of lineation and minor folds near major thrust faults in the southern Appalachians and the British and Norwegian Caledonides. Geological Magazine, 106, 412-429.

Bryant, B and Reed Jr., J.C., 1970. Geology of the Grandfather Mountain Window and Vicinity, North Carolina and Tennessee. United States Geological Survey Professional Paper 615, pp. 189.

Cook, F.A., Albaugh, D. S., Brown, L. D., Kaufman, S., Oliver, J. E., Hatcher, R. D., Jr., 1979. Thin-skinned tectonics in the crystalline southern Appalachians; COCORP seismic-reflection profiling of the Blue Ridge and Piedmont. Geology 7, 563-567.

Coward, M.P., and Potts, G.J., 1983. Complex strain patterns developed at the frontal and lateral tips to shear zones and thrust zones. Journal of Structural Geology 5, 383-399.

Dallmeyer, R.D., Wright, J.E., Secor, D.T., Jr., and Snoke, A.W., 1986. Character of the Alleghanian orogeny in the southern Appalachians: Part II. Geochronological constraints on the tectonothermal evolution of the eastern Piedmont in South Carolina. Geological Society of America Bulletin 96, 1329-1344.

De Paor, D.G., 1988. R_f/ϕ_f strain analysis using an orientation net. Journal of Structural Geology 10, 323-333.

De Paor, D.G., 1990. Determination of the strain ellipsoid from sectional data. Journal of Structural Geology 12, 131-137.

Dunnet, D., 1979. A technique of finite strain and initial shape from deformed elliptical objects. Tectonophysics 12, 307-325.

Elliott, D., 1976. The energy balance and deformation mechanisms of thrust sheets. Philosophical Transactions of the Royal Society of London A 283, 289-312

Flinn, D., 1962. On folding during three-dimensional progressive deformation. Quarterly Journal of the Geological Society of London 135, 385-433.

Fowler, T.J., and Winsor, C.N., 1996. Evolution of chevron folds by profile shape changes: comparison between multilayer deformation experiments and folds of the Bendigo-Castlemaine goldfields, Australia. Tectonophysics 258, 125-150.

Ghosh, S.K., Deb, S.K., and S. Sengupta, 1996. Hinge migration and hinge replacement. Tectonophysics 263, 319-337.

Gray, D.R., 1981. Cleavage-fold relationships and their implications for transected folds: An example from southwest Virginia, U.S.A.. Journal of Structural Geology 3, 265-277.

Groshong Jr., R.H., 1975. "Slip" cleavage caused by pressure solution in a buckle fold. Geology 3, 411-413.

Hatcher Jr., R.J. and Butler, J.B., 1986. Ocoee Gorge; Appalachian Valley and Ridge to Blue Ridge transition. Geological Society of America Centennial Field Guide - Southeastern Section, 265-270.

Hatcher Jr., R.J. and Goldberg, S.A., 1991. The Blue Ridge Geologic Province. In: Horton Jr., J.W., and Zullo, V.A., (Eds.), The Geology of the Carolinas. University of Tennessee Press., pp. 11-35.

Hatcher Jr., R.J., Hooper, R.J., McConnell, K.I., Heyn, T., and Costello, J.O., 1988. Geometric and time relationships between thrusts in the crystalline Southern Appalachians. Geological Society of America Special Paper 222, 185-196.

Hibbard, M.J., 1995. Petrography to Petrogenesis. Prentice-Hall, New Jersey, pp.587.

Hirth, G., and Tullis, J., 1992. Dislocation creep regimes in quartz aggregates. Journal of Structural Geology 14, 145-159.

Homza, T.X., and Wallace, W.K., 1995. Geometric and kinematic models for detachment folds with fixed and variable detachment depths. Journal of Structural Geology 17, 575-588.

Jamison, W.R., 1987. Geometric analysis of fold development in overthrust terraines. Journal of Structural Geology 9, 207-219.

Jonas, A.I., 1932. Structure of the metamorphic belt of the southern Appalachians. American Journal of Science 24, 228-243.

Law, R.D., 1990. Crystallographic fabrics: a select review of their applications to research in structural geology. In: Knipe, R.J., and Rutter, E.H., (Eds), Deformation Mechanisms, rheology, and tectonics. Geological Society Special Publication 54, p. 335-352.

Levin, H., 1992. The Earth through time. Saunders College Publishing, Fort Worth, pp. 651.

Lisle, R.J., 1985a. Geological strain analysis, a manual for the Rf/ϕ method. Pergamon Press, New York, 99 pp.

Lisle, R.J., 1985b. The use of the orientation tensor for description and statistical testing of fabrics. Journal of Structural Geology 7, 115-117.

Lister, G. S., Paterson, M. S., Hobbs, B. E., 1978. The simulation of fabric development in plastic deformation and its application to quartzite; the model. Tectonophysics 45, 107-158.

Lister, G.S., and Hobbs, B.E., 1980. The simulation of fabric development during plastic deformation and its application to quartzite: fabric transitions. Journal of Structural Geology 1, 99-115.

Lloyd, G.E., and Freeman, B., 1994. Dynamic recrystallization of quartz under greenschist facies conditions. Journal of Structural Geology 16, 867-881.

Lode, W., 1926. Versuche uber den Einfluss der mittleren Hauptspannung auf das Fliessen der Metalle Eisen, Kupfer and Nickel. Zeitschrift fuer Physik 36, 913-939.

Mardia, K.V., 1972. Statistics of Directional Data. Academic Press, London.

Merle, O., 1998. Emplacement Mechanisms of Nappes and Thrust Sheets. Kluwer Academic Publishers, Boston, pp. 158.

Miller, D.M., and Christie, J.M., 1981. Comparison of quartz microfabric with strain in recrystallized quartzite. Journal of Structural Geology 3, 129-141.

Milton, N.J., 1980. Determination of the strain ellipsoid from measurements on any three sections. Tectonophysics 64, T19-T27.

Nadai, A., 1963. Theory of Flow and Fracture of Solids, Volume 2. McGraw-Hill Book Company, Inc., New York.

Odonne, F., and Vialon, P., 1987. Hinge migration as a mechanism of superimposed folding. Journal of Structural Geology 9, 835-844.

Osberg, P.H., Tull, J.F., Robinson, P., Hon, R., and Butler, J.R., 1989. The Acadian Orogen. In: Hatcher Jr., R.D., Thomas, W.A., and Viele, G.W., (Ed.), The Appalachian-Ouchita Orogen in the United States. The Geology of North America Volume F-2, pp. 179-232.

Passchier, C.W., and Trouw, R.A.J., 1996. Microtectonics. Springer, New York, pp. 289.

Platt, J.P., and Behrmann, J.H., 1986. Structures and fabrics in a crustal-scale shear zone, Betic Coridllera, SE Spain. Journal of Structural Geology 8, 15-33.

Pryer, L.L., 1993. Microstructures in feldspars from a major crustal thrust zone: the Grenville Front, Ontario, Canada. Journal of Structural Geology 15, 21-36.

Ramberg, H., 1961. Contact strain and folding instability of a multilayered body under compression. Geologische Rundschau 51, 405-439.

Ramsay, J.G., 1967. Folding and fracturing of rocks. McGraw HIll, New York, pp. 568.

Rankin, D.W., 1970. Stratigraphy and structure of Precambrian rocks in northwestern North Carolina. In: Fisher, G.W., Pettijohn F.J., Reed Jr., J.C., and Weaver K.N., (Eds.), Appalachian Geology: Central and Southern. Interscience Publishers, New York, pp. 227-245.

Rankin, D.W., Dillon, W.P., Black, D.B., Boyer, S.E., Daniels, D.L., Goldsmith, R., Grow, J.A., Horton Jr., J.W., Hutchinson, D.R., Klitgord, K.D., McDowell, R.C., Milton, D.J., Owens, J.P., Phillips, J.D., with contributions by, Bayer, K.C., Butler, J.R., Elliot, D.W., and Millici, R.C., 1991. Centennial continent/ocean transect #16 E-4, Central Kentucky to the Carolina trough. The Geological Society of America, 41.

Ross, J.A., 1973. Mylonitic rocks and flattened garnets in the southern octanogen of British Columbia. Canadian Journal of Earth Science 10, 1-17.

Simon, R.I., and Gray, D.R., 1982. Interrelations of mesoscopic structures and strain across a small regional fold, Virginia Appalachians. Journal of Structural Geology 4, 271-289.

Simpson, E.L., and Eriksson, K.A., 1989. Sedimentology of the Unicoi Formation in southern and central Virginia: Evidence for late Proterozoic to Early Cambrian rift-to-passive margin transition. Geological Society of America Bulletin 101, 42-54.

Stewart, K.G., and Alvarez, W., 1991. Mobile-hinge kinking in layered rocks and models. Journal of Structural Geology 13, 243-259.

Suppe, J., 1983. Geometry and kinematics of fault-bend folding. American Journal of Science 283, 684-721.

Suppe, J., and Medwedeff, D.A., 1984. Fault-propagation folding. Geological Society of America Abstracts with Programs 16, 670.

Suppe, J., and Medwedeff, D.A., 1990. Geometry and kinematics of fault-propagation folding. Eclogae Geologisches Helvetica 83, 409-454.

Tagami, M., and Takeshita, T., 1998. C-axis fabrics and microstructures in quartz schist from the Sambagawa metamorphic belt, central Shikoku, Japan. Journal of Structural Geology 20, 1549-1568.

Treagus, J.E., and Treagus, S.H., 1981. Folds and the strain ellipsoid: a general model. Journal of Structural Geology 3, 1-17.

Trupe, C.H., 1999. Evidence for high ductile strains and high fluid pressures in the Tablerock thrust sheet, western North Carolina. Southeastern Section, Geological Society of America, Abstracts with Programs 31, A-72.

Tullis, J., and Yund, R.A., 1985. Dynamic recrystallization of feldspar: a mechanism for ductile shear zone formation. Geology 13, 238-241.

Turner, F.J., and Weiss, L.E., 1963. Structural analysis of metamorphic tectonites. McGraw Hill, New York, pp. 545.

Twiss, R.J., and Moores, E.M., 1992. Structural Geology. Freeman and Co., New York, pp.532.

Wheeler, J., 1986. Strain analysis in rocks with pretectonic fabrics. Journal of Structural Geology 8, 887-896.

Yund, R.A., and Tullis, J., 1991. Compositional changes of minerals associated with dynamic recrystallisation. Contributions Mineral Petrology 108, 346-355.

Software

De Paor, D.G, 1994. 2D-3D Compatibility. Earth'n Ware Inc., Hull MA..

De Paor, D.G., and Simpson, C., 1987. Rf/Fry 2.0.6. copyright, Earth'n Ware Inc., Hull MA..

Kanagawa, K., 1992. MacStrain 2.4 and 2D->3D Strain (QB). Tokyo, Japan.

Manktelow, N., 1997. Stereoplot 3.04. copyright, Neil Manktelow 1989-1997.

Starkey, J., 1989. Fabric 1.2. University of Western Ontario, London, Ontario.

Appendix I
Grain Shape Fabric Trends in Each Thin Section Plane by Inspection

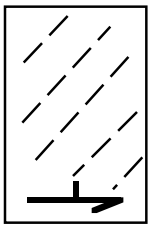

809-1a
well developed

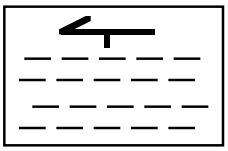

809-1b
well developed

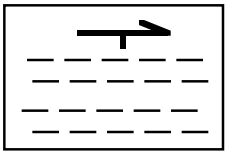

809-1c
weakly developed

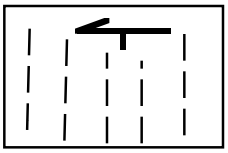

809-2a
weakly developed

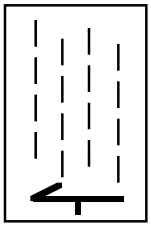

809-2b
moderately developed

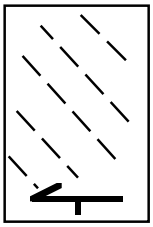

809-2c
well developed

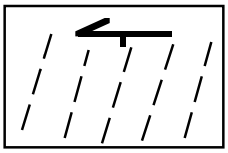

809--3a
weakly developed

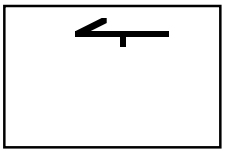

809--3b
very weakly developed

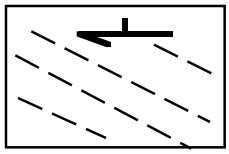

809-3c
well developed

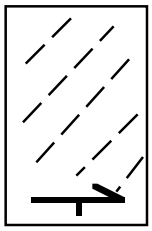

809-4a
moderately developed

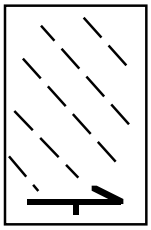

809-4b
moderately developed

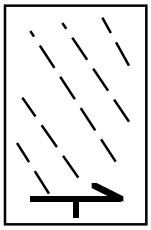

809-4c
moderately developed

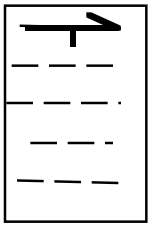

809-5a
well developed

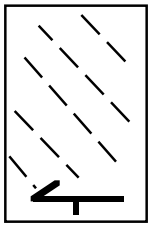

809-5b
well developed

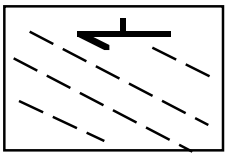

809-5c
well developed

Appendix II

a) Section Plane Orientation Information

Sample	Strike	Dip		Pole to G.C. Plunge	Pole to G.C. Trend
809-1a	030	79	SE	08	300
809-1b	116	58	NE	32	201
809-1c	**118**	**24**	**SW**	**66**	**044**
809-2a	154	80	W	10	064
809-2b	062	70	S	20	331
809-2c	**242**	**20**	**N**	**70**	**150**
809-3a	031	89	SE	01	301
809-3b	120	05	S	85	031
809-3c	**112**	**85**	**N**	**05**	**299**
809-4a	032	85	N	05	302
809-4b	298	55	NE	35	201
809-4c	**130**	**35**	**SW**	**55**	**041**
809-5a	031	88	NE	02	304
809-5b	295	15	NE	75	205
809-5c	**125**	**75**	**SW**	**15**	**033**

b) Rf/phi Analysis

Sample	Rs	Plot ϕ angle	Rake	Phi Plunge	Phi Trend	# of data points	S_1	S_2
809-1a	1.61013	41	41SW	40	201	60	1.3	0.8
809-1b	1.37	88	02SE	01	117	60	1.2	0.8
809-1c	1.5401	90	0	00	118	60	1.1	0.7
809-2a	1.23564	34	34NW	33	328	60	1.1	0.9
809-2b	1.45679	-24	66SW	59	226	60	1.2	0.8
809-2c	1.88295	-47	43SW	14	283	60	1.4	0.7
809-3a	1.3983	36	54NE	54	033	60	1.2	0.8
809-3b	1.37741	-41	49NW	05	261	60	1.2	0.9
809-3c	1.74086	-62	28NW	28	301	60	1.3	0.8
809-4a	1.7429	71	19NE	19	035	60	1.3	0.8
809-4b	1.4193	62	28SE	23	104	60	1.2	0.8
809-4c	1.45448	29	61SE	30	187	60	1.2	0.8
809-5a	1.68885	27	27S	27	214	60	1.3	0.8
809-5b	1.78132	72	18NW	04	312	60	1.3	0.7
809-5c	1.63169	-31	31S	30	134	60	1.3	0.8

c) 2D-3D Conversions

Sample	Strike	Dip	Sample ϕ angle	Rs new	S_1 new	S_2 new
809-1a	030	79	41	1.41	1.2	0.8
809-1b	296	58	02	1.2	1.2	1
809-1c	118	24	00	1.3	1.1	0.8
809-2a	154	80	56	1.16	1.1	0.95
809-2b	062	70	24	1.26	1.2	0.95
809-2c	242	20	43	1.56	1.25	0.8
809-3a	031	89	36	1.33	1.2	0.91
809-3b	120	05	131 (-41)	1.38	1.2	0.9
809-3c	292	85	118 (-62)	1.57	1.3	0.83
809-4a	212	85	71	1.51	1.3	0.9
809-4b	298	55	62	1.23	1.1	0.9
809-4c	130	35	29	1.29	1.1	0.8
809-5a	211	88	27	1.6	1.2	0.75
809-5b	295	15	18	1.73	1.3	0.75
809-5c	125	75	121 (-31)	1.56	1.25	0.8

d) Triaxial 2D->3D Strain Calculations

Sample #	magnitude *X*	orientation *X*	magnitude *Y*	orientation *Y*	magnitude *Z*	orientation *Z*	*k* value
809-1a							
809-1b	1.261	08, 143	1.002	51, 244	0.821	38, 047	1.17
809-1c							
809-2a							
809-2b	1.285	23, 287	0.964	58, 155	0.807	21, 026	1.71
809-2c							
809-3a							
809-3b	1.507	46, 301	0.906	15, 047	0.732	41, 150	2.79
809-3c							
809-4a							
809-4b	1.245	10, 038	1.004	24, 132	0.8	64, 287	0.94
809-4c							
809-5a							
809-5b	1.624	24, 159	0.917	23, 259	0.672	56, 028	2.11
809-5c							

Appendix III
Rf/f Plots - Samples 809-1 through 809-5

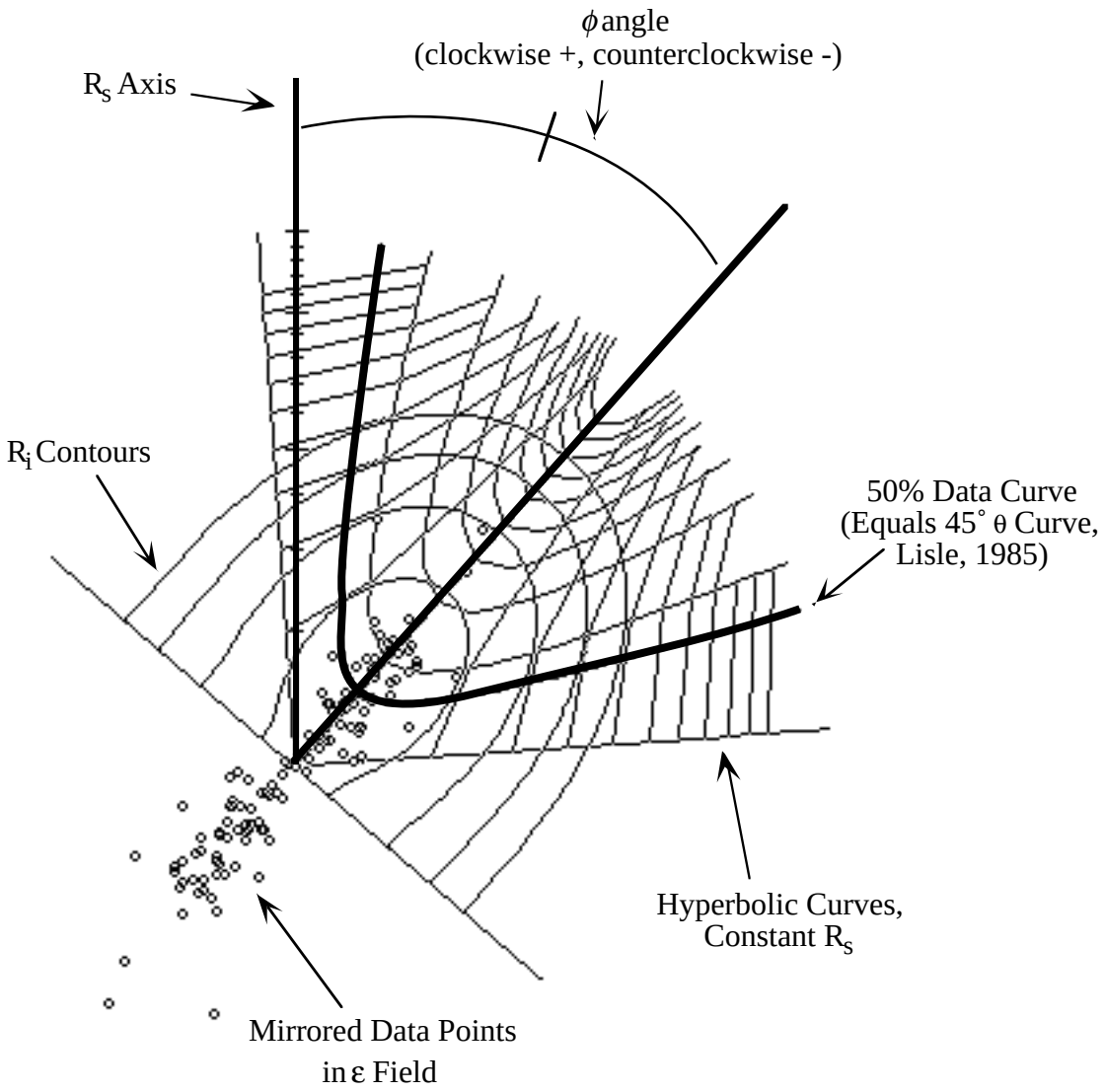

De Paor (1987) hyperbolic Rf/ϕ plots from Rf/Fry 2.0.6 with labels

***Not shown, Isogon curves that equal Lisle's, 1985, θ Curves

809-1a

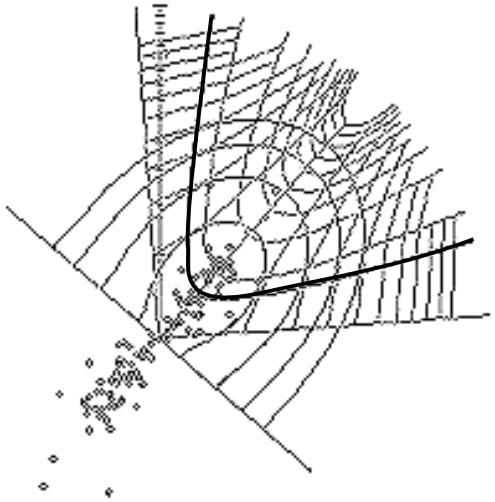

R_S = 1.6101
ϕ = 41˚
n = 60

809-1b

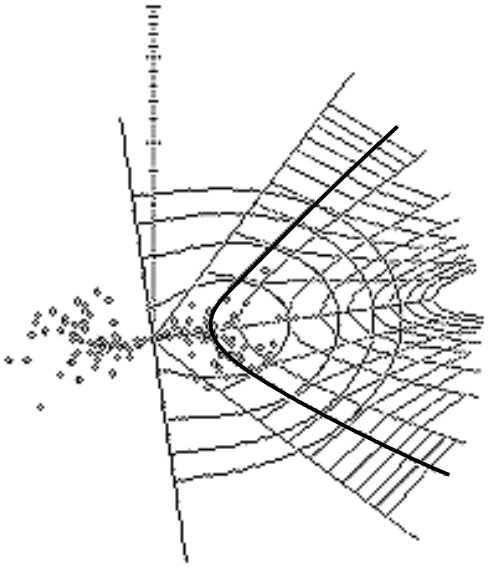

R_S = 1.5412
ϕ = 88˚
n = 60

809-1c

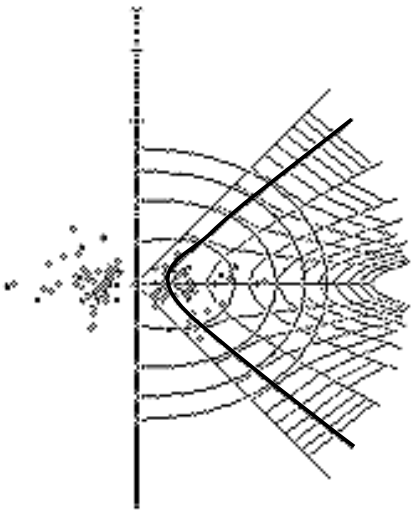

R_S = 1.317
ϕ = 90˚
n = 60

809-2a

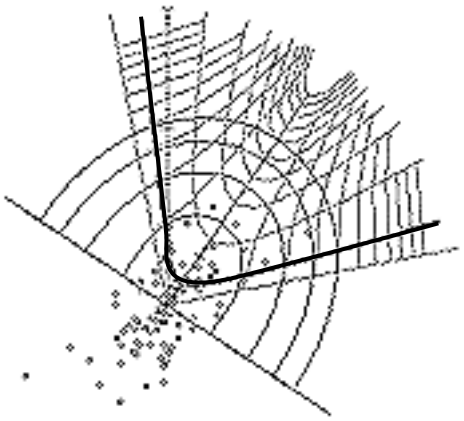

R_S = 1.2356
ϕ = 34°
n = 60

809-2b

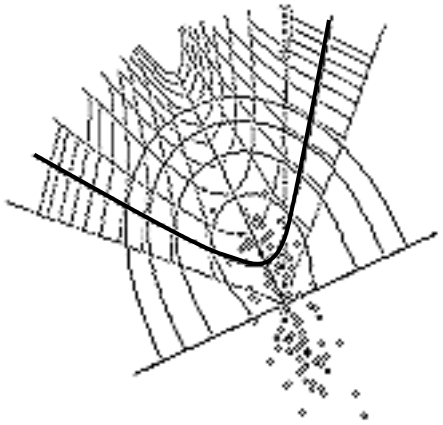

R_S= 1.4567
ϕ = -47°
n = 60

809-2c

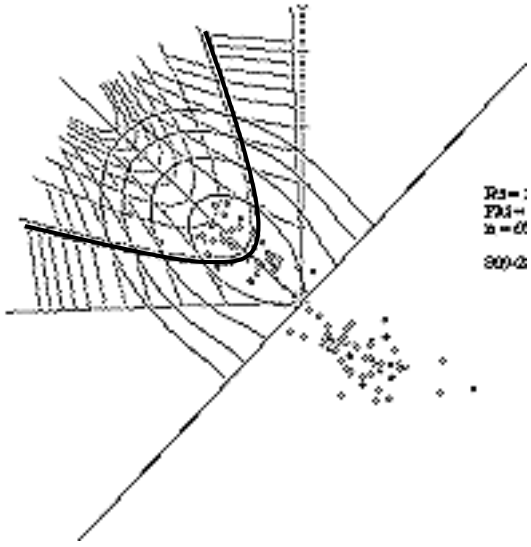

R_S = 1.8829
ϕ = -47°
n = 60

809-3a

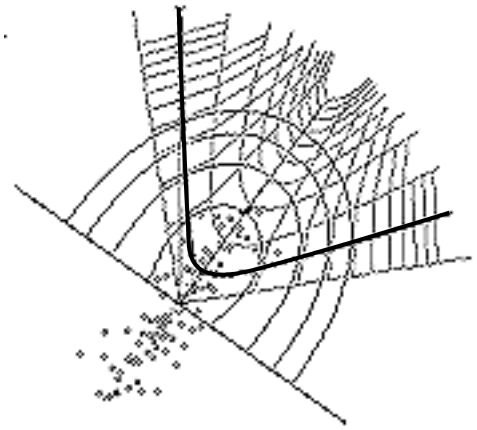

R_S = 1.3983
ϕ = 36°
n = 60

809-3b

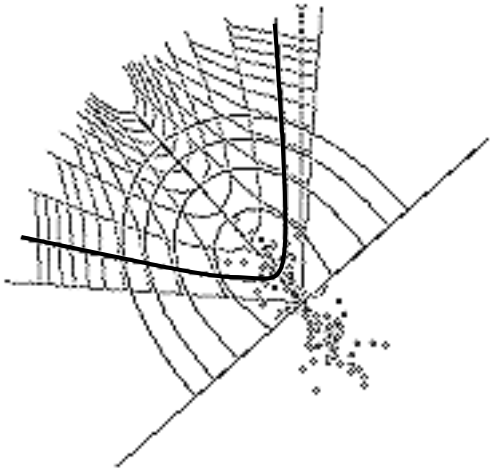

R_S= 1.3774
ϕ = -41°
n = 60

809-3c

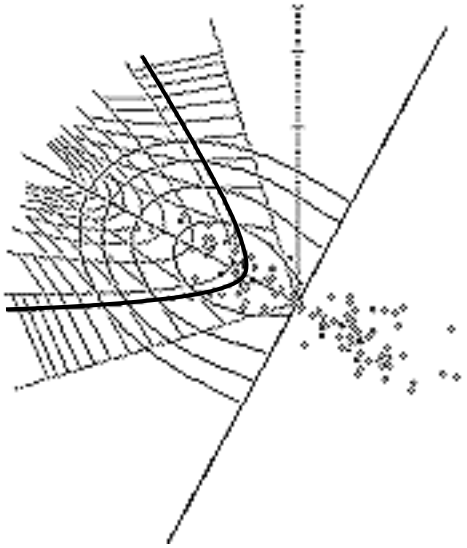

R_S = 1.7408
ϕ = -62°
n = 60

809-4a

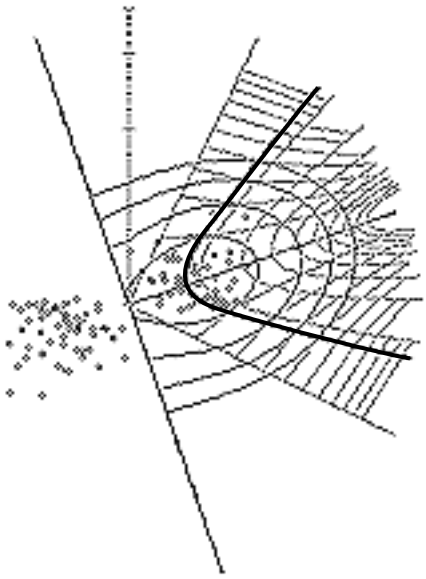

R_S = 1.7429
ϕ = 71°
n = 60

809-4b

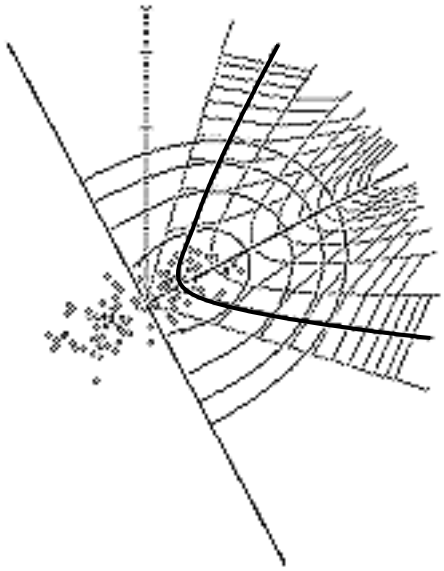

R_S= 1.4921
ϕ = 62°
n = 60

809-4c

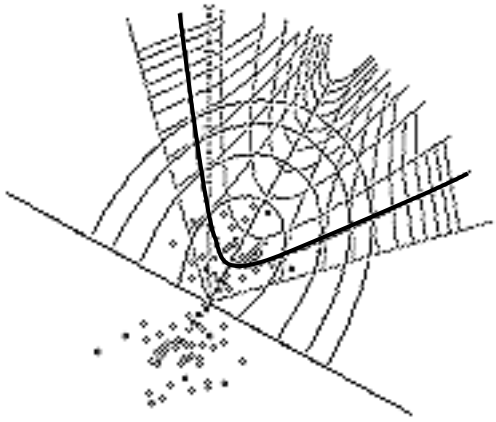

R_S = 1.4544
ϕ = 29°
n = 60

809-5a

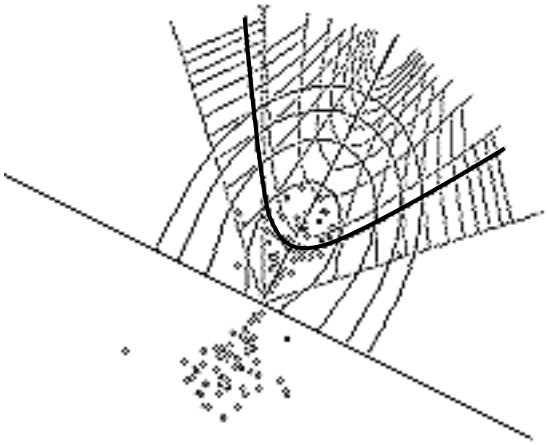

R_S = 1.68885
ϕ = 27°
n = 60

809-5b

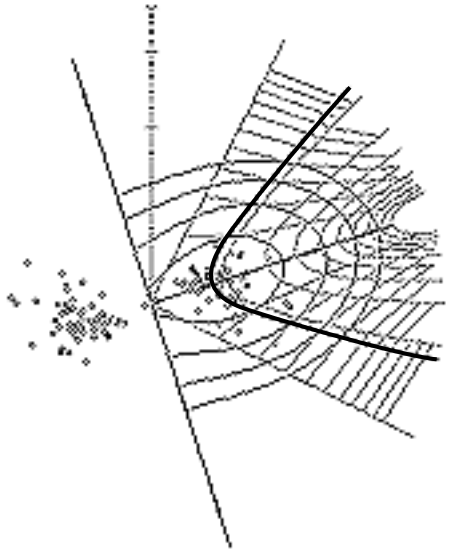

R_S= 1.78132
ϕ = 72°
n = 60

809-5c

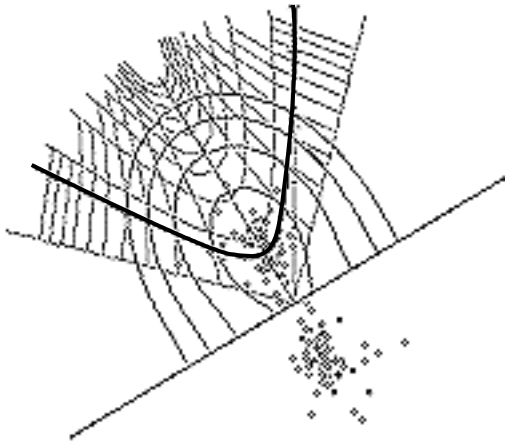

R_S = 1.63169
ϕ = -31°
n = 60

Appendix IV
Procedure for Analyzing of NC and VA Folds

1. Collect oriented samples from same bedding plane within fold and from limbs, hinge and nose of fold.

2. Calculate orientation of fold axis for each fold using stereonet, compare to measured fold axis orientation. Repeat for axial plane.

3. Cut three oriented, mutually perpendicular section planes in each sample with respect to orientation of sample and fold axis

4. Photograph three oriented thin sections for each sample

5. Use DePaor's Rf/Phi 2-D strain analysis program to calculate the strain ellipses for each thin section plane.

6. Tabulate resulting Rs and phi values

7. Spot check Rs and phi values via inspection of thin sections

8. Calculate orientation of section planes using stereonet conversions.
    a. Plot orientation of main bedding/foliation plane on stereo net (equal angle)
    b. Plot orientation of fold axis parallel, bedding perpendicular section (b for NC fold)
    c. Plot pole to main foliation great circle
    d. Plot pole to complimentary orientation plane
    e. Find best fit great circle between two poles for third orientation plane
    f. Use Rf/Phi plot and visual inspection to determine angles of phi in three section planes
    g. Plot pitch angle for each plane's linear fabric along its respective great circle
    h. Find best fit great circle that contains three pitches (should all fall relatively along the same great circle is phi's belong to a common ellipsoid).

9. Use DePaor's 2-D 3-D compatibility program to find S1 and S2 of ellipses on section plane and check compatibility of those ellipses to one another.

10. Use Macstrain to calculate the finite strain ellipsoid's principal axes for each sample

11. Relate the orientation of the long and short axes of the finite strain ellipsoid to the overall structure of the fold

12. Plot Flinn and Nadai Diagrams based on finite X, Y, and Z values for each sample

Appendix V
Derivation of Natural Octahedral Unit Shear Equation

Terms:

$\bar{\varepsilon}_S$ **= Natural logarithmic octahedral strain, magnitude of the strain (Nadai, 1963)**
γ_0 **= Octahedral unit shear (Nadai, 1963)**
v **= Lodes unit, defines the symmetry of the strain (Ross, 1973)**

Equations and derivations used for the Natural Strain (Nadai) Plot:

Natural Logarithmic Properties

1. $\ln(uv) = \ln u + \ln v$
2. $\ln \frac{u}{v} = \ln u - \ln v$
3. $\ln u^n = n \ln u$

If: $\gamma_0 = \frac{2}{3}\left[(E_1 - E_2)^2 + (E_2 - E_3)^2 + (E_3 - E_1)^2\right]^{\frac{1}{2}}$ (Nadai 1963)

And: $E = \ln \frac{L_1}{L_0}$ when $\frac{L_1}{L_0}$ =X or Y or Z (Ramsay 1967)

Then: E_1=lnX; E_2=lnY; E_3=lnZ

Therefore: $\gamma_0 = \frac{2}{3}\left[(\ln X - \ln Y)^2 + (\ln Y - \ln Z)^2 + (\ln Z - \ln X)^2\right]^{\frac{1}{2}}$

Using Property #2 from above:

$$\gamma_0 = \frac{2}{3}\left[\left(\ln\left(\frac{X}{Y}\right)\right)^2 + \left(\ln\left(\frac{Y}{Z}\right)\right)^2 + \left(\ln\left(\frac{Z}{X}\right)\right)^2\right]^{\frac{1}{2}}$$

And: $\bar{\varepsilon}_S = \left(\frac{\sqrt{3}}{2}\right)\gamma_0$ (Nadai 1963)

And: $\upsilon = \frac{\ln\left(\frac{Y}{Z}\right) - \ln\left(\frac{X}{Y}\right)}{\ln\left(\frac{X}{Z}\right)}$ (Ross 1973)

Appendix VI
I

I, a term first described by Lisle (1985b), is used to express the intensity or strength of fabrics where:

$$I = \frac{15}{2}\sum_{i=1}^{3}\left(S_i - \frac{1}{3}\right)^2 \qquad (3)$$

where S_I are the normalized eigenvalues of the orientation tensor. Lisle argues that *I* is a less biased means of determining certain shape fabrics than S_1/S_3 (Woodcock, 1977; Woodcock and Naylor, 1983) because the latter results in different, frequently asymmetric distributions for girdle-type fabrics than for unimodal clusters.

Lisle (1985b) reports that *I* varies from values of 0 to 5 for linear (unimodal) fabrics, and from 0 to 3.75 for planar (girdle) fabrics. Woodcock (1977) based on the work of Watson (1966) defined cluster patterns as those where $S_1>S_2=S_3$, and girdle patterns as $S_1=S_2>S_3$. Lisle argues that Woodcock's method of computing fabric symmetry results in an asymmetric distribution of data points between girdle-type fabrics and unimodal (cluster) type fabrics. Lisle uses Mardia's (1972) statistical techniques to argue that *I* is less biased towards certain fabric shapes than S_1/S_3 because the constant *I* curves plot parallel to the density contours of points on an S_1/S_2 vs. S_2/S_3 graph, while the S_1/S_3 curves deviate from the density curves (see Lisle, 1985b).

The statistical argument aside, Lisle's *I* value appears to have some serious shortfalls. This variable is generalized so that the uniformity or symmetry of any fabric type can be measured. However, basic tests based on theoretical data for strain ellipsoid symmetry reveals some problems with using *I* to describe the uniformity of a given fabric. Using the values of the primary ellipsoid axes as the eigenvalues for each system the strain magnitude and the strain symmetry (I_s) were calculated for three different systems, a) pure flattening strain, b) pure plane strain, and c) pure constrictional strain). Three x-y plots were constructed where the x axis was increasing values of strain symmetry (I_s) and the y axis equaled increasing values of strain magnitude (ε_s) (see the data and graphical plots on the following pages). All three fabrics should describe unimodal (cluster) type fabrics, and therefore should reach a maximum symmetry *I* of 5.0 according to Lisle. Both the pure constrictional and pure plane strain curves reached a maximum strain symmetry I_s of 5.0 with increasing strain magnitude (ε_s), pure plane strain, however, did not exceed a strain symmetry value (I_s) of 1.25 even for strain magnitudes (ε_s) exceeding those tested for pure plane strain and pure constrictional strain.

In addition to the apparent discrepancy between the states of strain, the theoretical curves discussed and Lisle's published study (1985b); the use of *I* by Tagami and Takeshita (1996) as a

means for correlating CPO girdle types with respect to the strain/grain shape magnitude (es) versus the fabric strength/intensity (*I*) is suspect. The use of *I* to describe the fabric strength/intensity of simple fabric patterns on stereonets, such as more linear patterns like those associated with great circle distributions or point concentration information such as the trend and plunge of a relatively constant lineation throughout a region, appears to work. However, more complex scatter patterns, like Type I CPO distributions, are not easily resolved by Lisle's (1985b) *I* parameter. The combination of small circle and cross girdle distributions in these patterns are not resolved by Lisle's strength parameter, *I*.

I Calculations

magnitude *X*	magnitude *Y*	magnitude *Z*	*k* value	Sample
1.261	1.002	0.821	1.17	809-1
1.285	0.964	0.807	1.71	809-2
1.507	0.906	0.732	2.79	809-3
1.245	1.004	0.8	0.94	809-4
1.624	0.917	0.672	2.11	809-5

Strain Magnitude and Lodes Unit Calculations

(LN (*X*/*Y*))^2	(LN(*Y*/*Z*))^2	(LN(*Z*/*X*))^2	Sum	SQR Root			v
0.0529	0.0397	0.1842	0.2767	0.5260	0.3507	**0.3037**	**-0.0715**
0.0826	0.0316	0.2164	0.3306	0.5750	0.3833	**0.3320**	**-0.2357**
0.2589	0.0455	0.5214	0.8258	0.9087	0.6058	**0.5247**	**-0.4093**
0.0463	0.0516	0.1956	0.2935	0.5417	0.3612	**0.3128**	**0.0271**
0.3267	0.0966	0.7786	1.2019	1.0963	0.7309	**0.6330**	**-0.2954**

magnitude *X*	magnitude *Y*	magnitude *Z*	*k* value	Sample
1.261	1.002	0.821	1.17	809-1
1.285	0.964	0.807	1.71	809-2
1.507	0.906	0.732	2.79	809-3
1.245	1.004	0.8	0.94	809-4
1.624	0.917	0.672	2.11	809-5

Lisle's Fabric Symmetry Calculation for the Grain Shape Fabric

X/*Y*	*Y*/*Z*	(*X*/*Y*)^2	(*Y*/*Z*)^2				I (gsf)
1.258	1.220	1.584	1.490	4.849	14.111	0.344	**0.077**
1.333	1.195	1.777	1.427	4.962	14.340	0.346	**0.095**
1.663	1.238	2.767	1.532	6.770	18.459	0.367	**0.251**
1.240	1.255	1.538	1.575	4.997	14.526	0.344	**0.080**
1.771	1.365	3.136	1.862	8.702	22.860	0.381	**0.355**

Constrictional Strains Theoretical Data pg1

magnitude X	magnitude Y	magnitude Z	K value	Test Values	No Volume Loss	(LN (X/Y))^2	(LN(Y/Z))^2	(LN(Z/X))^2	Sum	SQR Root	Octahedral Unit Shear	Natural Logarithmic Octahedral Strain	v	S1/S3
1	1	1.00E+00	#DIV/0!	1	1.00	0	0	0	0	0	0	**0**	**#DIV/0!**	1
1.24	0.9	9.00E-01	#DIV/0!	2	1.00	0.10270224	0	0.10270224	0.20540447	0.4532157	0.3021438	**0.2616642**	**-1**	1.37777778
1.39	0.85	8.50E-01	#DIV/0!	3	1.00	0.24188955	0	0.24188955	0.48377909	0.6955423	0.46369487	**0.4015715**	**-1**	1.63529412
1.56	0.8	8.00E-01	#DIV/0!	4	1.00	0.44599607	0	0.44599607	0.89199214	0.94445336	0.62963557	**0.5452804**	**-1**	1.95
1.77	0.75	7.50E-01	#DIV/0!	5	1.00	0.73729978	0	0.73729978	1.47459955	1.21433091	0.80955394	**0.7010943**	**-1**	2.36
2.05	0.7	7.00E-01	#DIV/0!	6	1.00	1.15458192	0	1.15458192	2.30916384	1.51959331	1.01306221	**0.8773376**	**-1**	2.92857143
2.36	0.65	6.50E-01	#DIV/0!	7	1.00	1.66266721	0	1.66266721	3.32533442	1.82354995	1.21569997	**1.0528271**	**-1**	3.63076923
2.77	0.6	6.00E-01	#DIV/0!	8	1.00	2.33989932	0	2.33989932	4.67979863	2.16328422	1.44218948	**1.2489727**	**-1**	4.61666667
3.3	0.55	5.50E-01	#DIV/0!	9	1.00	3.210402	0	3.210402	6.42080399	2.53393054	1.68928703	**1.4629655**	**-1**	6
3.99	0.5	5.00E-01	#DIV/0!	10	1.00	4.31367317	0	4.31367317	8.62734633	2.93723447	1.95815631	**1.6958131**	**-1**	7.98
4.95	0.45	4.50E-01	#DIV/0!	11	1.00	5.74990174	0	5.74990174	11.4998035	3.39113602	2.26075734	**1.9578733**	**-1**	11
6.25	0.4	4.00E-01	#DIV/0!	12	1.00	7.55629835	0	7.55629835	15.1125967	3.88749234	2.59166156	**2.2444447**	**-1**	15.625
8.2	0.35	3.50E-01	#DIV/0!	13	1.00	9.94744021	0	9.94744021	19.8948804	4.46036774	2.9735785	**2.5751945**	**-1**	23.4285714
11.1	0.3	3.00E-01	#DIV/0!	14	1.00	13.0387282	0	13.0387282	26.0774563	5.10660908	3.40440606	**2.9483021**	**-1**	37
16	0.25	2.50E-01	#DIV/0!	15	1.00	17.2963085	0	17.2963085	34.592617	5.88154886	3.92103257	**3.3957138**	**-1**	64
25	0.2	2.00E-01	#DIV/0!	16	1.00	23.3126135	0	23.3126135	46.6252271	6.82826677	4.55217785	**3.9423017**	**-1**	125
44.5	0.15	1.50E-01	#DIV/0!	17	1.00	32.4057992	0	32.4057992	64.8115984	8.0505651	5.3670434	**4.6479959**	**-1**	296.666667
100	0.1	1.00E-01	#DIV/0!	18	1.00	47.717083	0	47.717083	95.434166	9.7690412	6.51269413	**5.6401586**	**-1**	1000
400	0.05	5.00E-02	#DIV/0!	19	1.00	80.7697067	0	80.7697067	161.539413	12.7098156	8.47321042	**7.3380155**	**-1**	8000
495	0.045	4.50E-02	#DIV/0!	20	1.00	86.5951322	0	86.5951322	173.190264	13.1601772	8.77345148	**7.5980319**	**-1**	11000
625	0.04	4.00E-02	#DIV/0!	21	1.00	93.2504542	0	93.2504542	186.500908	13.6565335	9.10435569	**7.8846033**	**-1**	15625
820	0.035	3.50E-02	#DIV/0!	22	1.00	101.238039	0	101.238039	202.476079	14.2294089	9.48627263	**8.2153531**	**-1**	23428.5714
1110	0.03	3.00E-02	#DIV/0!	23	1.00	110.642486	0	110.642486	221.284971	14.8756503	9.91710019	**8.5884607**	**-1**	37000
1600	0.025	2.50E-02	#DIV/0!	24	1.00	122.470485	0	122.470485	244.940969	15.6505901	10.4337267	**9.0358724**	**-1**	64000
2500	0.02	2.00E-02	#DIV/0!	25	1.00	137.735316	0	137.735316	275.470632	16.597308	11.064872	**9.5824602**	**-1**	125000
4425	0.015	1.50E-02	#DIV/0!	26	1.00	158.62724	0	158.62724	317.25448	17.8116389	11.8744259	**10.283555**	**-1**	295000
10000	0.01	1.00E-02	#DIV/0!	27	1.00	190.868332	0	190.868332	381.736664	19.5380824	13.0253883	**11.280317**	**-1**	1000000
40000	0.005	5.00E-03	#DIV/0!	28	1.00	252.649502	0	252.649502	505.299004	22.4788568	14.9859046	**12.978174**	**-1**	8000000
49500	0.0045000	4.50E-03	#DIV/0!	29	1.00	262.874529	0	262.874529	525.749057	22.9292184	15.2861456	**13.23819**	**-1**	11000000
62500	0.0040000	4.00E-03	#DIV/0!	30	1.00	274.378776	0	274.378776	548.757552	23.4255747	15.6170498	**13.524762**	**-1**	15625000
82000	0.0035000	3.50E-03	#DIV/0!	31	1.00	287.962805	0	287.962805	575.925609	23.9984501	15.9989668	**13.855512**	**-1**	23428571.4
111000	0.0030000	3.00E-03	#DIV/0!	32	1.00	303.680409	0	303.680409	607.360818	24.6446915	16.4297943	**14.228619**	**-1**	37000000
160000	0.0025000	2.50E-03	#DIV/0!	33	1.00	323.078827	0	323.078827	646.157654	25.4196313	16.9464208	**14.676031**	**-1**	64000000
250000	0.0020000	2.00E-03	#DIV/0!	34	1.00	347.592184	0	347.592184	695.184369	26.3663492	17.5775661	**15.222619**	**-1**	125000000
442500	0.0015000	1.50E-03	#DIV/0!	35	1.00	380.346957	0	380.346957	760.693914	27.5806801	18.3871201	**15.923713**	**-1**	295000000
1000000	0.0010000	1.00E-03	#DIV/0!	36	1.00	429.453747	0	429.453747	858.907494	29.3071236	19.5380824	**16.920476**	**-1**	1000000000
4000000	0.0005000	5.00E-04	#DIV/0!	37	1.00	519.963464	0	519.963464	1039.92693	32.247898	21.4985987	**18.618333**	**-1**	8000000000
4950000	0.0004500	4.50E-04	#DIV/0!	38	1.00	534.588091	0	534.588091	1069.17618	32.6982596	21.7988397	**18.878349**	**-1**	1.1E+10
6250000	0.0004000	4.00E-04	#DIV/0!	39	1.00	550.941264	0	550.941264	1101.88253	33.1946159	22.129744	**19.16492**	**-1**	1.5625E+10
8200000	0.0003500	3.50E-04	#DIV/0!	39	1.00	570.121736	0	570.121736	1140.24347	33.7674913	22.5116609	**19.49567**	**-1**	2.3429E+10
11100000	0.0003000	3.00E-04	#DIV/0!	40	1.00	592.152499	0	592.152499	1184.305	34.4137327	22.9424885	**19.868778**	**-1**	3.7E+10
16000000	0.0002500	2.50E-04	#DIV/0!	41	1.00	619.121335	0	619.121335	1238.24267	35.1886725	23.459115	**20.31619**	**-1**	6.4E+10
25000000	0.0002000	2.00E-04	#DIV/0!	41	1.00	652.883219	0	652.883219	1305.76644	36.1353904	24.0902602	**20.862777**	**-1**	1.25E+11

Constrictional Strains Theoretical Data pg2

magnitude X	magnitude Y	magnitude Z	K value	Test Values	X/Y	Y/Z		(X/Y)^2	(Y/Z)^2				I
1	1	1.00E+00	#DIV/0!	1	1	1		1	1	3	9	0.33333333	2.5E-08
1.24	0.9	9.00E-01	#DIV/0!	2	1.377777778	1		1.8982716	1	3.8982716	11.4093827	0.34167244	0.0625433
1.39	0.85	8.50E-01	#DIV/0!	3	1.635294118	1		2.67418685	1	4.67418685	13.2153633	0.3536934	0.1527006
1.56	0.8	8.00E-01	#DIV/0!	4	1.95	1		3.8025	1	5.8025	15.6025	0.37189553	0.2892165
1.77	0.75	7.50E-01	#DIV/0!	5	2.36	1		5.5696	1	7.5696	19.0096	0.3981988	0.4864911
2.05	0.7	7.00E-01	#DIV/0!	6	2.928571429	1		8.57653061	1	10.5765306	24.2908163	0.43541273	0.7655955
2.36	0.65	6.50E-01	#DIV/0!	7	3.630769231	1		13.1824852	1	15.1824852	31.7055621	0.47885873	1.0914405
2.77	0.6	6.00E-01	#DIV/0!	8	4.616666667	1		21.3136111	1	23.3136111	43.7802778	0.53251401	1.4938551
3.3	0.55	5.50E-01	#DIV/0!	9	6	1		36	1	38	64	0.59375	1.953125
3.99	0.5	5.00E-01	#DIV/0!	10	7.98	1		63.6804	1	65.6804	99.6004	0.65943912	2.4457934
4.95	0.45	4.50E-01	#DIV/0!	11	11	1		121	1	123	169	0.72781065	2.9585799
6.25	0.4	4.00E-01	#DIV/0!	12	15.625	1		244.140625	1	246.140625	310.640625	0.79236457	3.4427343
8.2	0.35	3.50E-01	#DIV/0!	13	23.42857143	1		548.897959	1	550.897959	646.612245	0.85197576	3.8898182
11.1	0.3	3.00E-01	#DIV/0!	14	37	1		1369	1	1371	1521	0.90138067	4.2603551
16	0.25	2.50E-01	#DIV/0!	15	64	1		4096	1	4098	4356	0.94077135	4.5557851
25	0.2	2.00E-01	#DIV/0!	16	125	1		15625	1	15627	16129	0.96887594	4.7665696
44.5	0.15	1.50E-01	#DIV/0!	17	296.6666667	1		88011.1111	1	88013.1111	89201.7778	0.98667441	4.9000581
100	0.1	1.00E-01	#DIV/0!	18	1000	1		1000000	1	1000002	1004004	0.99601396	4.9701047
400	0.05	5.00E-02	#DIV/0!	19	8000	1		64000000	1	64000002	64032004	0.99950022	4.9962517
495	0.045	4.50E-02	#DIV/0!	20	11000	1		121000000	1	121000002	121044004	0.99963648	4.9972736
625	0.04	4.00E-02	#DIV/0!	21	15625	1		244140625	1	244140627	244203129	0.99974406	4.9980805
820	0.035	3.50E-02	#DIV/0!	22	23428.57143	1		548897959	1	548897961	548991677	0.99982929	4.9987197
1110	0.03	3.00E-02	#DIV/0!	23	37000	1		1369000000	1	1369000002	1369148004	0.9998919	4.9991893
1600	0.025	2.50E-02	#DIV/0!	24	64000	1		4096000000	1	4096000002	4096256004	0.9999375	4.9995313
2500	0.02	2.00E-02	#DIV/0!	25	125000	1		1.5625E+10	1	1.5625E+10	1.5626E+10	0.999968	4.99976
4425	0.015	1.50E-02	#DIV/0!	26	295000	1		8.7025E+10	1	8.7025E+10	8.7026E+10	0.99998644	4.9998983
10000	0.01	1.00E-02	#DIV/0!	27	1000000	1		1E+12	1	1E+12	1E+12	0.999996	4.99997
40000	0.005	5.00E-03	#DIV/0!	28	8000000	1		6.4E+13	1	6.4E+13	6.4E+13	0.9999995	4.9999963
49500	0.0045000	4.50E-03	#DIV/0!	29	11000000	1		1.21E+14	1	1.21E+14	1.21E+14	0.99999964	4.9999973
62500	0.0040000	4.00E-03	#DIV/0!	30	15625000	1		2.4414E+14	1	2.4414E+14	2.4414E+14	0.99999974	4.9999981
82000	0.0035000	3.50E-03	#DIV/0!	31	23428571.43	1		5.489E+14	1	5.489E+14	5.489E+14	0.99999983	4.9999987
111000	0.0030000	3.00E-03	#DIV/0!	32	37000000	1		1.369E+15	1	1.369E+15	1.369E+15	0.99999989	4.9999992
160000	0.0025000	2.50E-03	#DIV/0!	33	64000000	1		4.096E+15	1	4.096E+15	4.096E+15	0.99999994	4.9999996
250000	0.0020000	2.00E-03	#DIV/0!	34	125000000	1		1.5625E+16	1	1.5625E+16	1.5625E+16	0.99999997	4.9999998
442500	0.0015000	1.50E-03	#DIV/0!	35	295000000	1		8.7025E+16	1	8.7025E+16	8.7025E+16	0.99999999	4.9999999
1000000	0.0010000	1.00E-03	#DIV/0!	36	1000000000	1		1E+18	1	1E+18	1E+18	1	5
4000000	0.0005000	5.00E-04	#DIV/0!	37	8000000000	1		6.4E+19	1	6.4E+19	6.4E+19	1	5
4950000	0.0004500	4.50E-04	#DIV/0!	38	11000000000	1		1.21E+20	1	1.21E+20	1.21E+20	1	5
6250000	0.0004000	4.00E-04	#DIV/0!	39	15625000000	1		2.4414E+20	1	2.4414E+20	2.4414E+20	1	5
8200000	0.0003500	3.50E-04	#DIV/0!	39	23428571429	1		5.489E+20	1	5.489E+20	5.489E+20	1	5
11100000	0.0003000	3.00E-04	#DIV/0!	40	37000000000	1		1.369E+21	1	1.369E+21	1.369E+21	1	5
16000000	0.0002500	2.50E-04	#DIV/0!	41	64000000000	1		4.096E+21	1	4.096E+21	4.096E+21	1	5
25000000	0.0002000	2.00E-04	#DIV/0!	41	1.25E+11	1		1.5625E+22	1	1.5625E+22	1.5625E+22	1	5

Constrictional Strains Theoretical Data pg3

I	Es
2.5E-08	0
0.06254331	0.26166421
0.15270056	0.40157153
0.2892165	0.5452804
0.48649106	0.70109428
0.76559549	0.87733761
1.0914405	1.05282705
1.49385507	1.24897273
1.95312503	1.46296548
2.44579342	1.69581311
2.95857991	1.95787329
3.44273429	2.24444475
3.88981823	2.57519452
4.26035505	2.94830213
4.55578515	3.39571382
4.76656956	3.94230166
4.90005807	4.64799593
4.97010473	5.64015857
4.99625167	7.33801548
4.99727362	7.59803186
4.99808046	7.88460332
4.99871973	8.21535309
4.99918929	8.5884607
4.9995313	9.03587239
4.99976003	9.58246023
4.99989833	10.2835545
4.99997003	11.2803171
4.99999628	12.978174
4.9999973	13.2381904
4.99999811	13.5247619
4.99999874	13.8555117
4.99999921	14.2286193
4.99999956	14.676031
4.99999979	15.2226188
4.99999992	15.9237131
5	16.9204757
5.00000002	18.6183326
5.00000002	18.878349
5.00000002	19.1649205
5.00000002	19.4956702
5.00000002	19.8687778
5.00000002	20.3161895
5.00000002	20.8627774

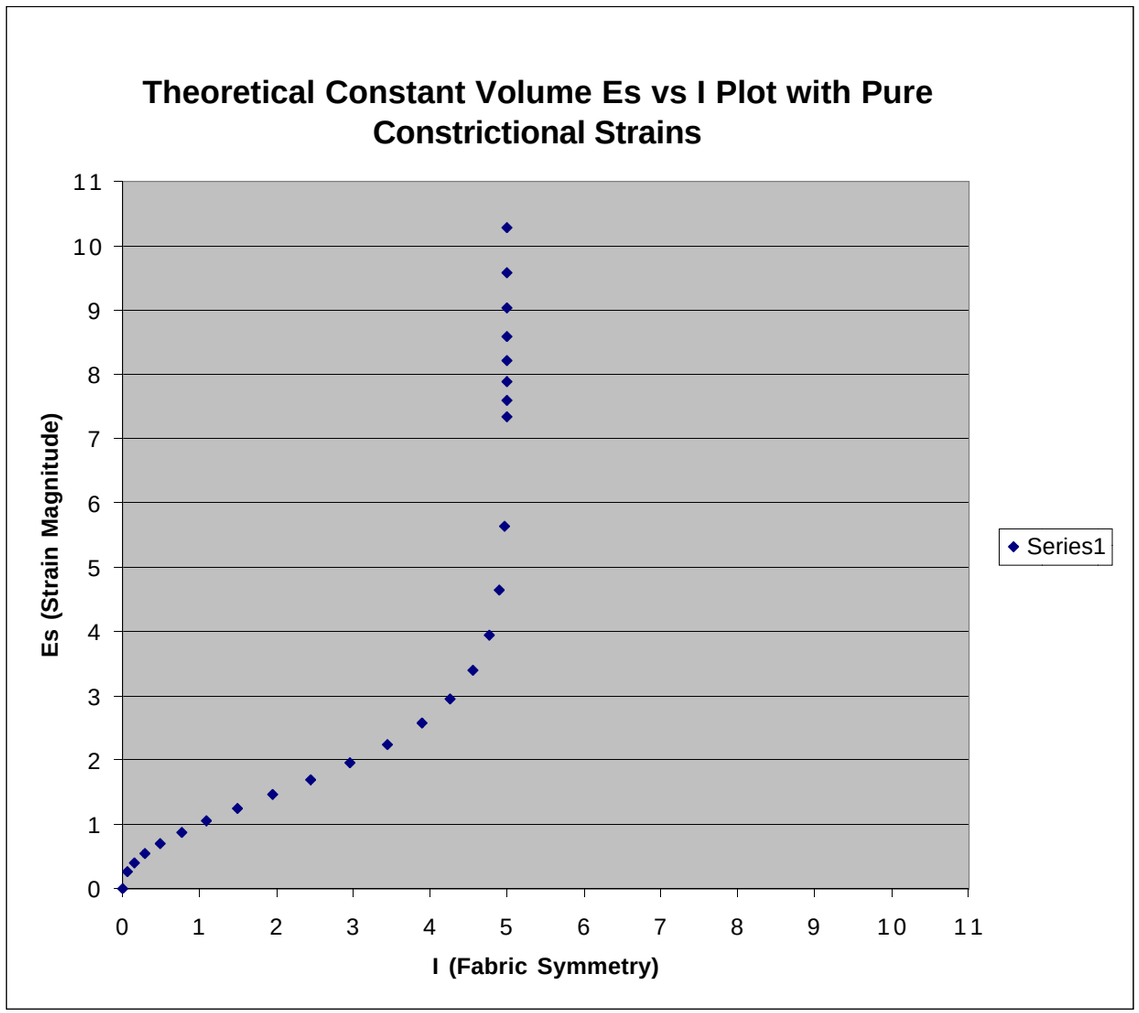

Constrictional Strains Theoretical Data pg4

S1/S3	Es
1	0
1.37777778	0.26166421
1.63529412	0.40157153
1.95	0.5452804
2.36	0.70109428
2.92857143	0.87733761
3.63076923	1.05282705
4.61666667	1.24897273
6	1.46296548
7.98	1.69581311
11	1.95787329
15.625	2.24444475
23.4285714	2.57519452
37	2.94830213
64	3.39571382
125	3.94230166
296.666667	4.64799593
1000	5.64015857
8000	7.33801548
11000	7.59803186
15625	7.88460332
23428.5714	8.21535309
37000	8.5884607
64000	9.03587239
125000	9.58246023
295000	10.2835545
1000000	11.2803171
8000000	12.978174
11000000	13.2381904
15625000	13.5247619
23428571.4	13.8555117
37000000	14.2286193
64000000	14.676031
125000000	15.2226188
295000000	15.9237131
1000000000	16.9204757
8000000000	18.6183326
1.1E+10	18.878349
1.5625E+10	19.1649205
2.3429E+10	19.4956702
3.7E+10	19.8687778
6.4E+10	20.3161895

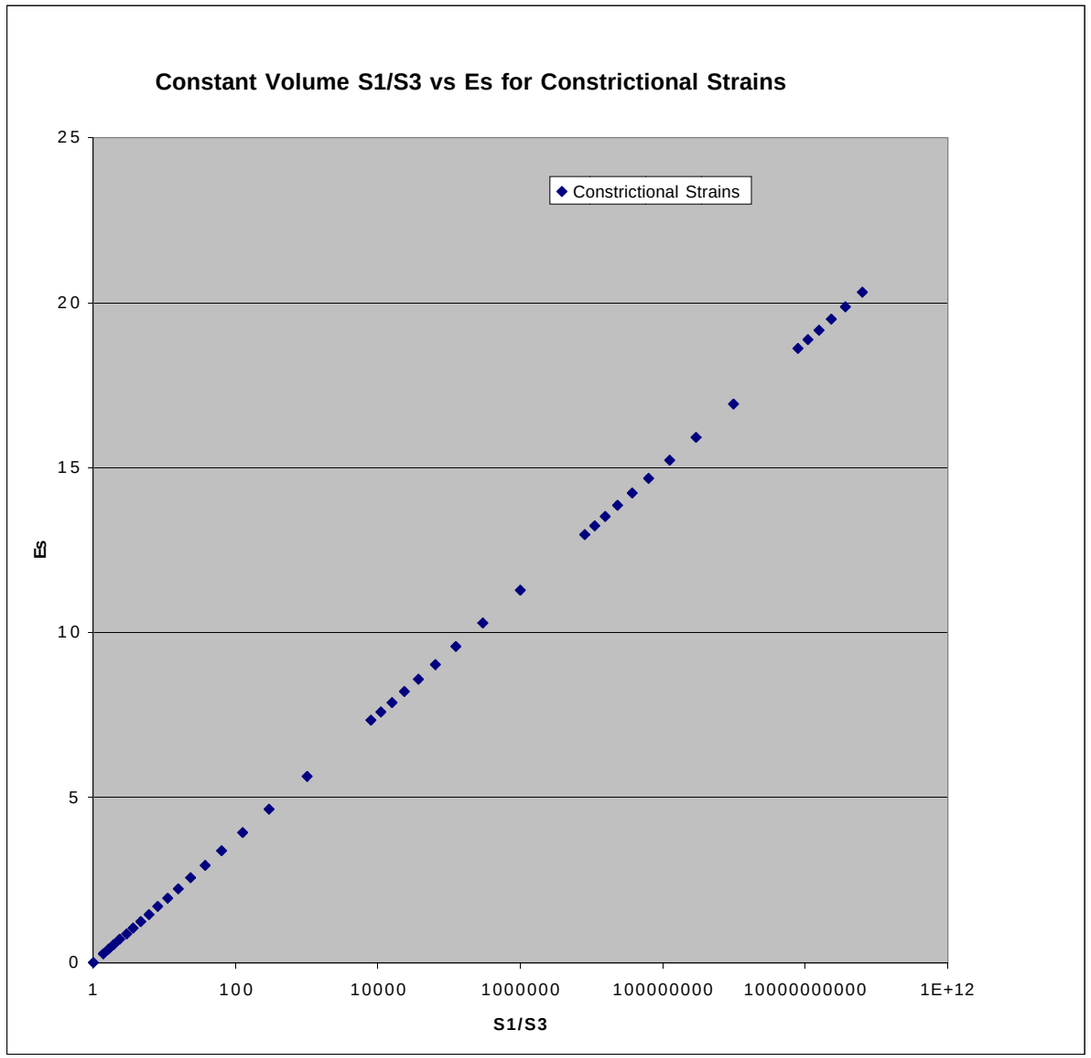

Constrictional Strains Theoretical Data pg2

magnitude X	magnitude Y	magnitude Z	K value	Test Values	X/Y	Y/Z		(X/Y)^2	(Y/Z)^2				I
1	1	1.00E+00	#DIV/0!	1	1	1		1	1	3	9	0.33333333	2.5E-08
1.24	0.9	9.00E-01	#DIV/0!	2	1.377777778	1		1.8982716	1	3.8982716	11.4093827	0.34167244	0.0625433
1.39	0.85	8.50E-01	#DIV/0!	3	1.635294118	1		2.67418685	1	4.67418685	13.2153633	0.3536934	0.1527006
1.56	0.8	8.00E-01	#DIV/0!	4	1.95	1		3.8025	1	5.8025	15.6025	0.37189553	0.2892165
1.77	0.75	7.50E-01	#DIV/0!	5	2.36	1		5.5696	1	7.5696	19.0096	0.3981988	0.4864911
2.05	0.7	7.00E-01	#DIV/0!	6	2.928571429	1		8.57653061	1	10.5765306	24.2908163	0.43541273	0.7655955
2.36	0.65	6.50E-01	#DIV/0!	7	3.630769231	1		13.1824852	1	15.1824852	31.7055621	0.47885873	1.0914405
2.77	0.6	6.00E-01	#DIV/0!	8	4.616666667	1		21.3136111	1	23.3136111	43.7802778	0.53251401	1.4938551
3.3	0.55	5.50E-01	#DIV/0!	9	6	1		36	1	38	64	0.59375	1.953125
3.99	0.5	5.00E-01	#DIV/0!	10	7.98	1		63.6804	1	65.6804	99.6004	0.65943912	2.4457934
4.95	0.45	4.50E-01	#DIV/0!	11	11	1		121	1	123	169	0.72781065	2.9585799
6.25	0.4	4.00E-01	#DIV/0!	12	15.625	1		244.140625	1	246.140625	310.640625	0.79236457	3.4427343
8.2	0.35	3.50E-01	#DIV/0!	13	23.42857143	1		548.897959	1	550.897959	646.612245	0.85197576	3.8898182
11.1	0.3	3.00E-01	#DIV/0!	14	37	1		1369	1	1371	1521	0.90138067	4.2603551
16	0.25	2.50E-01	#DIV/0!	15	64	1		4096	1	4098	4356	0.94077135	4.5557851
25	0.2	2.00E-01	#DIV/0!	16	125	1		15625	1	15627	16129	0.96887594	4.7665696
44.5	0.15	1.50E-01	#DIV/0!	17	296.6666667	1		88011.1111	1	88013.1111	89201.7778	0.98667441	4.9000581
100	0.1	1.00E-01	#DIV/0!	18	1000	1		1000000	1	1000002	1004004	0.99601396	4.9701047
400	0.05	5.00E-02	#DIV/0!	19	8000	1		64000000	1	64000002	64032004	0.99950022	4.9962517
495	0.045	4.50E-02	#DIV/0!	20	11000	1		121000000	1	121000002	121044004	0.99963648	4.9972736
625	0.04	4.00E-02	#DIV/0!	21	15625	1		244140625	1	244140627	244203129	0.99974406	4.9980805
820	0.035	3.50E-02	#DIV/0!	22	23428.57143	1		548897959	1	548897961	548991677	0.99982929	4.9987197
1110	0.03	3.00E-02	#DIV/0!	23	37000	1		1369000000	1	1369000002	1369148004	0.9998919	4.9991893
1600	0.025	2.50E-02	#DIV/0!	24	64000	1		4096000000	1	4096000002	4096256004	0.9999375	4.9995313
2500	0.02	2.00E-02	#DIV/0!	25	125000	1		1.5625E+10	1	1.5625E+10	1.5626E+10	0.999968	4.99976
4425	0.015	1.50E-02	#DIV/0!	26	295000	1		8.7025E+10	1	8.7025E+10	8.7026E+10	0.99998644	4.9998983
10000	0.01	1.00E-02	#DIV/0!	27	1000000	1		1E+12	1	1E+12	1E+12	0.999996	4.99997
40000	0.005	5.00E-03	#DIV/0!	28	8000000	1		6.4E+13	1	6.4E+13	6.4E+13	0.9999995	4.9999963
49500	0.0045000	4.50E-03	#DIV/0!	29	11000000	1		1.21E+14	1	1.21E+14	1.21E+14	0.99999964	4.9999973
62500	0.0040000	4.00E-03	#DIV/0!	30	15625000	1		2.4414E+14	1	2.4414E+14	2.4414E+14	0.99999974	4.9999981
82000	0.0035000	3.50E-03	#DIV/0!	31	23428571.43	1		5.489E+14	1	5.489E+14	5.489E+14	0.99999983	4.9999987
111000	0.0030000	3.00E-03	#DIV/0!	32	37000000	1		1.369E+15	1	1.369E+15	1.369E+15	0.99999989	4.9999992
160000	0.0025000	2.50E-03	#DIV/0!	33	64000000	1		4.096E+15	1	4.096E+15	4.096E+15	0.99999994	4.9999996
250000	0.0020000	2.00E-03	#DIV/0!	34	125000000	1		1.5625E+16	1	1.5625E+16	1.5625E+16	0.99999997	4.9999998
442500	0.0015000	1.50E-03	#DIV/0!	35	295000000	1		8.7025E+16	1	8.7025E+16	8.7025E+16	0.99999999	4.9999999
1000000	0.0010000	1.00E-03	#DIV/0!	36	1000000000	1		1E+18	1	1E+18	1E+18	1	5
4000000	0.0005000	5.00E-04	#DIV/0!	37	8000000000	1		6.4E+19	1	6.4E+19	6.4E+19	1	5
4950000	0.0004500	4.50E-04	#DIV/0!	38	11000000000	1		1.21E+20	1	1.21E+20	1.21E+20	1	5
6250000	0.0004000	4.00E-04	#DIV/0!	39	15625000000	1		2.4414E+20	1	2.4414E+20	2.4414E+20	1	5
8200000	0.0003500	3.50E-04	#DIV/0!	39	23428571429	1		5.489E+20	1	5.489E+20	5.489E+20	1	5
11100000	0.0003000	3.00E-04	#DIV/0!	40	37000000000	1		1.369E+21	1	1.369E+21	1.369E+21	1	5
16000000	0.0002500	2.50E-04	#DIV/0!	41	64000000000	1		4.096E+21	1	4.096E+21	4.096E+21	1	5
25000000	0.0002000	2.00E-04	#DIV/0!	41	1.25E+11	1		1.5625E+22	1	1.5625E+22	1.5625E+22	1	5

Constrictional Strains Theoretical Data pg3

I	Es
2.5E-08	0
0.06254331	0.26166421
0.15270056	0.40157153
0.2892165	0.5452804
0.48649106	0.70109428
0.76559549	0.87733761
1.0914405	1.05282705
1.49385507	1.24897273
1.95312503	1.46296548
2.44579342	1.69581311
2.95857991	1.95787329
3.44273429	2.24444475
3.88981823	2.57519452
4.26035505	2.94830213
4.55578515	3.39571382
4.76656956	3.94230166
4.90005807	4.64799593
4.97010473	5.64015857
4.99625167	7.33801548
4.99727362	7.59803186
4.99808046	7.88460332
4.99871973	8.21535309
4.99918929	8.5884607
4.9995313	9.03587239
4.99976003	9.58246023
4.99989833	10.2835545
4.99997003	11.2803171
4.99999628	12.978174
4.9999973	13.2381904
4.99999811	13.5247619
4.99999874	13.8555117
4.99999921	14.2286193
4.99999956	14.676031
4.99999979	15.2226188
4.99999992	15.9237131
5	16.9204757
5.00000002	18.6183326
5.00000002	18.878349
5.00000002	19.1649205
5.00000002	19.4956702
5.00000002	19.8687778
5.00000002	20.3161895
5.00000002	20.8627774

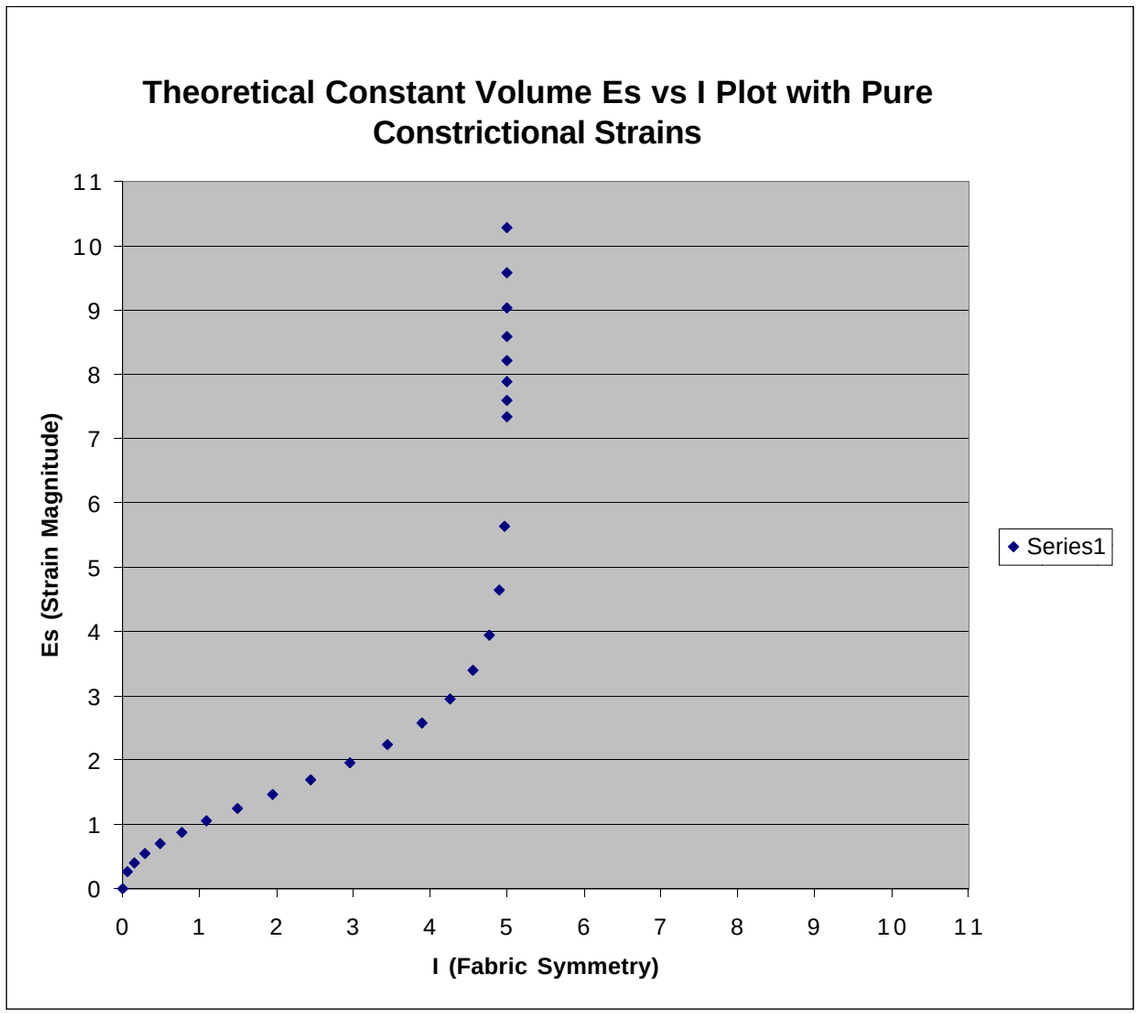

Constrictional Strains Theoretical Data pg4

S1/S3	Es
1	0
1.37777778	0.26166421
1.63529412	0.40157153
1.95	0.5452804
2.36	0.70109428
2.92857143	0.87733761
3.63076923	1.05282705
4.61666667	1.24897273
6	1.46296548
7.98	1.69581311
11	1.95787329
15.625	2.24444475
23.4285714	2.57519452
37	2.94830213
64	3.39571382
125	3.94230166
296.666667	4.64799593
1000	5.64015857
8000	7.33801548
11000	7.59803186
15625	7.88460332
23428.5714	8.21535309
37000	8.5884607
64000	9.03587239
125000	9.58246023
295000	10.2835545
1000000	11.2803171
8000000	12.978174
11000000	13.2381904
15625000	13.5247619
23428571.4	13.8555117
37000000	14.2286193
64000000	14.676031
125000000	15.2226188
295000000	15.9237131
1000000000	16.9204757
8000000000	18.6183326
1.1E+10	18.878349
1.5625E+10	19.1649205
2.3429E+10	19.4956702
3.7E+10	19.8687778
6.4E+10	20.3161895

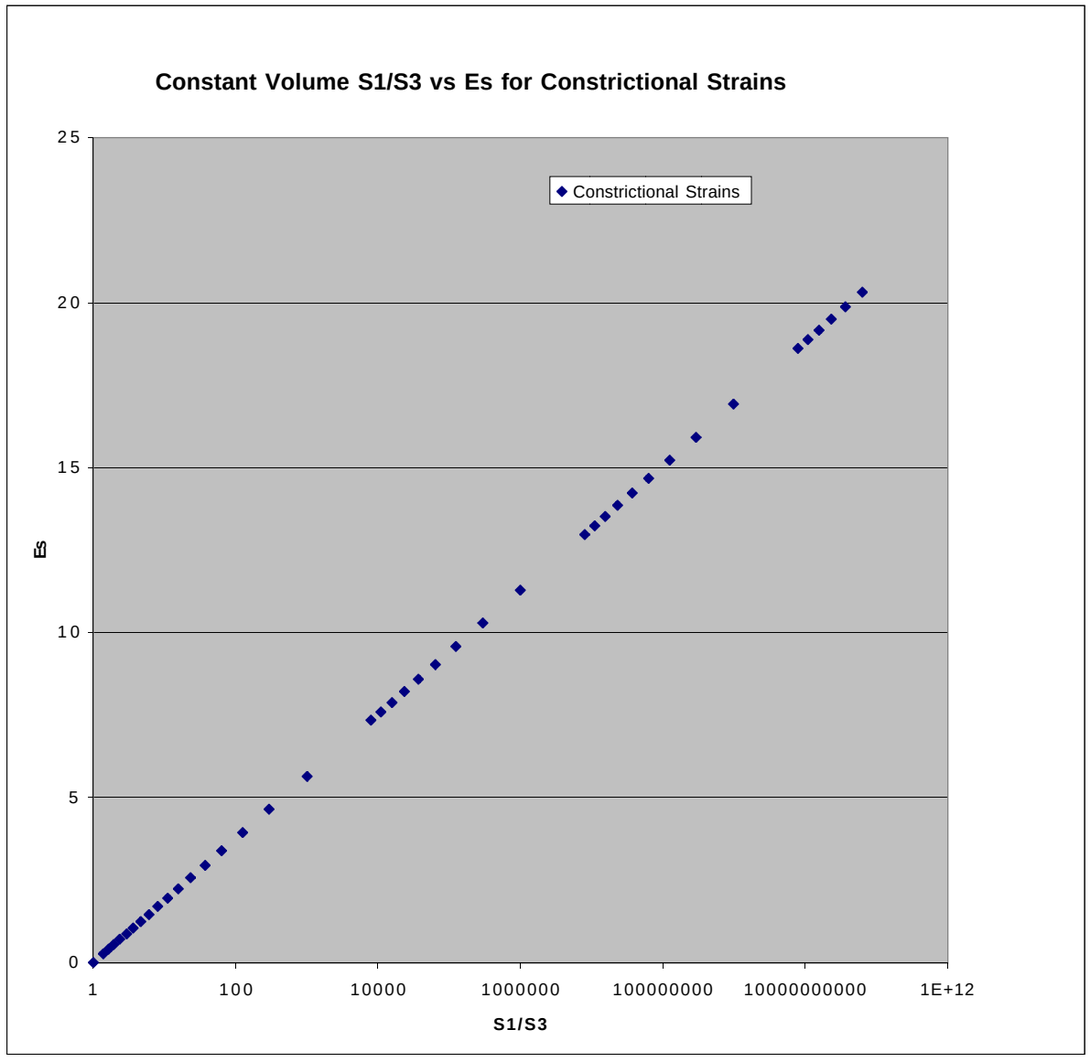

Plane Strain Theoretical Data pg1

magnitude X	magnitude Y	magnitude Z	K value	Test Values	No Volume Loss	(LN (X/Y))^2	(LN(Y/Z))^2	(LN(Z/X))^2	Sum	SQR Root	Octahedral Unit Shear	Natural Logarithmic Octahedral Strain	v	S1/S3
1	1	1	#DIV/0!	1	1.00	0	0	0	0	0	0	0	#DIV/0!	1
1.5	1	0.666	1.00	2	1.00	0.16440195	0.16521429	0.65923149	0.98884773	0.99440823	0.66293882	0.5741219	0.0012322	2.25225225
2	1	0.5	1.00	3	1.00	0.48045301	0.48045301	1.92181206	2.88271808	1.69785691	1.13190461	0.9802581	0	4
2.5	1	0.4	1.00	4	1.00	0.83958871	0.83958871	3.35835482	5.03753223	2.24444475	1.4962965	1.2958308	0	6.25
3	1	0.333	1.00	5	1.00	1.20694896	1.20914829	4.83219349	7.24829074	2.69226498	1.79484332	1.5543799	0.0004551	9.00900901
3.5	1	0.285	1.00	6	1.00	1.56941506	1.57569298	6.2902098	9.43531784	3.07169625	2.0477975	1.7734447	0.000998	12.2807018
4	1	0.2499	1.00	7	1.00	1.92181206	1.92292147	7.6894669	11.5342004	3.39620383	2.26413588	1.9607992	0.0001443	16.0064026
4.5	1	0.223	1.00	8	1.00	2.26224882	2.25175086	9.02798715	13.5419868	3.67994386	2.45329591	2.1246166	-0.0011628	20.1793722
5	1	0.2	1.00	9	1.00	2.59029039	2.59029039	10.3611616	15.5417424	3.94230166	2.62820111	2.2760889	0	25
5.5	1	0.182	1.00	10	1.00	2.90616606	2.90275926	11.6178496	17.426775	4.17453889	2.78302593	2.4101712	-0.0002932	30.2197802
6	1	0.166	1.00	11	1.00	3.210402	3.22478088	12.8703497	19.3055326	4.39380616	2.92920411	2.5367652	0.0011172	36.1445783
6.5	1	0.154	1.00	12	1.00	3.50364339	3.49990265	14.0070911	21.0106371	4.58373615	3.0558241	2.6464213	-0.0002671	42.2077922
7	1	0.143	1.00	13	1.00	3.78656631	3.78267743	15.1384865	22.7077302	4.76526287	3.17684191	2.7512258	-0.0002569	48.951049
7.5	1	0.133	1.00	14	1.00	4.05983418	4.06992758	16.2595173	24.389279	4.93855029	3.29236686	2.8512733	0.0006208	56.3909774
8	1	0.125	1.00	15	1.00	4.32407713	4.32407713	17.2963085	25.9444628	5.09357073	3.39571382	2.9407744	0	64
8.5	1	0.118	1.00	16	1.00	4.57988318	4.56707098	18.2938994	27.4408535	5.23840181	3.49226787	3.0243927	-0.0007004	72.0338983
9	1	0.111	1.00	17	1.00	4.82779584	4.83219349	19.3199777	28.979967	5.38330447	3.58886965	3.1080523	0.0002276	81.0810811
9.5	1	0.105	1.00	18	1.00	5.06831476	5.07959158	20.2958064	30.4437128	5.51758215	3.6783881	3.1855775	0.0005556	90.4761905
10	1	0.1	1.00	19	1.00	5.30189811	5.30189811	21.2075924	31.8113887	5.64015857	3.76010571	3.2563471	0	100
20	1	0.05	1.00	20	1.00	8.97441185	8.97441185	35.8976474	53.8464711	7.33801548	4.89201032	4.2366052	0	400
30	1	0.0333	1.00	21	1.00	11.5681436	11.5749504	46.2861871	69.4292812	8.33242349	5.55494899	4.8107269	0.0001471	900.900901
40	1	0.025	1.00	22	1.00	13.6078316	13.6078316	54.4313265	81.6469898	9.03587239	6.02391492	5.2168634	0	1600
50	1	0.02	1.00	23	1.00	15.303924	15.303924	61.215696	91.823544	9.58246023	6.38830682	5.532436	0	2500
60	1	0.0167	1.00	24	1.00	16.7636574	16.7473004	67.0219115	100.532869	10.0266081	6.68440538	5.7888649	-0.0002441	3592.81437
70	1	0.0143	1.00	25	1.00	18.0497118	18.0412201	72.1818628	108.272795	10.4054214	6.93694761	6.0075729	-0.0001176	4895.1049
80	1	0.0125	1.00	26	1.00	19.2021574	19.2021574	76.8086297	115.212945	10.7337293	7.15581953	6.1971215	0	6400
90	1	0.0111	1.00	27	1.00	20.2482871	20.2572922	81.0111575	121.516737	11.023463	7.34897534	6.3643993	0.0001112	8108.10811
100	1	0.01	1.00	28	1.00	21.2075924	21.2075924	84.8303698	127.245555	11.2803171	7.52021142	6.5126941	0	10000
200	1	0.005	1.00	29	1.00	28.0721669	28.0721669	112.288668	168.433001	12.978174	8.65211603	7.4929523	0	40000
300	1	0.00333	1.00	30	1.00	32.5331345	32.5445488	130.155366	195.233049	13.972582	9.31505469	8.067074	8.77E-05	90090.0901
400	1	0.0025	1.00	31	1.00	35.8976474	35.8976474	143.59059	215.385885	14.676031	9.78402063	8.4732104	0	160000
500	1	0.002	1.00	32	1.00	38.6213538	38.6213538	154.485415	231.728123	15.2226188	10.1484125	8.7887831	0	250000
600	1	0.00167	1.00	33	1.00	40.920709	40.8951508	163.631716	245.447576	15.6667666	10.4445111	9.0452119	-0.0001562	359281.437
700	1	0.00143	1.00	34	1.00	42.9166536	42.9035589	171.640424	257.460636	16.04558	10.6970533	9.2639199	-7.629E-05	489510.49
800	1	0.00125	1.00	35	1.00	44.6840339	44.6840339	178.736136	268.104204	16.3738879	10.9159252	9.4534686	0	640000
900	1	0.00111	1.00	36	1.00	46.2725745	46.2861871	185.117522	277.676284	16.6636216	11.109081	9.6207464	7.353E-05	810810.811
1000	1	0.001	1.00	37	1.00	47.717083	47.717083	190.868332	286.302498	16.9204757	11.2803171	9.7690412	0	1000000
5000	1	0.0002	1	38	1.00	72.5425799	72.5425799	290.170319	435.255479	20.8627774	13.9085182	12.04513	0	25000000
10000	1	0.0001	1	39	1.00	84.8303698	84.8303698	339.321479	508.982219	22.5606343	15.0404228	13.025388	0	100000000
20000	1	0.00005	1	39	1.00	98.0790657	98.0790657	392.316263	588.474394	24.2584912	16.1723275	14.005646	0	400000000

Plane Strain Theoretical Data pg2

magnitude X	magnitude Y	magnitude Z	K value	Test Values	X/Y	Y/Z		(X/Y)^2	(Y/Z)^2				I
1	1	1	#DIV/0!	1	1	1		1	1	3	9	0.33333333	2.5E-08
1.5	1	0.666	1.00	2	1.5	1.5015015		2.25	2.25450676	8.32714697	22.5981748	0.36848759	0.263657
2	1	0.5	1.00	3	2	2		4	4	21	49	0.42857143	0.7142857
2.5	1	0.4	1.00	4	2.5	2.5		6.25	6.25	46.3125	95.0625	0.48717949	1.1538462
3	1	0.333	1.00	5	3	3.003003		9	9.01802704	91.1802704	169.312457	0.53853256	1.5389942
3.5	1	0.285	1.00	6	3.5	3.50877193		12.25	12.3114805	164.127116	281.886427	0.58224554	1.8668416
4	1	0.2499	1.00	7	4	4.00160064		16	16.0128077	273.217731	441.336199	0.61906939	2.1430204
4.5	1	0.223	1.00	8	4.5	4.48430493		20.25	20.1089907	428.316053	658.624324	0.65031921	2.3773941
5	1	0.2	1.00	9	5	5		25	25	651	961	0.67741935	2.5806452
5.5	1	0.182	1.00	10	5.5	5.49450549		30.25	30.1895906	944.424707	1347.93878	0.70064362	2.7548272
6	1	0.166	1.00	11	6	6.02409639		36	36.2897373	1343.72028	1863.53448	0.72106006	2.9079505
6.5	1	0.154	1.00	12	6.5	6.49350649		42.25	42.1656266	1824.66335	2470.21909	0.73866458	3.0399844
7	1	0.143	1.00	13	7	6.99300699		49	48.9021468	2446.10734	3242.62551	0.75436011	3.1577009
7.5	1	0.133	1.00	14	7.5	7.51879699		56.25	56.5323082	3237.47465	4213.27882	0.76839791	3.2629844
8	1	0.125	1.00	15	8	8		64	64	4161	5329	0.78082192	3.3561644
8.5	1	0.118	1.00	16	8.5	8.47457627		72.25	71.818443	5261.70095	6643.63143	0.7919917	3.4399378
9	1	0.111	1.00	17	9	9.00900901		81	81.1622433	6656.30395	8297.40451	0.80221519	3.516614
9.5	1	0.105	1.00	18	9.5	9.52380952		90.25	90.7029478	8277.64399	10201	0.81145417	3.5859063
10	1	0.1	1.00	19	10	10		100	100	10101	12321	0.81981982	3.6486487
20	1	0.05	1.00	20	20	20		400	400	160401	177241	0.90498812	4.287411
30	1	0.0333	1.00	21	30	30.03003		900	901.802704	812525.236	868495.26	0.93555518	4.5166638
40	1	0.025	1.00	22	40	40		1600	1600	2561601	2692881	0.95124924	4.6343693
50	1	0.02	1.00	23	50	50		2500	2500	6252501	6507601	0.96079969	4.7059977
60	1	0.0167	1.00	24	60	59.8802395		3600	3585.64309	12911901.7	13349484.3	0.96722101	4.7541576
70	1	0.0143	1.00	25	70	69.9300699		4900	4890.21468	23966943.1	24661503.3	0.97183626	4.788772
80	1	0.0125	1.00	26	80	80		6400	6400	40966401	42003361	0.97531245	4.8148434
90	1	0.0111	1.00	27	90	90.0900901		8100	8116.22433	65749534.3	67226851.1	0.9780249	4.8351868
100	1	0.01	1.00	28	100	100		10000	10000	100010001	102030201	0.98019998	4.8514999
200	1	0.005	1.00	29	200	200		40000	40000	1600040001	1616120401	0.99005	4.925375
300	1	0.00333	1.00	30	300	300.3003		90000	90180.2704	8116314514	8170603457	0.99335558	4.9501669
400	1	0.0025	1.00	31	400	400		160000	160000	2.56E+10	2.5728E+10	0.9950125	4.9625938
500	1	0.002	1.00	32	500	500		250000	250000	6.25E+10	6.2751E+10	0.996008	4.97006
600	1	0.00167	1.00	33	600	598.802395		360000	358564.309	1.2908E+11	1.2951E+11	0.99667221	4.9750416
700	1	0.00143	1.00	34	700	699.300699		490000	489021.468	2.3962E+11	2.4031E+11	0.99714693	4.978602
800	1	0.00125	1.00	35	800	800		640000	640000	4.096E+11	4.1063E+11	0.99750312	4.9812735
900	1	0.00111	1.00	36	900	900.900901		810000	811622.433	6.5741E+11	6.5888E+11	0.99778025	4.9833519
1000	1	0.001	1.00	37	1000	1000		1000000	1000000	1E+12	1.002E+12	0.998002	4.985015
5000	1	0.0002	1	38	5000	5000		25000000	25000000	6.25E+14	6.2525E+14	0.99960008	4.9970006
10000	1	0.0001	1	39	10000	10000		100000000	100000000	1E+16	1.0002E+16	0.99980002	4.9985002
20000	1	0.00005	1	39	20000	20000		400000000	400000000	1.6E+17	1.6002E+17	0.99990001	4.9992501

Plane Strain Theoretical Data pg3

I	Es
2.5E-08	0
0.26365695	0.57412186
0.71428574	0.98025814
1.15384618	1.29583078
1.53899421	1.55437991
1.86684161	1.77344466
2.14302044	1.96079919
2.37739413	2.12461658
2.58064519	2.27608892
2.7548272	2.41017115
2.90795047	2.53676517
3.03998438	2.6464213
3.15770086	2.7512258
3.26298436	2.85127334
3.35616441	2.94077443
3.43993777	3.0243927
3.51661396	3.10805228
3.5859063	3.18557754
3.64864867	3.25634707
4.28741095	4.23660521
4.51666385	4.81072694
4.63436931	5.21686335
4.70599767	5.53243599
4.75415763	5.78886487
4.78877199	6.00757285
4.81484341	6.1971215
4.83518677	6.36439934
4.85149988	6.51269413
4.92537502	7.49295228
4.95016685	8.067074
4.96259377	8.47321042
4.97006002	8.78878306
4.97504161	9.04521191
4.97860204	9.26391991
4.98127346	9.45346856
4.9833519	9.6207464
4.98501502	9.7690412
4.99700062	12.0451301
4.99850018	13.0253883
4.99925006	14.0056464

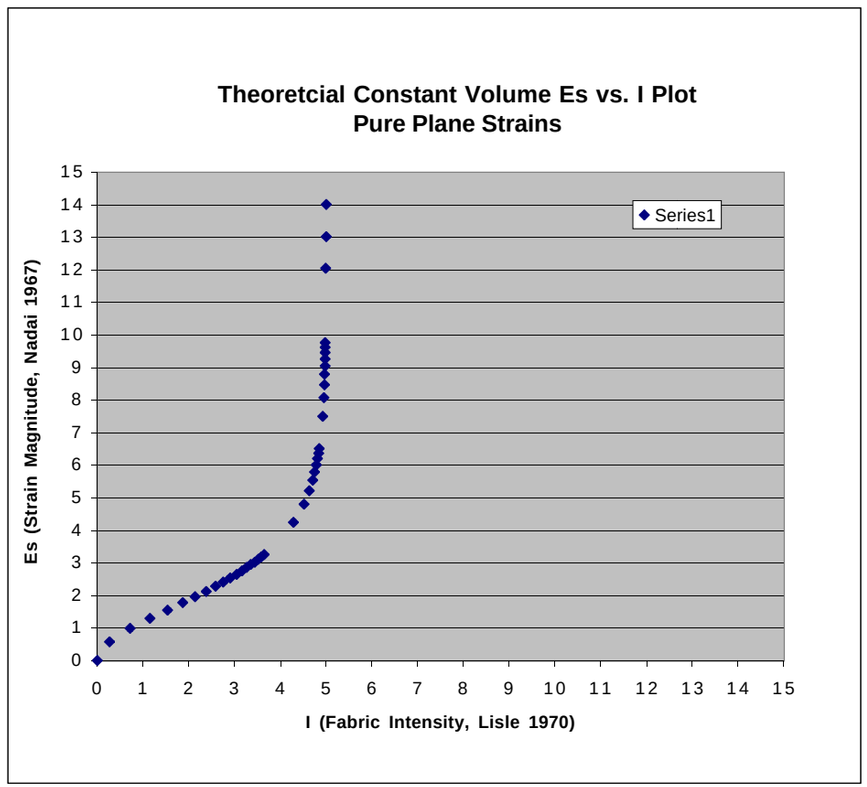

Plane Strain Theoretical Data pg4

S1/S3	Es
1	0
2.25225225	0.57412186
4	0.98025814
6.25	1.29583078
9.00900901	1.55437991
12.2807018	1.77344466
16.0064026	1.96079919
20.1793722	2.12461658
25	2.27608892
30.2197802	2.41017115
36.1445783	2.53676517
42.2077922	2.6464213
48.951049	2.7512258
56.3909774	2.85127334
64	2.94077443
72.0338983	3.0243927
81.0810811	3.10805228
90.4761905	3.18557754
100	3.25634707
400	4.23660521
900.900901	4.81072694
1600	5.21686335
2500	5.53243599
3592.81437	5.78886487
4895.1049	6.00757285
6400	6.1971215
8108.10811	6.36439934
10000	6.51269413
40000	7.49295228
90090.0901	8.067074
160000	8.47321042
250000	8.78878306
359281.437	9.04521191
489510.49	9.26391991
640000	9.45346856
810810.811	9.6207464
1000000	9.7690412
25000000	12.0451301
100000000	13.0253883
400000000	14.0056464

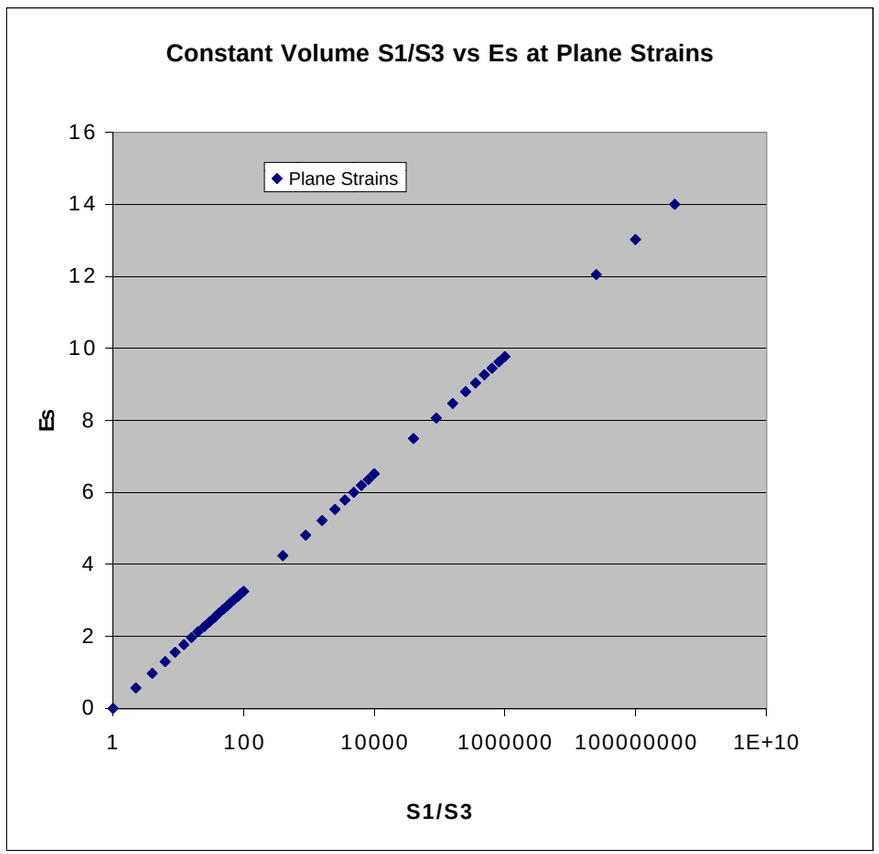

Flattening Strains Theoretical data pg1

magnitude X	magnitude Y	magnitude Z	K value	Test Values	No Volume Loss	(LN (X/Y))^2	(LN(Y/Z))^2	(LN(Z/X))^2	Sum	SQR Root	Octahedral Unit Shear	Natural Logarithmic Octahedral Strain	v	S1/S3
1	1	1	#DIV/0!	1	1.00	0	0	0	0	0	0	**0**	#DIV/0!	1
1.5	1.5	0.445	0.00	2	1.00	0	1.47658006	1.47658006	2.95316011	1.7184761	1.14565073	**0.9921626**	**1**	3.37078652
2	2	0.25	0.00	3	1.00	0	4.32407713	4.32407713	8.64815425	2.94077443	1.96051629	**1.6978569**	**1**	8
2.5	2.5	0.16	0.00	4	1.00	0	7.55629835	7.55629835	15.1125967	3.88749234	2.59166156	**2.2444447**	**1**	15.625
3	3	0.111	0.00	5	1.00	0	10.8691366	10.8691366	21.7382732	4.66243212	3.10828808	**2.6918564**	**1**	27.027027
3.5	3.5	0.082	0.00	6	1.00	0	14.0910069	14.0910069	28.1820139	5.30867346	3.53911564	**3.064964**	**1**	42.6829268
4	4	0.0622	0.00	7	1.00	0	17.3363531	17.3363531	34.6727061	5.88835343	3.92556895	**3.3996424**	**1**	64.3086817
4.5	4.5	0.0495	0.00	8	1.00	0	20.3388373	20.3388373	40.6776746	6.37790519	4.25193679	**3.6822853**	**1**	90.9090909
5	5	0.04	0.00	9	1.00	0	23.3126135	23.3126135	46.6252271	6.82826677	4.55217785	**3.9423017**	**1**	125
5.5	5.5	0.033	0.00	10	1.00	0	26.1734131	26.1734131	52.3468263	7.23511066	4.82340711	**4.1771931**	**1**	166.666667
6	6	0.0279	0.00	11	1.00	0	28.8464385	28.8464385	57.6928771	7.59558274	5.06372182	**4.3853117**	**1**	215.053763
6.5	6.5	0.0236	0.00	12	1.00	0	31.5654156	31.5654156	63.1308312	7.94549125	5.29699417	**4.5873315**	**1**	275.423729
7	7	0.0205	0.00	13	1.00	0	34.0266952	34.0266952	68.0533904	8.24944789	5.49963192	**4.762821**	**1**	341.463415
7.5	7.5	0.0177	0.00	14	1.00	0	36.5915341	36.5915341	73.1830682	8.55471029	5.7031402	**4.9390643**	**1**	423.728814
8	8	0.0156	0.00	15	1.00	0	38.9366753	38.9366753	77.8733506	8.82458785	5.88305856	**5.0948782**	**1**	512.820513
8.5	8.5	0.0138	0.00	16	1.00	0	41.2568925	41.2568925	82.5137851	9.08370987	6.05580658	**5.2444823**	**1**	615.942029
9	9	0.0124	0.00	17	1.00	0	43.3923024	43.3923024	86.7846048	9.3158255	6.21055033	**5.3784944**	**1**	725.806452
9.5	9.5	0.0111	0.00	18	1.00	0	45.590881	45.590881	91.181762	9.54891418	6.36594279	**5.5130682**	**1**	855.855856
10	10	0.01	0.00	19	1.00	0	47.717083	47.717083	95.434166	9.7690412	6.51269413	**5.6401586**	**1**	1000
20	20	0.0025	0.00	20	1.00	0	80.7697067	80.7697067	161.539413	12.7098156	8.47321042	**7.3380155**	**1**	8000
30	30	0.00111	0.00	21	1.00	0	104.133711	104.133711	208.267422	14.4314733	9.62098221	**8.332015**	**1**	27027.027
40	40	0.000622	0.00	22	1.00	0	122.577003	122.577003	245.154007	15.6573946	10.4382631	**9.039801**	**1**	64308.6817
50	50	0.0004	0.00	23	1.00	0	137.735316	137.735316	275.470632	16.597308	11.064872	**9.5824602**	**1**	125000
60	60	0.000279	0.00	24	1.00	0	150.765082	150.765082	301.530164	17.3646239	11.576416	**10.02547**	**1**	215053.763
70	70	0.000205	0.00	25	1.00	0	162.332975	162.332975	324.665949	18.0184891	12.0123261	**10.40298**	**1**	341463.415
80	80	0.000156	0.00	26	1.00	0	172.861521	172.861521	345.723041	18.593629	12.3957527	**10.735037**	**1**	512820.513
90	90	0.000124	0.00	27	1.00	0	182.116069	182.116069	364.232137	19.0848667	12.7232445	**11.018653**	**1**	725806.452
100	100	0.0001	0.00	28	1.00	0	190.868332	190.868332	381.736664	19.5380824	13.0253883	**11.280317**	**1**	1000000
200	200	0.000025	0.00	29	1.00	0	252.649502	252.649502	505.299004	22.4788568	14.9859046	**12.978174**	**1**	8000000
300	300	0.0000111	0.00	30	1.00	0	292.832451	292.832451	585.664903	24.2005145	16.1336763	**13.972174**	**1**	27027027
400	400	0.00000622	0.00	31	1.00	0	323.25182	323.25182	646.503639	25.4264358	16.9509572	**14.67996**	**1**	64308681.7
500	500	0.000004	0.00	32	1.00	0	347.592184	347.592184	695.184369	26.3663492	17.5775661	**15.222619**	**1**	125000000
600	600	0.00000279	0.00	33	1.00	0	368.117892	368.117892	736.235784	27.1336651	18.0891101	**15.665629**	**1**	215053763
700	700	0.00000205	0.00	34	1.00	0	386.07342	386.07342	772.14684	27.7875303	18.5250202	**16.043138**	**1**	341463415
800	800	0.00000156	0.00	35	1.00	0	402.220532	402.220532	804.441064	28.3626702	18.9084468	**16.375195**	**1**	512820513
900	900	0.00000124	0.00	36	1.00	0	416.274001	416.274001	832.548001	28.8539079	19.2359386	**16.658811**	**1**	725806452
1000	1000	0.000001	0.00	37	1.00	0	429.453747	429.453747	858.907494	29.3071236	19.5380824	**16.920476**	**1**	1000000000
5000	5000	0.00000004	0.00	38	1.00	0	652.883219	652.883219	1305.76644	36.1353904	24.0902602	**20.862777**	**1**	1.25E+11
10000	10000	0.00000001	0.00	39	1.00	0	763.473328	763.473328	1526.94666	39.0761648	26.0507765	**22.560634**	**1**	1E+12
20000	20000	2.5E-09	0.00	39	1.00	0	882.711591	882.711591	1765.42318	42.0169392	28.0112928	**24.258491**	**1**	8E+12
200000	200000	2.5E-11	0.00	40	1.00	0	1340.89388	1340.89388	2681.78777	51.7859804	34.523987	**29.89865**	**1**	8E+15
2000000	2000000	2.5E-13	0.00	41	1.00	0	1894.51034	1894.51034	3789.02069	61.5550216	41.0366811	**35.538808**	**1**	8E+18
20000000000	20000000000	2.50E-21	0.00	41	1.00	0	5063.31784	5063.31784	10126.6357	100.631186	67.0874576	**58.099443**	**1**	8E+30

Flattening Strains Theoretical data pg2

magnitude X	magnitude Y	magnitude Z	K value	Test Values	X/Y	Y/Z	(X/Y)^2	(Y/Z)^2				I
1	1	1	#DIV/0!	1	1	1	1	1	3	9	0.33333333	**2.5E-08**
1.5	1.5	0.445	0.00	2	1	3.37078652	1	11.3622017	23.7244035	59.931953	0.39585567	**0.4689176**
2	2	0.25	0.00	3	1	8	1	64	129	289	0.44636678	**0.8477509**
2.5	2.5	0.16	0.00	4	1	15.625	1	244.140625	489.28125	1040.0625	0.47043447	**1.0282585**
3	3	0.111	0.00	5	1	27.027027	1	730.46019	1461.92038	3030.94887	0.48233093	**1.117482**
3.5	3.5	0.082	0.00	6	1	42.6829268	1	1821.83224	3644.66449	7459.06068	0.48862245	**1.1646684**
4	4	0.0622	0.00	7	1	64.3086817	1	4135.60654	8272.21308	16800.6609	0.49237427	**1.192807**
4.5	4.5	0.0495	0.00	8	1	90.9090909	1	8264.46281	16529.9256	33422.4876	0.49457496	**1.2093123**
5	5	0.04	0.00	9	1	125	1	15625	31251	63001	0.49603975	**1.2202981**
5.5	5.5	0.033	0.00	10	1	166.666667	1	27777.7778	55556.5556	111778.778	0.49702239	**1.227668**
6	6	0.0279	0.00	11	1	215.053763	1	46248.1212	92497.2423	185853.7	0.49768846	**1.2326635**
6.5	6.5	0.0236	0.00	12	1	275.423729	1	75858.2304	151717.461	304535.616	0.49819283	**1.2364463**
7	7	0.0205	0.00	13	1	341.463415	1	116597.264	233195.527	467755.908	0.49854106	**1.239058**
7.5	7.5	0.0177	0.00	14	1	423.728814	1	179546.107	359093.215	719880.345	0.49882347	**1.2411761**
8	8	0.0156	0.00	15	1	512.820513	1	262984.878	525970.757	1053991.8	0.49902737	**1.2427053**
8.5	8.5	0.0138	0.00	16	1	615.942029	1	379384.583	758770.166	1520003.1	0.49918988	**1.2439241**
9	9	0.0124	0.00	17	1	725.806452	1	526795.005	1053591.01	2110084.25	0.4993123	**1.2448422**
9.5	9.5	0.0111	0.00	18	1	855.855856	1	732489.246	1464979.49	2933381.41	0.49941664	**1.2456248**
10	10	0.01	0.00	19	1	1000	1	1000000	2000001	4004001	0.49950062	**1.2462547**
20	20	0.0025	0.00	20	1	8000	1	64000000	128000001	256032001	0.49993751	**1.2495313**
30	30	0.00111	0.00	21	1	27027.027	1	730460190	1460920381	2921948869	0.4999815	**1.2498613**
40	40	0.000622	0.00	22	1	64308.6817	1	4135606538	8271213078	1.6543E+10	0.49999223	**1.2499417**
50	50	0.0004	0.00	23	1	125000	1	1.5625E+10	3.125E+10	6.2501E+10	0.499996	**1.24997**
60	60	0.000279	0.00	24	1	215053.763	1	4.6248E+10	9.2496E+10	1.8499E+11	0.49999768	**1.2499826**
70	70	0.000205	0.00	25	1	341463.415	1	1.166E+11	2.3319E+11	4.6639E+11	0.49999854	**1.249989**
80	80	0.000156	0.00	26	1	512820.513	1	2.6298E+11	5.2597E+11	1.0519E+12	0.49999903	**1.2499927**
90	90	0.000124	0.00	27	1	725806.452	1	5.268E+11	1.0536E+12	2.1072E+12	0.49999931	**1.2499949**
100	100	0.0001	0.00	28	1	1000000	1	1E+12	2E+12	4E+12	0.4999995	**1.2499963**
200	200	0.000025	0.00	29	1	8000000	1	6.4E+13	1.28E+14	2.56E+14	0.49999994	**1.2499996**
300	300	0.0000111	0.00	30	1	27027027	1	7.3046E+14	1.4609E+15	2.9218E+15	0.49999998	**1.2499999**
400	400	0.00000622	0.00	31	1	64308681.7	1	4.1356E+15	8.2712E+15	1.6542E+16	0.49999999	**1.25**
500	500	0.000004	0.00	32	1	125000000	1	1.5625E+16	3.125E+16	6.25E+16	0.5	**1.25**
600	600	0.00000279	0.00	33	1	215053763	1	4.6248E+16	9.2496E+16	1.8499E+17	0.5	**1.25**
700	700	0.00000205	0.00	34	1	341463415	1	1.166E+17	2.3319E+17	4.6639E+17	0.5	**1.25**
800	800	0.00000156	0.00	35	1	512820513	1	2.6298E+17	5.2597E+17	1.0519E+18	0.5	**1.25**
900	900	0.00000124	0.00	36	1	725806452	1	5.268E+17	1.0536E+18	2.1072E+18	0.5	**1.25**
1000	1000	0.000001	0.00	37	1	1000000000	1	1E+18	2E+18	4E+18	0.5	**1.25**
5000	5000	0.00000004	0.00	38	1	1.25E+11	1	1.5625E+22	3.125E+22	6.25E+22	0.5	**1.25**
10000	10000	0.00000001	0.00	39	1	1E+12	1	1E+24	2E+24	4E+24	0.5	**1.25**
20000	20000	2.5E-09	0.00	39	1	8E+12	1	6.4E+25	1.28E+26	2.56E+26	0.5	**1.25**
200000	200000	2.5E-11	0.00	40	1	8E+15	1	6.4E+31	1.28E+32	2.56E+32	0.5	**1.25**
2000000	2000000	2.5E-13	0.00	41	1	8E+18	1	6.4E+37	1.28E+38	2.56E+38	0.5	**1.25**
20000000000	20000000000	2.50E-21	0.00	41	1	8E+30	1	6.4E+61	1.28E+62	2.56E+62	0.5	**1.25**

Flattening Strains Theoretical data pg3

I	Es
2.5E-08	0
0.46891756	0.99216264
0.84775089	1.69785691
1.02825854	2.24444475
1.11748198	2.69185644
1.16466838	3.06496405
1.19280702	3.39964244
1.20931226	3.68228528
1.22029812	3.94230166
1.22766797	4.17719309
1.2326635	4.38531174
1.23644625	4.58733151
1.23905799	4.76282096
1.24117608	4.93906429
1.24270532	5.09487817
1.24392413	5.24448234
1.24484225	5.37849436
1.24562484	5.51306817
1.24625471	5.64015857
1.24953135	7.33801548
1.24986128	8.332015
1.24994171	9.03980101
1.24997003	9.58246023
1.24998259	10.0254703
1.24998904	10.4029795
1.24999271	10.7350367
1.24999486	11.0186529
1.24999628	11.2803171
1.24999956	12.978174
1.24999989	13.9721736
1.24999997	14.6799596
1.25	15.2226188
1.25000001	15.6656289
1.25000001	16.0431381
1.25000002	16.3751953
1.25000002	16.6588115
1.25000002	16.9204757
1.25000002	20.8627774
1.25000002	22.5606343
1.25000002	24.2584912

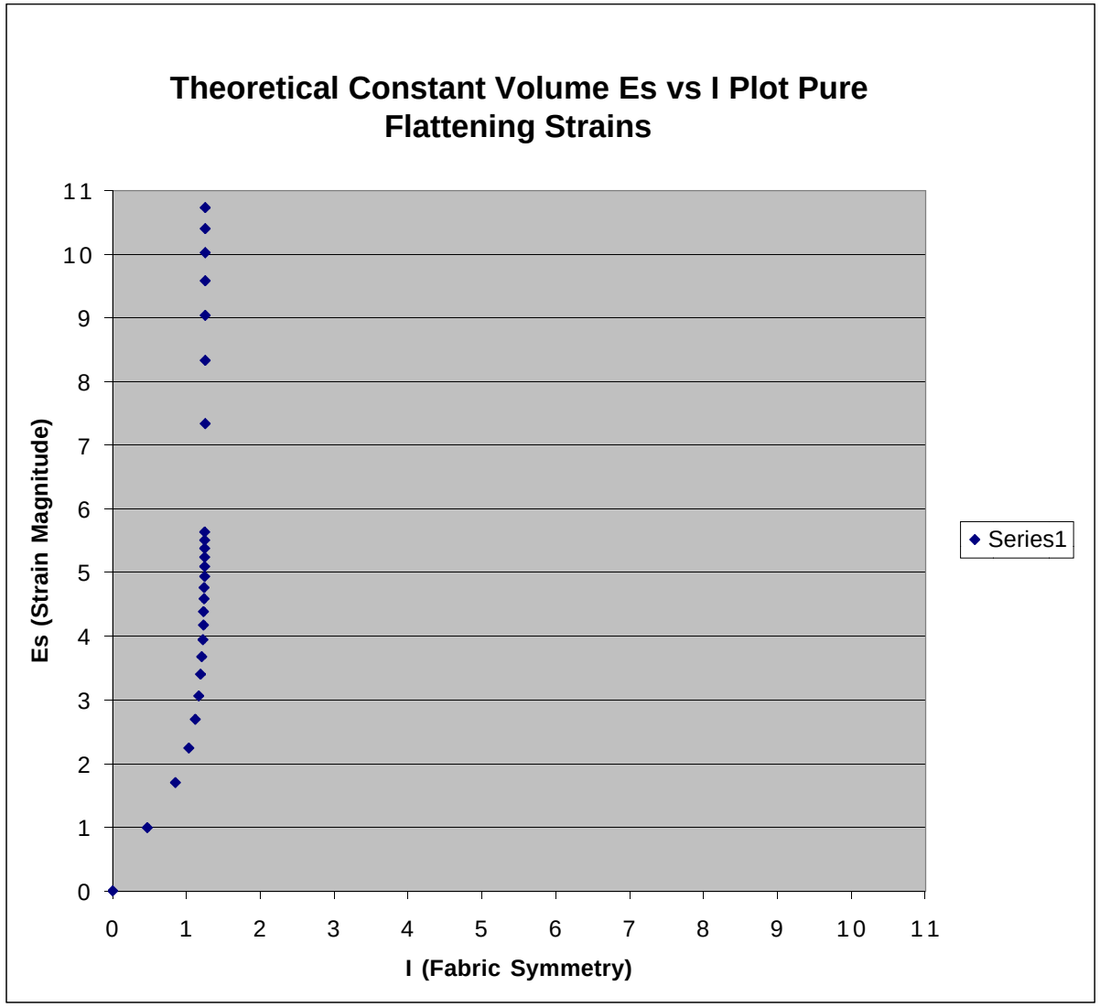

Flattening Strains Theoretical data pg4

S1/S3	Es
1	0
3.37078652	0.99216264
8	1.69785691
15.625	2.24444475
27.027027	2.69185644
42.6829268	3.06496405
64.3086817	3.39964244
90.9090909	3.68228528
125	3.94230166
166.666667	4.17719309
215.053763	4.38531174
275.423729	4.58733151
341.463415	4.76282096
423.728814	4.93906429
512.820513	5.09487817
615.942029	5.24448234
725.806452	5.37849436
855.855856	5.51306817
1000	5.64015857
8000	7.33801548
27027.027	8.332015
64308.6817	9.03980101
125000	9.58246023
215053.763	10.0254703
341463.415	10.4029795
512820.513	10.7350367
725806.452	11.0186529
1000000	11.2803171
8000000	12.978174
27027027	13.9721736
64308681.7	14.6799596
125000000	15.2226188
215053763	15.6656289
341463415	16.0431381
512820513	16.3751953
725806452	16.6588115
1000000000	16.9204757
1.25E+11	20.8627774
1E+12	22.5606343
8E+12	24.2584912

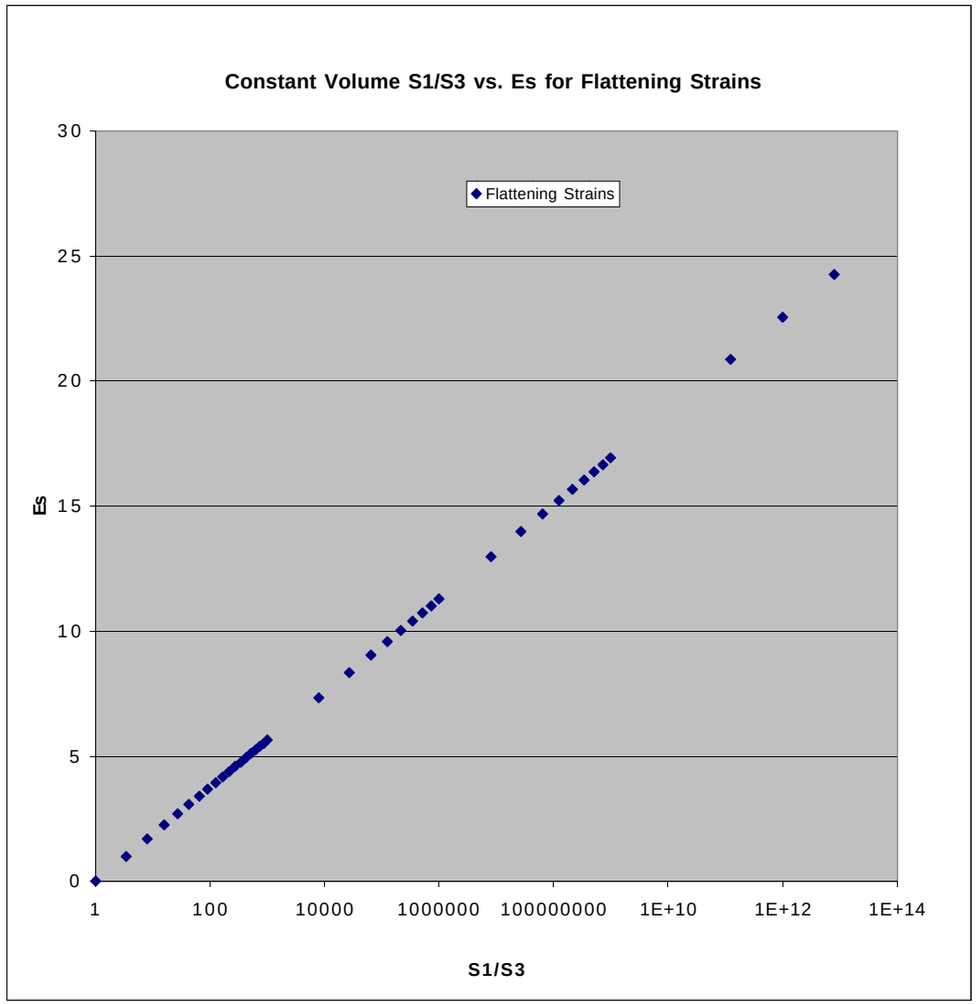

Vita

Following the completion of her Master's degree at Virginia Tech, Kelly Kathleen Rose will relocate to Cody, Wyoming where she has a job as a geologist with Marathon Oil Company. She received her Bachelor's of Science degree from Denison University in May of 1996.